

Model-based optimization and experimental investigation of CO₂ methanation

Dissertation

zur Erlangung des akademischen Grades

Doktoringenieur

(Dr.-Ing.)

von M.Sc. Ali El Sibai

geb. am 26.02.1987 in Beirut

genehmigt durch die Fakultät für Verfahrens-und Systemtechnik

der Otto-von-Guericke-Universität Magdeburg

Promotionskommission: Prof. Dr.-Ing. Kai Sundmacher

Prof. Dr.-Ing. Christof Hamel

Dr. Liisa Rihko-Struckmann

eingereicht am: 25.4.2019

Promotionskolloquium am: 29.8.2019

ZUSAMMENFASSUNG

Erneuerbare Energiesysteme werden heute sowohl von der Wissenschaft, als auch von der Öffentlichkeit, als unverzichtbare Technologien wahrgenommen, um den zukünftigen Energiebedarf zu decken, die Versorgungssicherheit zu gewährleisten, und die globale Erwärmung zu bekämpfen. Der fluktuierende Charakter erneuerbarer Energiequellen macht Energiespeicher zu einer zentralen Komponente in einem erneuerbaren Energiesystem. In dieser Hinsicht bietet das Power-to-Gas Konzept (P2G) einen effizienten Weg um überschüssige erneuerbare Energie in großem Maßstab über Zeiträume von Stunden bis hin zu Monaten zu speichern. Die Infrastruktur für den Transport und die Speicherung von Erdgas ist in vielen Ländern bereits etabliert. Daher erscheint die Umwandlung erneuerbarer Energie in H_2 und die nachgeschaltete Produktion von synthetischem Erdgas (SNG, synthetic natural gas) mit Hilfe der Methanisierung von CO_2 eine attraktive Prozessroute. Das Recycling von CO_2 ist ein weiterer zentraler Vorteil dieses Prozesses. Diese Arbeit untersucht die CO_2 Methanisierung im Kontext der P2G Anwendung auf unterschiedlichen hierarchischen Stufen: die chemischen Kinetiken, den Reaktor, und den gesamten Prozess.

Im ersten Teil dieser Arbeit wird ein modellbasiertes optimales Reaktordesign für die Produktionen von hochwertigem SNG entwickelt. Dieses ist nach einem nachgeschalteten Trocknungsprozess bereit in das Erdgasnetz eingespeist zu werden. Dazu wird das dreistufige Verfahren zum Reaktordesign von Peschel (2010), welches auf der flussorientierten Methode der elementaren Prozessfunktionen (EPF) basiert, implementiert. Auf der ersten Stufe werden noch keine vordefinierten Apparate berücksichtigt. Stattdessen wird der Reaktor durch ein Massenelement im thermodynamischen Zustandsraum repräsentiert.

Das Massenelement wird über die Reaktionszeit durch unbegrenzte Massen- und Wärmeströme so manipuliert, dass optimale Profile der Zustandsvariable (z.B. T , x_i) erreicht werden. Die Effekte optimaler Dosierung und Entfernung verschiedener Komponenten, sowie die optimale Kühlungsstrategie auf die Produktivität des Reaktors wird systematisch untersucht. Basierend auf den Resultaten der Stufe 1 wird gezeigt dass die kontinuierliche Entfernung von Wasser kombiniert mit einer aktiven Kühlung der vielversprechendste Ansatz zur Verbesserung der Reaktorperformance ist. Daher werden auf Stufe 2 zwei Reaktorkonfigurationen betrachtet und auf Basis ihrer Raum-Zeit-Ausbeute verglichen: (1) eine Kaskade polytroper Rohrbündelreaktoren mit

zwischen geschalteten Kondensationsschritten, und (2) ein polytroper hydrophiler Membranreaktor. Für jedes Szenario werden optimal geometrische Designs und Betriebsbedingungen, wie Zufluss, Temperaturprofile und Reaktordimensionen, bestimmt. Es wird gezeigt, dass eine Kaskade aus drei Kondensationsschritten und vier extern gekühlten Rohrbündelreaktoren die beste Konfiguration darstellen um die Raum-Zeit-Ausbeute zu maximieren. Auf Stufe 3 werden schließlich die optimalen Temperaturprofile technisch realisiert. Die vorgeschlagene Konfiguration wird mit einer klassischen Kaskade adiabater Reaktoren mit Zwischenkühlung oder einem einzelnen polytropen Reaktor verglichen. Die Ergebnisse zeigen dass die vorgeschlagene Konfiguration eine signifikant bessere Produktivität aufweist. Darüber hinaus ist es möglich eine gute Temperaturregelung im Reaktor zu haben, die die Bildung von Hotspots verhindert. Dies führt auch zu einer Verlängerung der Lebensdauer des Katalysators.

Der zweite Teil dieser Arbeit behandelt das optimale Design und den Betrieb des gesamten Methanisierungsprozesses mit Hauptaugenmerk auf das Reaktordesign. Der betrachtete Prozess besteht aus einem Reaktionsbereich und einem Trocknungsbereich. Der Reaktionsbereich ist eine Kaskade von Reaktoren und Kühlern, während der Trocknungsbereich durch eine Glykol Dehydrierungsanlage dargestellt wird. Während die Reaktoren rigoros modelliert werden, werden die anderen Prozesseinheiten (Verdichter, Pumpen, Wärmetauscher und Absorber) durch Short-Cut Modelle beschrieben. Da die Reaktoren und die verschiedenen Prozesseinheiten simultan nach den Betriebs- und Investitionskosten optimiert werden schließt das Optimierungsproblem Kostenmodelle mit ein. Es wird gezeigt, dass der kostenoptimale Reaktionsbereich aus drei Rohrbündelreaktoren mit zwei Kondensationsschritten für die Wasserabführung besteht. Die Ergebnisse zeigen auch die Wichtigkeit der Berücksichtigung der Interaktionen zwischen den Reaktoren und den anderen Prozesseinheiten beim Bestimmen des optimalen Prozessdesigns und den Betriebsbedingungen.

Im letzten Teil dieser Arbeit wird ein umfassendes mechanistisches kinetisches Modell der CO₂ Methanisierung über einem kommerziellen Nickel-basierten Katalysator entwickelt. Es wird angenommen dass die CO₂ Methanisierung durch die Reaktionsreihe aus inverser Wassergas Shift Reaktion (R-WGS) und er Methanisierung von CO realisiert wird. Damit besteht das hergeleitete Modell aus Reaktionsraten dieser beiden Reaktionen. Es wurden Daten über einen großen industriell relevanten Bereich

an Zuständen (Temperatur, Druck, Zufluss Zusammensetzung) gesammelt und zur Diskriminierung zwischen rivalisierenden Modellen und zur Parameterschätzung verwendet. Zur Parameterschätzung wird die Determinante der Matrix der Quadratsummen und den Kreuzprodukten der Residuen minimiert. Darüber hinaus wurde die Methode von Vajda, die auf einer Eigenwertzerlegung der Fisher-Informationmatrix basiert, verwendet um die quantitative Identifizierbarkeit der Parameter der besten Modelle zu untersuchen. Von zwölf Modellparametern sind acht eindeutig identifizierbar. Auch die Vorhersagequalität des Modells wurde unter Verwendung eines Datensatzes, der nicht zur Parameterschätzung herangezogen wurde, validiert.

ABSTRACT

Today, renewable energy systems are perceived by the scientific communities and the public opinion as crucial tools for meeting future energy demands, ensuring the security energy supplies, and combating global warming. The intermittent nature of renewable sources, nevertheless, makes energy storage a key component in any renewable energy system. In this regard, power-to-gas concept (P2G) offers an efficient means to store excess renewable energy in large scale and for periods ranging from hours to months. Given that the infrastructure for transporting and storing natural gas is already established in many countries, converting renewable electricity into H_2 and then into Synthetic Natural Gas (SNG) via CO_2 methanation appears to be an attractive P2G process route. The recycling of CO_2 is another main advantage of this route. This thesis investigates the CO_2 methanation in the context of P2G application on various hierarchical levels: chemical kinetics, reactor, and overall process.

In the first part of this work, a model-based optimal reactor design is developed for the production of high quality SNG that can be ready for grid injection following a downstream drying step. The three-level reactor design procedure of Peschel¹, which is based originally on the flux-oriented Elementary Process Function (EPF) methodology², is implemented. On level 1, predefined apparatuses are not considered. Instead, the reactor is represented by a matter element in the thermodynamic state space. The matter element is manipulated over the entire reaction time by unlimited mass and heat fluxes so that optimal profiles of the state variables (e.g. T , x_i) are achieved. The effect of optimal dosing/removal of certain components and optimal cooling strategies on the reactor productivity is systematically investigated. Based on the results of Level 1, it is found that continuous water removal combined with active cooling is the most promising approach for enhancing the reactor performance. Consequently, on Level 2, two reactor configurations are considered and compared on the basis of their space-time yield: (1) a cascade of polytropic multi-tubular packed bed reactor with intermediate

condensation steps and (2) a polytropic hydrophilic membrane reactor. For each case scenario, optimal geometric designs and operating conditions are determined such as the inlet conditions, temperature profiles, reactor dimensions. It is concluded that a cascade of three condensation steps and four externally cooled multitubular reactor is the best configuration for maximizing space-time yield. On level 3, the optimal temperature profiles are technically realized. Furthermore, the proposed configuration is compared with the traditionally adopted cascade of adiabatic reactors with intercooling steps or a single polytropic reactor. The results show that our proposed reactor configuration performs significantly better in terms of productivity. Moreover, using our configuration, it is possible to have good temperature control inside the reactors and prevent the formation of hotspots, thus lengthening the life time of the catalyst.

The second part of this work deals with the optimal design and operation of the whole methanation process with main emphasis on the reactor design. The considered process design comprise of a reaction section and a drying section. The reaction section is a cascade of reactors and condensers, while the drying section is represented by a glycol dehydration unit. While the reactors are rigorously modeled, all other process units (compressors, pumps, heat exchangers, and absorber) are described using short-cut models. Since the reactors and the various process units are simultaneously optimized for reduced operating and investment costs, the optimization problem includes cost models as well. It is shown that the cost optimal reaction section is a cascade of three multitubular reactors with two intermediate condensation steps for water removal. Furthermore, the results clearly demonstrate the significant importance of accounting for the interaction between the reaction section and the other process units when determining the optimal reactor design and process operating conditions.

In the last part of this work, a comprehensive mechanistic kinetic model that best described CO₂ methanation reaction over a commercial nickel-based catalyst is developed. It is proposed that CO₂ methanation occurs through a series of reactions, namely the r-WGS and the CO methanation. As such, the derived model is comprised of

the rate expressions of these two reactions. Data collected over a wide range of industrial relevant conditions (temperature, pressure, and feed content) is used in discriminating between rival models and in estimating the parameters. The parameters are estimated by minimizing the determinant of the matrix of the sum of squares and the cross-products of the residuals. Furthermore, the method of Vajda^{3,4}, which is based on eigen-decomposition of the Fisher Information Matrix, is used to investigate the quantitative identifiability of the parameters of the most adequate model. Based on this investigation, it is shown that out of the twelve model parameters, eight are uniquely identifiable. Also, the predictive ability of the model is validated using a different set of data that was not used in the estimation.

TABLE OF CONTENTS

1 INTRODUCTION.....	1
1.1 MOTIVATION AND SCOPE.....	1
1.2 STRUCTURE OF THE THESIS	2
2 THEORETICAL BACKGROUND.....	5
2.1 SABATIER REACTION	5
2.1.1 <i>Heterogeneous catalysts</i>	6
2.1.2 <i>Reaction mechanisms</i>	7
2.1.3 <i>Reactors</i>	11
3 MODEL-BASED OPTIMAL DESIGN AND OPERATION OF THE SABATIER REACTOR.....	14
3.1 LEVEL 1.....	15
3.1.1 <i>Model formulation</i>	17
3.1.2 <i>Results and discussion</i>	20
3.2 LEVEL 2.....	23
3.2.1 <i>Reactor cascade with interstage condensation</i>	24
3.2.2 <i>Membrane reactor</i>	35
3.2.3 <i>Comparison between reactor cascade and membrane reactor</i>	39
3.3 LEVEL 3.....	40
3.3.1 <i>Model formulation for 3CS reactor cascade</i>	40
3.3.2 <i>Results and discussion</i>	41
3.4 CONCLUSION	44
4 TOTAL COST OPTIMIZATION OF THE SABATIER PROCESS.....	46
4.1 MODELING AND SIZING OF EQUIPMENT.....	46
4.1.1 <i>Reactors</i>	46
4.1.2 <i>Heat exchangers</i>	47

4.1.3 Compressors.....	48
4.1.4 Condensers.....	49
4.1.5 Glycol dehydration unit	50
4.2 COSTING.....	55
4.2.1 Capital cost	55
4.2.2 Raw materials and utility cost.....	56
4.3 RESULTS AND DISCUSSION.....	57
4.4 CONCLUSION	62
5 ON THE KINETICS OF THE SABATIER REACTION.....	64
5.1 INTRODUCTION.....	64
5.2 EXPERIMENTAL	66
5.2.1 Experimental setup.....	66
5.2.2 Preliminary and kinetic measurements.....	67
5.3 THEORETICAL.....	68
5.3.1 Consecutive route versus Direct route.....	69
5.3.2 Mechanistic derivation of plausible kinetic models.....	70
5.3.3 Parameter estimation and Model discrimination	78
5.3.4 Quantitative identifiability of the parameters.....	80
5.4 RESULTS AND DISCUSSION.....	84
5.4.1 Preliminary results.....	84
5.4.2 Influence of Temperature.....	86
5.4.3 Influence of H ₂ and CO ₂	87
5.4.4 Influence of H ₂ O.....	88
5.4.5 Regression analysis: Comparison of results obtained for different kinetic models	89
5.5 COMPARISON BETWEEN REACTION RATES REPORTED IN LITERATURE.....	96
5.6 CONCLUSION	98
6 SUMMARY AND OUTLOOK.....	99

7 APPENDIX..... 103
8 LITERATURE CITED..... 107

LIST OF FIGURES

FIGURE 3.1 THE GENERAL SCHEME OF THE PROPOSED SABATIER PROCESS WITH THE REACTION STEP DEPICTED, ACCORDING TO THE EPF APPROACH, BY THE FLUID ELEMENT.....	15
FIGURE 3.2 THE DECISION STRUCTURE OF THE SABATIER REACTOR DESIGN BASED ON THE EPF METHODOLOGY	20
FIGURE 3.3 RESULTS OF LEVEL 1; OPTIMAL TEMPERATURE PROFILES OF CASE 1 AND CASE 5 (LEFT). OPTIMAL PROFILE OF H ₂ O EXTRACTION AND MOLE FRACTION OF CASE 4 (RIGHT)	21
FIGURE 3.4 STY CALCULATED FOR THE DIFFERENT CASCADES.....	31
FIGURE 3.5 RESULTS OF 3CS CASCADE OF LEVEL 2, COMPONENT MOLE FRACTION PROFILE IN THE FOUR REACTORS.	33
FIGURE 3.6 RESULTS OF 3CS CASCADE OF LEVEL 2, COOLANT AND REACTION MIXTURE TEMPERATURE PROFILE IN THE FOUR REACTORS	34
FIGURE 3.7 RESULTS OF MEMBRANE REACTOR. FROM TOP TO BOTTOM: PERMEANCE AND WATER FLUX OPTIMAL PROFILE, COMPONENT MOLE FRACTION PROFILE, OPTIMAL TEMPERATURE PROFILE OF THE COOLANT AND THE REACTION MIXTURE.....	39
FIGURE 3.8 SCHEMATIC REPRESENTATION OF THE 3CS CASCADE INTEGRATED WITH THE DEHYDRATION PROCESS	40
FIGURE 3.9 RESULTS OF 3CS CASCADE OF LEVEL 3, COOLANT AND REACTION MIXTURE TEMPERATURE PROFILE IN THE FOUR REACTORS	41
FIGURE 3.10 SPACE TIME YIELD OBTAINED BY OUR OPTIMAL REACTOR CONFIGURATION (3CS) AND OTHER REACTOR DESIGNS (ADIABATIC CASCADE AND SINGLE POLYTROPIC REACTOR).....	43
FIGURE 3.11 TEMPERATURE PROFILE OF A SINGLE POLYTROPIC REACTOR	44
FIGURE 4.1 GLYCOL UNI- AN OVERVIEW OF THE MAIN COMPONENTS.....	50
FIGURE 4.2 RELATIVE PRODUCTION COST FOR THE THREE CASCADES	58

FIGURE 4.3 PROCESS LAYOUT OF THE COST OPTIMAL PROCESS	58
FIGURE 4.4: OPTIMAL TEMPERATURE PROFILES (LEFT COLUMN), PARTIAL PRESSURES (RIGHT COLUMN) IN THE TUBES OF THE THREE REACTORS (FROM TOP TO BOTTOM: REACTORS 1, 2, AND 3).	59
FIGURE 5.1 A SCHEMATIC REPRESENTATION OF THE EXPERIMENTAL SETUP USED IN THE KINETIC STUDY.....	66
FIGURE 5.2 STABILITY TEST: CONVERSION AND SELECTIVITY VERSUS TIME.....	84
FIGURE 5.3 INFLUENCE OF TOTAL PRESSURE ON CO ₂ CONNVERSION AND SELECTIVITY TOWARDS CH ₄	85
FIGURE 5.4 INFLUENCE OF SPACE VELOCITY ON CO ₂ CONVERSION AND SELECTIVITY TOWARDS CH ₄ AT DIFFERENT TEMPERATURE.....	86
FIGURE 5.5 INFLUENCE OF TEMPERATURE AND INLET COMPOSITION ON THE RATE FORMATION OF CH ₄ AND CO	87
FIGURE 5.6 INFLUENCE OF H ₂ AND CO ₂ PARTIAL PRESSURE ON THE RATE OF DISAPPEARANCE OF CO ₂ AND THE RATE OF FORMATION OF CO AND CH ₄	88
FIGURE 5.7 INFLUENCE OF PARTIAL PRESSURE OF H ₂ O ON THE FORMATION RATE OF CH ₄ AND CO	89
FIGURE 5.8 PARITY PLOT OF DIFFERENT MODELS. FROM TOP TO BOTTOM: MODEL A, RONSCH MODEL, XU MODEL, AND MODEL B. LEFT COLUMN: RATE OF R-WGS. RIGHT COLUMN: RATE OF CO METHANATION.....	92
FIGURE 5.9 PARITY PLOT: PREDICTIVE ABILITY OF THE DERIVED MODEL.....	96
FIGURE 5.10 PERFORMANCE OF A PACKED BED REACTOR SIMULATED USING DIFFERENT KINETIC MODELS	97

LIST OF SYMBOLS

Symbols that are not included in the list are explained on the spot. The units are stated as used in the equations. In case different units are used for better readability in tables and figures, these units are given in the according table or figure.

Latin Letters

A	Area	[m^2]
C	Cost	[\$]
\hat{C}_p	Heat capacity	[J/(mol K)]
D	Diffusion coefficient or diameter	[m^2/s], [m]
Ea	Activation energy	[J/mol]
h	Specific enthalpy	[J/mol]
j	Molar flux or molar flux acting on matter element	[mol/(m^2s)], [mol/s]
k	Reaction rate constant	various
K	Equilibrium constant or adsorption constant	various
L	Reactor length	[m]
M	Molecular weight	[Kg/mol]
n	Molar flow rate	[mol/s]
p	Pressure or parameter	[atm]
perm	Permeance	[mol/(Pa m^2s)]
q_{ex}	External heat flux or heat flux acting in fluid element	[W/ m^2], [W]
Q	Heat duty	[W]
R	Gas constant	[J/(mol K)]
r	Reaction rate	[mol/(Kg s)]
r	Measured reaction rate	[mol/(Kg s)]
S	Selectivity	[-]

STY	Space time yield	[mol/(m ³ s)]
T	Temperature	[K]
t	Time	[s]
V	Volume	[m ³]
x	Mole fraction	[-]
X	Conversion	[-]
z	Axial coordinate	[m]

Greek Symbols

α	Heat transfer coefficient	[W/(m ² K)]
ΔH	Reaction enthalpy	[J/mol]
η	Efficiency	[-]
ε	Catalyst void fraction	[-]
λ	Thermal conductivity or eigenvalue	[W/(m K)], [-]
λ_b	Stagnant contribution of thermal conductivity in packed bed	[W/(m K)]
λ_{th}	Threshold eigenvalue	[-]
M	Dynamic viscosity	[Kg/(m s)]
v	velocity	[m/s]
ρ	Density	[Kg/m ³]
θ	Dimensionless time or length	[-]

Subscripts

c	Coolant or catalyst or compressor
cond	Condenser
eq	Equilibrium
i	Component index
in	Inlet

j	Reaction index
g	Gas
mix	Mixture
out	Outlet
p	Particle
rem	Removed
rxn	Reaction
t	Tube
to	Outer tube
ti	Inner tube

1 Introduction

1.1 Motivation and scope

Limited fossil fuel reserves, high oil prices, insecure energy supply, as well as worldwide increase in environmental awareness are key factors that are driving the transition towards a renewable energy based economy. Electricity generated by harvesting renewable natural resources like wind or solar can significantly reduce, if not entirely eliminate, our dependence on fossil fuels. Nevertheless, the intermittent nature of the renewable sources, and subsequently the electrical power generated from them, makes *energy storage* a crucial component of any renewables-based energy system. The ‘Power-to-Chemicals’ concept presents an attractive option in this regard whereby renewable electrical power is stored in the form of energy carriers/chemicals for short or long periods of time and in large scale. Renewable electricity can be efficiently converted into H₂ via water electrolysis. Nevertheless, the already established infrastructure for natural gas storage and transportation, unlike the case with H₂, makes the further conversion of H₂ into Synthetic Natural Gas a preferential route within the ‘Power-to-Chemicals’ process chain. CO₂ obtained from flue gas or biogas can catalytically react with H₂ according to the equation below:



The recycling of emitted CO₂, which contributes to global warming, is another benefit derived from this process.

For the past several decades, the main industrial application of CO₂ methanation has been the purification of H₂-rich streams in various chemical processes e.g. ammonia synthesis. It was only until recently that CO₂ methanation was considered for the large scale production of SNG. The renewed interest in CO₂ methanation, within the scope of ‘power to gas’ applications, resulted in a significant increase in the number of relevant studies that exceeded 100 in 2014.⁵ These studies focused mostly on the preparation of highly stable and active catalysts and to less extent on the elucidation of the reaction mechanism, the development of reliable kinetic model, and the design of reactor/process as demonstrated by recent comprehensive reviews.⁵⁻⁷

This thesis addresses the less investigated engineering aspects of the CO₂ methanation process within the context of ‘power to gas’ applications. Its overall framework rests on two research pillars: (1) the model-based optimal design and operation of the CO₂ methanation process with main emphasis on the reaction section and (2) the development of comprehensive mechanistic kinetic model under conditions relevant to industrial operation.

1.2 Structure of the Thesis

The structure of the thesis is as follows:

- **Chapter 2** lays the theoretical groundwork of the thesis. The fundamentals of CO₂ methanation are discussed first with main focus on heterogeneous catalysts and the reaction mechanisms. Afterwards, an overview of reactor designs, reported in literature, for the production of Synthetic Natural Gas is introduced.
- In **chapter 3**, optimal Sabatier reactor design and operation is derived for maximum space-time yield by implementing a three-level reactor design procedure, which is based on the conceptual framework of the Elementary

Process Function methodology. Accordingly, the most promising performance enhancing concept is determined after solving a number of dynamic optimization problems. The concept is then approximated by two reactor configurations: (1) a cascade of polytropic multitubular fixed bed reactor with interstage condensers and (2) a polytropic hydrophilic membrane reactor. Ultimately, the best reactor configuration is technically realized and compared with other typical reactor configurations reported in literature for the production of SNG. Optimal temperature profiles with the reactors are successfully approximated. Moreover, optimal operating conditions and geometric dimensions of the reactor are determined.

- **Chapter 4** discusses the model-based optimization of the whole methanation process for reduced total cost, with main emphasis on the reaction section. The proposed process is comprised of a reaction section, represented by a cascade of multitubular reactor and intermediate condensers, and a glycol unit for downstream drying. In addition to the rigorous reactor model and the shortcut models used to describe all other process units, the formulated optimization problem also included cost models for the different process units. Because all the units in the process were simultaneously optimized, it was possible to account for the interaction between the various units when determining the cost optimal reactor design and operating conditions of the process.
- **Chapter 5** deals with the kinetic investigation of CO₂ methanation over commercial nickel-based catalyst. The experimental test rig used in performing steady state kinetic measurements under technically relevant conditions is presented first. Detailed derivation of mechanistic kinetic models based on elementary steps and in line with reported theoretical studies like the density functional theory are then introduced. Parameter estimation and model discrimination on the basis of the collected data is performed by choosing an objective function and discrimination criterion that are suitable for multi-

response systems. Afterwards, the quantitative identifiability of the most adequate model parameters is investigated and the prediction ability of the model is validated using a new set of data points. Finally, a comparison is made between this model and other models reported in literature by simulating an isothermally cooled packed bed reactor.

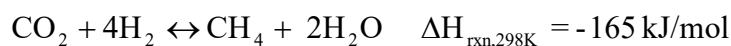
- **Chapter 6** draws the conclusions of this work and gives some recommendations for further work.

2 Theoretical background

This chapter discusses the fundamentals of CO₂ methanation reaction with main emphasis on the reaction mechanism, heterogeneous catalysts, and the reactors used for the production of Synthetic Natural Gas starting from carbon oxides.

2.1 Sabatier reaction

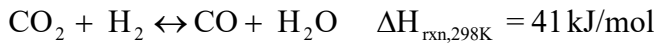
Chemical CO₂ methanation, also known as the Sabatier reaction, is a thermodynamically favored ($\Delta G_{\text{rxn},298\text{K}} = -113 \text{ kJ/mol}$) and highly exothermic ($\Delta H_{\text{rxn},298\text{K}} = -165 \text{ kJ/mol}$) reaction whereby CO₂ is hydrogenated to form CH₄ according to the following equations:



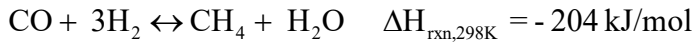
The chemical equilibrium of this reaction is dependent on pressure and temperature. Since methanation is an exothermic reaction with fewer moles of gaseous molecules on the product side than on the educts side, the formation of CH₄ is more thermodynamically favored at low temperature and high pressure (Le Chatelier principle).

In addition to the direct CO₂ methanation reaction, several other reactions can take place in parallel such as:

Reverse water gas shift reaction:



CO methanation reaction:



Boudouard reaction:



2.1.1 Heterogeneous catalysts

Although the Sabatier reaction is thermodynamically favored, it is kinetically limited and requires a catalyst to proceed at an acceptable rate. In 1902, Sabatier and Sanderens were the first to report the chemical catalytic hydrogenation of CO₂ towards CH₄.⁸ Since its discovery, several metals were found active for the methanation of CO₂ (e.g. Ni, Ru, Rh, Pd, Co). In order to maximize the catalyst utilization efficiency, these active metals are usually highly dispersed over various porous supports (e.g. Al₂O₃, SiO₂, TiO₂, CeO₂, ZrO₂, MgO).⁹ The activity and the selectivity of the catalyst towards CH₄ vary depending on: (1) the active metal used, its loading, and the dispersed particle size, (2) the type and structure of the support, (3) the method of preparation, and (4) the reduction procedure.

Graf et al. arranged the active metals based on their activity as follows: Ru > Fe > Ni > Co > Rh > Pd > Pt > Ir.⁹ Nevertheless, Ni-based catalysts continue to be the catalyst of choice in most industrial applications of CO₂ methanation due to their high activity, high selectivity towards CH₄, and relatively low cost. They are, therefore, the most widely investigated among the methanation heterogeneous catalysts. Here, only a number of recent studies are presented.

A high-loaded Ni-Al mixed oxide catalyst (ca. molar ratio Ni/Al = 5) was prepared, for the methanation of CO₂, by Abello et al. via conventional co-precipitation of the metal precursors.¹⁰ Despite the high Ni loading (ca. 70 wt. %), which is thought to have

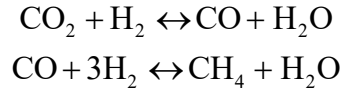
negative impact on the catalyst performance, high activity was reported. It was explained by the formation of small metallic nickel crystallites (ca. 6 nm) dispersed over NiO-alumina upon partial reduction of the mixed oxide. Moreover, the catalyst showed a CH₄ selectivity that is very close to 1. Rahmani et al. studied the effect of Ni loading on the CO₂ methanation activity of a mesoporous nanocrystalline γ -Al₂O₃ supported catalyst.¹¹ The results showed that the catalytic activity increased by increasing the Ni content from 10% to 20%. However, a further increase in the Ni content to 25% led to the formation of large particle size and consequently low dispersion, thus resulting in a decrease in the catalyst performance.

Aziz et al. prepared, by sol-gel and impregnation methods, a Ni catalyst supported on mesostructured silica nanoparticles (MSN) for the methanation of CO₂.¹² The authors then compared the prepared catalyst to other Ni catalysts supported on Mobile Crystalline Material (MCM-41), γ -Al₂O₃, SiO₂, and protonated Y zeolite (YH). The catalytic activity followed the order: Ni/MSN > Ni/MCM-41 > Ni/HY > Ni/SiO₂ > Ni/ γ -Al₂O₃. The high activity of the Ni/MSN was attributed to the presence of both intra- and inter-particle porosity which led to the high concentration of basic sites. The effect of various supports (CeO₂, α -Al₂O₃, TiO₂, and MgO) on Ni catalysts was also studied by Tada et al..¹³ The highest activity was observed for Ni/CeO₂ followed by Ni/ α -Al₂O₃, Ni/TiO₂, and Ni/MgO. The superior performance of Ni/CeO₂ arises from the favored CO₂ activation and reduction due to the oxygen vacancies on the CeO₂.¹⁴ By combining CeO₂ with ZrO₂ to form Ce_xZr_{1-x}O₂ solid solution, further improvements in the support properties such as excellent thermal stability, resistance to sintering, high redox property, and suppressing coke formation are achieved.⁷

2.1.2 Reaction mechanisms

In general, it is suggested that the methanation of CO₂ proceeds either via a direct route, in which CO₂ is reduced to CH₄ without the formation of intermediate CO, or via a

consecutive pathway comprising of reverse water gas shift, as a first reaction step, and CO methanation reaction according to the equations below:



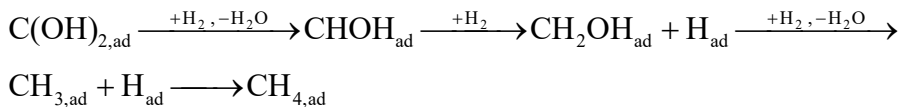
The dominant reaction pathway can generally vary depending on the reaction conditions and the catalyst used.¹⁵ This is reflected by a significant number of experimental and theoretical studies that aimed at elucidating the mechanism of CO₂ hydrogenation.

Using functional density theory, Bothra et al. investigated the mechanism of CO₂ methanation on Ni(100).¹⁶ In their study, the authors focused on two possibilities regarding the CO₂ hydrogenation step. The first possibility involved a reaction between adsorbed CO₂ and gaseous H₂ in an Eley Rideal mechanism (ER), yielding a carboxyl group that is further reduced to dihydroxyl intermediate:

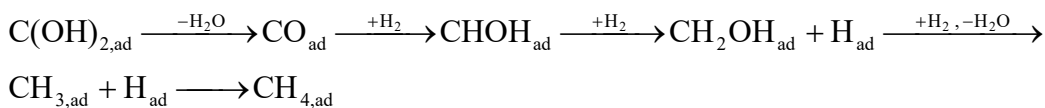


Starting from this intermediate, two reaction pathways (Path1A and Path1B) were explored:

Path1A



Path1B



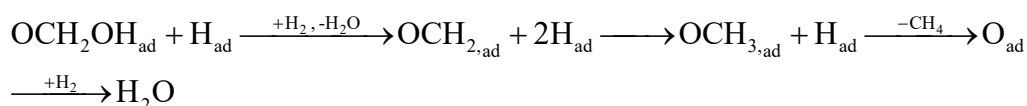
As can be seen, Path1B included CO intermediate.

The second possibility included the reaction of adsorbed CO₂ with adsorbed H₂ (Langmuir Hinshelwood mechanism (LH)) to form formate that is further reduced according to:

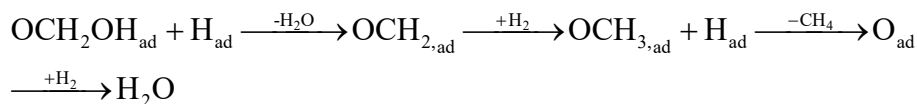


This intermediate follows two paths (Path2A and Path2B) each of which resulted in a methoxy intermediate that was eventually converted to CH₄:

Path2A



Path2B



Based on their calculations, among all these four pathways, Path1A has the lowest energy barrier.

The ‘direct’ reaction pathway for CO₂ methanation was suggested in only few experimental studies^{17–20} where zirconia and/or ceria oxides were used as catalyst support. For example, Schild et al. proposed a ‘direct route’ mechanism for CO₂ hydrogenation over Ni/ZiO₂.¹⁸ Their conclusion was supported by the results of a dynamic experiment in which CO₂/H₂ atmosphere was replaced by pure hydrogen. After switching the feed to pure hydrogen, CH₄ was still being produced while a decrease in the abundant surface formate was observed by means of in-situ DRIFT spectroscopy. Thus, it was suggested that intermediate formate was hydrogenated directly into methane. One should note that adsorbed CO, and not gaseous CO, was also detected during the experiments. Therefore, the existence of another route where CO could be the precursor to CH₄ couldn’t be excluded. It is worth noting that while formate is highly stable on nickel monocrystals,^{16,21} its conversion to CH₄ and H₂O can be facilitated depending on the catalyst support employed.²² It was reported that the Ce (III) sites of the ceria support, for instance, can promote the hydrogenation of the formate species.¹⁹

Aldana et al. studied the mechanism of CO₂ methanation on Ni catalyst supported on two different oxides (silica and zirconia-ceria) by means of operando IR spectroscopy.¹⁷ The study revealed different CO₂ conversion mechanism for ceria-zirconia supported and silica supported catalyst. The authors found that CH₄ formation and CO formation proceeded via two different pathways on Ni/zirconia-ceria, unlike the case with

Ni/silica. The formation of CH₄ independent of CO intermediate was ascribed to the activation of CO₂ by the weak basic sites of the zirconia-ceria support. Once CO₂ is activated, it is converted, by the hydrogen atom adsorbed on nickel, into intermediate formate and further into CH₄. This is in line with the results obtained by Pan et al. who investigated the reaction route of CO₂ methanation over ceria-zirconia supported and alumina supported nickel catalysts.²³ The authors detected two types of formates: The monodentate and the bidentate formate. The monodentate formate, which is faster to hydrogenate, was formed abundantly on the medium basic sites of the ceria-zirconia support. In contrast, minor monodentate formate species were observed on the alumina support which mostly exhibits strong basic sites. It was concluded that medium basic sites enhance CO₂ methanation activity and that CO₂ adsorbed on strong basic sites of Ni/ γ -Al₂O₃ will not participate in the reaction. Similar conclusions regarding the mechanism and the role of formate in the formation of CH₄ over zirconia supported nickel catalysts was reported by Solis-Garcia et al..²⁰

On the other hand, a larger number of studies (experimental and theoretical) considered CO an indispensable intermediate in the CO₂ methanation reaction.^{24,25} In 1982, Weatherbee and Bartholomew were the first to propose a mechanistic kinetic model based on the consecutive reaction scheme.²⁶ In a previous study, the authors reported that the rates of CO and CO₂ methanation over Ni/silica were the same at low temperature.²⁷ This was further supported by the results of Peebles et al., who found that the activation energy of CO₂ methanation over Ni (100) is in close agreement with CO methanation.²⁸ Aldana et al. also reported that the activity of Ni/silica was comparable for both CO and CO₂ methanation at 673 K.¹⁷ Zagli and Falconer performed temperature programmed experiments for both CO and CO₂ methanation over Ni/silica.²⁹ As the two reactions showed identical reaction spectrum, it was concluded that both reactions proceed via the same mechanism. The mechanism of CO₂ methanation on carbon supported nickel catalyst was investigated by Lapidus et al. using isotopic, steady state, and transient techniques.³⁰ During the different experiments, CO was

always produced along with CH₄ and H₂O. On the basis of the data collected, especially by means of the transient experiments, the authors concluded that CO is an essential intermediate in CH₄ formation.

In a more recent study, Garbarino et al. studied CO₂ methanation over various Ni/alumina catalysts.³¹ It was concluded that fast methanation occurs at the expense of CO intermediate on the corners of nanoparticles interacting with alumina likely with a ‘via oxygenate’ mechanism. In addition to the many experimental studies, theoretical calculations also supported the intermediacy of CO in the hydrogenation of CO₂ to CH₄. Ren et al. investigated three different mechanism for CO₂ methanation on Ni (111) using Density Functional Theory (DFT), two of which involve the formation of CO intermediate.³² According to the first mechanism, CO₂ reacts with H to produce HCOO species. Formate then dissociates into CO which is subsequently hydrogenated to CH₄. In the second mechanism, CO₂ decomposes first to CO and then to C which is eventually hydrogenated to CH₄. On the contrary, the third mechanism follows the direct route: CO₂ reacts with H to produce C(OH)₂ species which dissociates into CH₂O and then into CH₂ species. It was reported that, among the three mechanisms, the second mechanism was the most favorable with the lowest energy barrier.

2.1.3 Reactors

The typical reactor used for methanation is the fixed bed reactor.⁶ In hydrogen and ammonia synthesis processes where methanation is used as a purification step, the reactors are generally operated adiabatically³³. This is possible due to the small amount of carbon oxides available for the reaction. However, for large scale production of SNG where the feed is rich with carbon oxides and where high conversion is desired, then the adiabatic reactors must be combined with intermediate cooling steps. Indeed, a series of 2-6 adiabatic fixed bed reactors with intermediate cooling and/or recycling of the product as well as isothermal fluidized bed reactors were the main reactor concepts used in the ‘coal/biomass to SNG’ processes.³⁴

Recently, the adiabatic reactor/intercoolers concept was adopted for the ‘power-to-gas’ CO₂ methanation process. De Saint Jean et al. proposed a process design that was

comprised of a high temperature steam electrolysis unit, a methanation unit, and a gas purification unit.^{35,36} The methanation unit consisted of a series of 4 adiabatic reactors with intermediate cooling steps and one condensation step between reactor 3 and 4. Shaaf et al. developed two different reaction concepts for methanation plants.³⁷ The first concept consisted of two reactors with intermediate condensation, while the second concept consisted of one reactor but with 6 reaction stages and four gas intercooling steps.

Apart from using adiabatic reactors, one can significantly enhance the performance of the Sabatier reactor by tailoring the temperature inside using external coolant. Kievit and Thöming computed the optimal axial temperature profile inside a single fixed bed reactor using the Semenov Number Optimization method.³⁸ Their results showed that the methane yield was improved by two folds compared to adiabatic and isothermal operation. SolarFuel proposed a cascade of two polytropic tube bundle reactors and one intermediate condensation step.³⁹ Jürgensen et al. investigated, using Aspen Plus Dynamic, the dynamic behavior of an externally countercurrent cooled multitubular methanator integrated into a biogas plant. The study revealed that one reactor with CH₄ rich feed is sufficient to produce a grid quality gas mixture based on the Wobbe index and the CO₂ composition specifications.⁴⁰ Schelerth and Hinrichsen compared the model predictions of different pseudo-homogeneous models and a heterogeneous model of an externally cooled tubular packed bed reactor in addition to a membrane reactor for CO₂ dosing.⁴¹ The study showed that a 1-D pseudo homogeneous model is capable of describing the qualitative trends of the reactor and can be used for evaluating the process conditions. However, a 2-D model is more suited for comparison with experiments. Excellent temperature control could be achieved in the membrane reactor by feeding H₂ and CO₂ in a separated and controlled manner.

In addition to fixed bed reactors, three phase reactors were also considered for CO₂ methanation due to their good heat dissipation and tolerance to rapid load change. Nevertheless, slurry bubble column reactor has one major disadvantage and that is the liquid side mass transfer limitation which reduces the effective reaction rate.⁴² Lefebvre et al. experimentally investigated the performance of the reactor under both steady and dynamic operation and determined the optimal process conditions for SNG production.⁴³ The results confirmed the rapid adaptation of this reactor to changes in the

feed. Götz et al. proposed a reaction concept consisting of two reactors in series: an isothermal slurry bubble reactor and a polytropic honeycomb reactor with one intermediate condensation step.⁴⁴ The three phase reactor acts as a buffer for load changes whereas full conversion is achieved in the honeycomb reactor, thus, producing a gas mixture with CH₄ composition of more than 95%.

The microchannel methanators were also proposed by different researchers for space-related applications. Brooks et al. developed a microchannel reactor with active side wall cooling using oil.⁴⁵ The reactor was designed for applications related to the propellant production on Mars or space habitat air revitalization. The reactor consisted of two parallel columns of 15 rectangular microchannels each. Another reactor was developed by Holladay et al. also for an in situ propellant production (ISPP) system.⁴⁶ It consisted of 7 reaction microchannels interleaved with eight cooling ones. However, the catalyst suffered from deactivation due to sintering and loss of surface area.

The significant potential of membrane fixed bed reactors in the methanation of CO₂ was experimentally demonstrated by Ohya et al. who reported an increase in conversion by 18 % upon using a hydrophilic membrane reactor. One drawback of this reactor was the permselectivity of its integrated membrane which was a ceramic tube coated with a thin layer of microporous glass.⁴⁷ The membrane was not only permeable to H₂O but also to all the other components with H₂ having the highest permeable flux. According to Ohya et al., the predominant mechanism of the permeation of H₂, CH₄, and CO₂ is Knudsen flow while that of water vapor is surface diffusion.

3 Model-based optimal design and operation of the Sabatier reactor

This chapter focuses on the optimal design and operation of the Sabatier reactor under process-wide constraints and within the conceptual framework of the Elementary Process Function methodology. The design aims at producing high quality gas mixture that is suitable for direct injection into the NG grid following a downstream drying step, without the need for any additional separation steps (Figure 3.1). This way, the overall SNG production cost can be significantly reduced since purification steps of multi component systems are known to be the most power consuming operations. The availability of highly selective catalysts towards CH₄ (up to 100%)⁵ makes the proposed process design feasible. It should be noted, however, that the downstream drying step is an indispensable component of the process because the NG grid quality specifications demand an extremely low water content. Drying the produced SNG to the desired water content can be achieved using molecular sieve or glycol systems. These techniques are already applied in the natural gas processing plants and can reduce the water content to less than 0.1 ppm.^{48,49}

The reactor is optimally designed and operated for maximum space-time yield by following a procedure that is comprised of three design levels. At each level,

optimization problems of increasing complexity are formulated and solved. The decisions made on each of the three levels are illustrated in Figure 3.2.

3.1 Level 1

On this level, predefined apparatuses are avoided. The reactor is represented by a matter element whose thermodynamic state is influenced, along the reaction coordinate, by external *unlimited* heat and component fluxes ($q_{ex}(t)$, $j_i(t)$) and an internal reaction flux ($r_{rxn}(t)$). The external fluxes are control variables that are optimized to ensure the best reaction conditions (e.g. T , p , x_i) over the entire reaction time. To systematically investigate the influence of dosing or extracting certain components on the STY, different cases, or integration concepts, are considered. For each case, only specific fluxes are enabled to manipulate the thermodynamic state of the matter element (Table 3.5).

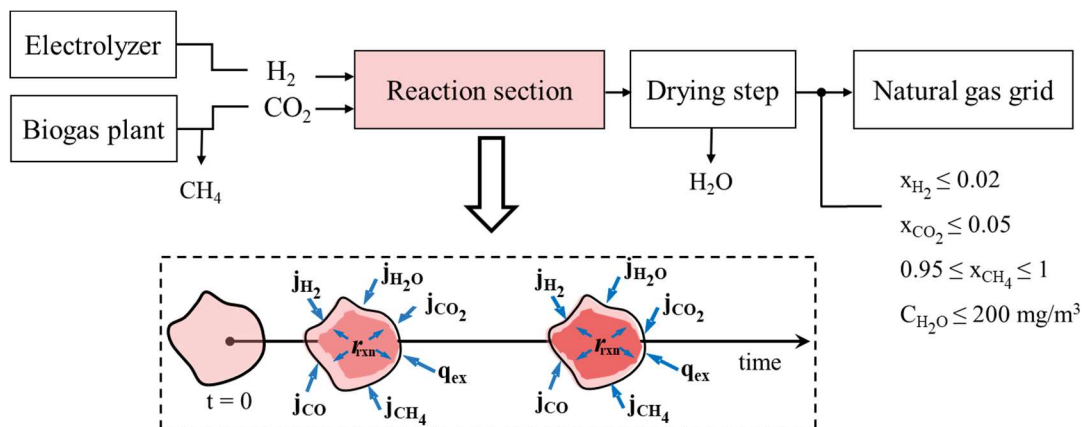


Figure 3.1 The general scheme of the proposed Sabatier process with the reaction step depicted, according to the EPF approach, by the fluid element.

It should be noted that the aim, on this level, is to reveal and compare quantitatively the *maximum potential* of the different integration concepts. Therefore, no technical or transport kinetic limitations are enforced on the external fluxes at this stage. In other words, $j_i(t)$ and $q_{ex}(t)$ can be varied unrestrictedly so that any temperature and concentration profiles are obtainable. As for the internal flux ($r_{rxn}(t)$), it is defined by the kinetic model of Xu and Froment who studied the intrinsic kinetics of CO₂ methanation

over nickel based catalyst.⁵⁰ The developed rate expressions are of Langmuir-Hinshelwood type and are applicable in the temperature range of 573-673 K and a pressure range of 1-10 atm:

$$r_{COMeth} = \frac{\frac{k_1}{P_{H_2}^{2.5}} (K_{COMeth} P_{H_2}^3 P_{CO_2} - P_{CH_4} P_{H_2O})}{DEN^2} \quad (3.1)$$

$$r_{RWGS} = \frac{\frac{k_3}{P_{H_2}} (K_{RWGS} P_{H_2} P_{CO_2} - P_{CO} P_{H_2O})}{DEN^2} \quad (3.2)$$

$$r_{CO_2Meth} = \frac{\frac{k_3}{P_{H_2}^{3.5}} (K_{CO_2Meth} P_{H_2}^4 P_{CO_2} - P_{CH_4} P_{H_2O}^2)}{DEN^2} \quad (3.3)$$

$$DEN = 1 + K_{CO} P_{CO} + K_{H_2} P_{H_2} + K_{CH_4} P_{CH_4} + \frac{K_{H_2O} P_{H_2O}}{P_{H_2}} \quad (3.4)$$

According to the Arrhenius equation and van Hoff equation, the rate and adsorption constants are calculated respectively as follows:

$$k_j = k_{0,j} \exp\left(\frac{-E_{a,j}}{RT}\right) \text{ where } j = 1, 2, \text{ and } 3 \quad (3.5)$$

$$K_i = A_i \exp\left(\frac{-\Delta H_i}{RT}\right) \text{ where } i \in \{H_2, CH_4, CO, H_2O\} \quad (3.6)$$

The respective parameters are given in Table 3.1 and Table 3.2.

Table 3.1 Parameters of the rate constants as reported by Xu et al.

j	k ₀	E _a [kJ/mol]
1	4.225×10 ¹⁵	240.1
2	1.955×10 ⁶	67.13
3	1.020×10 ¹⁵	243.9

Table 3.2 Parameters of the adsorption constants as reported by Xu et al.

i	A	ΔH [kJ/mol]
H ₂	6.12×10 ⁻⁹	-82.9
H ₂ O	1.77×10 ⁵	88.68
CH ₄	6.65×10 ⁻⁴	-38.28
CO	8.23×10 ⁻⁵	-70.65

3.1.1 Model formulation

The optimal reaction route, i.e. the optimal temperature and concentration profiles, associated with each integration concept (Table 3.5) is determined by formulating and solving the respective dynamic optimization problem. The optimization problem is constrained by ordinary differential equations (Mass and energy balances), algebraic equalities (thermodynamic equations, kinetics), inequalities (e.g. quality specifications), and intrinsic bounds.

First, the optimization problem is converted, using orthogonal collocation on finite elements, into a Non Linear Programming (NLP). The NLP is then solved, based on the simultaneous approach, using CONOPT. CONOPT is a generalized reduced-gradient solver that is based on the sequential quadratic programming and is efficient in solving large scale NLP problems. In our case, CONOPT was implemented in AMPL.

The matter element is assumed to be randomly packed with spherical catalyst particles with a void fraction $\varepsilon=0.38$. It is described using a pseudohomogeneous model consisting of component mass and energy balance equations.

The component mass balance is defined as:

$$\frac{dn_i}{dt} = \sum_j \mathcal{G}_{ij} \cdot r_j \cdot \rho_c \cdot \frac{(1-\varepsilon)}{\varepsilon} V_g + b_i j_i \quad (3.7)$$

$$\text{where } b_i = \begin{cases} 1 & \text{for dosing of component i} \\ 0 & \text{no dosing/removal of component i} \\ -1 & \text{for removal of component i} \end{cases}$$

Since the maximum pressure is 10 atm, ideal gas behavior can still be a valid assumption. The gas volume is calculated using the ideal gas law:

$$V_g = \frac{1}{1.013 \times 10^5} \frac{n_i RT}{p} \quad (3.8)$$

It is assumed that the CO₂ feed is supplied free of CH₄ by an average sized biogas plant (1100 Nm³/hr, see Table 3.3). The inlet H₂ to CO₂ ratio, inlet temperature, and inlet pressure are decision variables and are bounded as follows:

$$2.7 \leq x_{H_2,in} / x_{CO_2,in} \leq 5.1$$

$$1 \leq p_{in} \leq 10 \text{ atm}$$

$$573 \leq T_{in} \leq 673 \text{ K}$$

Table 3.3 Composition of the biogas

Component	CH ₄	CO ₂	O ₂	H ₂ O
Mole fraction	0.64	0.325	0.01	0.025

The upper and lower bounds of the pressure and temperature are chosen as such in order to ensure the validity of the kinetic model. Moreover, the effluent composition is defined in accordance with the German quality specifications of the gas mixture that can be injected directly into the NG grid or used as fuel for cars (DVGW G260/A, 2013 and DIN 51624):

$$0 \leq x_{H_2,out} \leq 0.02$$

$$0 \leq x_{CO_2,out} \leq 0.05$$

$$0.95 \leq x_{CH_4,out} \leq 1$$

$$0 \leq C_{H_2O,out} \leq 200 \text{ mg} / \text{m}^3$$

The energy balance is formulated in terms of temperature. It is assumed that the change of enthalpy due to extraction/dosing of compounds and change in pressure is negligible compared to the heat released by the reaction or the heat exchanged (q_{ex}). This is a reasonable assumption considering the high exothermicity of the methanation reaction. Since q_{ex} is assumed to be unlimited as mentioned earlier, the temperature of the reaction is free to vary within the applicable range of the kinetic study ($573 \leq T \leq 673 \text{ K}$). An optimal temperature profile over the residence time can thus be achieved.

$$\sum_i n_i \hat{C}_{p,i} \frac{dT}{dt} = -(q_{ex} + \sum_j \Delta H_{rxn,j} r_j \rho_c \frac{1-\varepsilon}{\varepsilon} V_g) \quad (3.9)$$

The component molar heat capacity is estimated using temperature dependent formulas reported in Yaws.⁵¹ The heat capacity constants for the various components are presented in Table 3.4.

$$\hat{C}_{p,i} = A_i + B_i T + C_i T^2 + D_i T^3 + E_i T^4 \quad (3.10)$$

The objective function is defined as:

$$STY = \frac{n_{CH_4,prod}}{\int_0^\tau \frac{V_g}{\varepsilon} dt} \quad (3.11)$$

Table 3.4 Heat capacity constants for the different components

i	A	B	C	D	E
H ₂	25.399	2.0178×10 ⁻²	-3.8549×10 ⁻⁵	3.188×10 ⁻⁸	-8.7585×10 ⁻¹²
CO ₂	27.437	4.2315×10 ⁻²	1.9555×10 ⁻⁵	3.9968×10 ⁻⁹	-2.987×10 ⁻¹³
CH ₄	34.942	-3.9957×10 ⁻²	1.9184×10 ⁻⁴	-1.5303×10 ⁻⁷	3.9321×10 ⁻¹¹
H ₂ O	33.933	-8.4186×10 ⁻³	2.9906×10 ⁻⁵	-1.7825×10 ⁻⁸	3.6934×10 ⁻¹²
CO	29.556	-6.5807×10 ⁻³	2.0130×10 ⁻⁵	-1.2227×10 ⁻⁸	2.2617×10 ⁻¹²

As for the drying unit, its rigorous modeling exceeds the scope of this chapter. Therefore, it is described using a simple mass balance while assuming that the produced gas mixture is dried to the desired water content.

The general description of the dynamic optimization problem is given below:

$$\max \quad STY$$

$$q_{ex}(t), j_i(t)$$

s.t:

- Component mass and energy balance equations
- Chemical kinetics
- Chemical reaction engineering bounds
- Intrinsic bounds
- State equations
- Mass balance for the downstream drying step

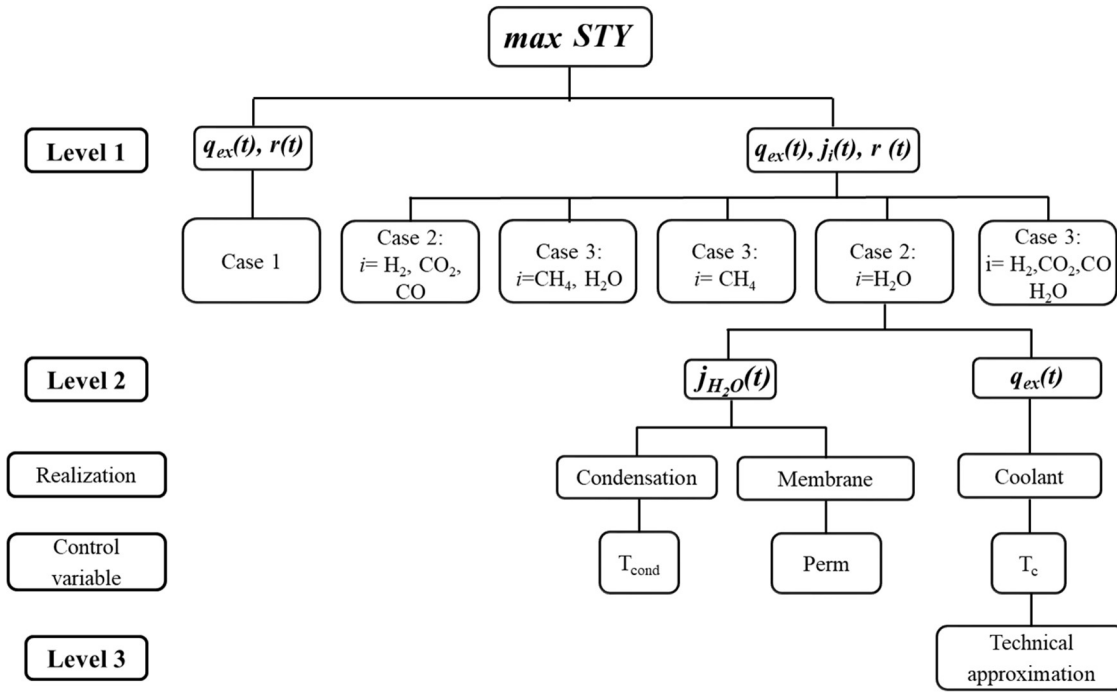


Figure 3.2 The decision structure of the Sabatier reactor design based on the EPF methodology

3.1.2 Results and discussion

Table 3.5 summarizes the optimization results of the most representative integration concepts. The results show that the desired outlet composition (product quality specifications), based on the ‘reaction and downstream drying’ scheme (Figure 3.1) and under the investigated temperature range, can not be met by applying cooling only (Case 1) or by combining cooling with dosing/extracting any of the reactants over the reaction time (Case 2).

Table 3.5 Level 1: Heat and component fluxes integrated in the different studied cases and the respective space-time yield obtained

Control variables	$q_{ex}(t)$	$j_{H_2O}(t)$	$j_{CH_4}(t)$	$j_{H_2}(t)$	$j_{CO_2}(t)$	$j_{CO}(t)$	STY
Case 1	×						Inf.
Case 2	×			×	×	×	Inf.
Case 3	×	×	×				256
Case 4	×		×				49
Case 5	×	×					33
Case 6	×	×		×	×	×	33

This is owed to the fact that for the produced gas to meet the NG grid specifications, almost complete conversion ($X > 99\%$) should be achieved in the reaction section. However, this level of conversion can not be realized in the aforementioned cases due to thermodynamic limitation.

Figure 3.3 shows the optimal temperature profile of Case 1, after disabling the product quality constraint, versus conversion. As can be seen, the temperature remains constant at its upper limit ($T = 673$ K) for a maximally enhanced reaction rate before it starts to decrease gradually, at $X = 92\%$, to $T = 573$ K. This decrease in temperature allows a maximum conversion of $\approx 98\%$ to be reached with $STY = 1.67$ mol/(m³ s). At this level of conversion, additional measures need to be taken in order to meet the product quality specifications such as recycling part of the effluent or extending the temperature range to lower values. In any case, these two measures will lead to a further decrease in the STY.

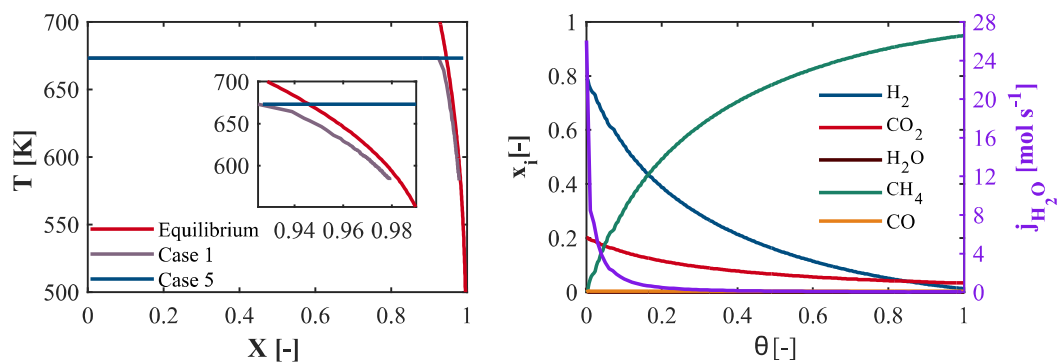


Figure 3.3 Results of Level 1; Optimal temperature profiles of Case 1 and Case 5 (left). Optimal profile of H₂O extraction and mole fraction of Case 4 (right)

A feasible solution exists only if one or all the products are extracted (Cases 3-6). By extracting H₂O (Case 5), CH₄ (Case 4), or both (Case 3), the equilibrium is shifted towards the product side according to the Le Chatelier principle. For instance, Figure 3.3 (left) shows that almost complete conversion is achieved in Case 5 while the optimal temperature is kept at the upper bound (673 K) for maximum enhancement of the reaction rate. By comparing the STY obtained for the different investigated cases, one

can see that the extraction of both CH₄ and H₂O combined with cooling (Case 3) represents the best integration concept with a STY of 256 mol/(m³ s). Furthermore, the STY values clearly show that extracting CH₄ (STY=49 mol/(m³ s), Case 4) is more advantageous than the optimal removal of H₂O (STY=33 mol/(m³ s), Case 5). This can be explained by examining the rate expression, more specifically, the adsorption equilibrium constants of H₂O and CH₄ which represents the 'resistance' terms in the rate equation. The larger they are, the slower is the reaction rate. Over the operating temperature range, the adsorption equilibrium constant of CH₄ is larger than that of H₂O by two orders of magnitude. Therefore, eliminating the CH₄ adsorption term by CH₄ removal has a bigger impact on enhancing the reaction rate.

Also, dosing H₂, CO₂, or CO over the reaction time is not favored ($j_{CO}(t)=j_{CO_2}(t)=j_{H_2}(t)=0$) as indicated by the result of Case 6. The STY calculated for this case (STY=33 mol/(m³ s), see Table 3.5) is equal to that achieved in Case 5.

Overall, it can be concluded that the removal of CH₄ and H₂O along the reaction coordinate can significantly increase the STY and that active cooling is essential to control the temperature within the reactor since the reaction is highly exothermic.

3.1.2.1 Technical feasibility of the best integration concept

While external coolant can be used, for instance, to keep the reactor temperature at the desired value, finding the technical means to extract both CH₄ and H₂O from the reaction system can be more challenging. Generally, the extraction of CH₄ from gas mixtures can be realized using various membranes or adsorption/absorption systems. For instance, specifically designed molecular sieves are reported to be able to retain CH₄ without hindering the flow of CO₂, H₂O, and H₂S in biogas process plant.⁵² However, the application of this technology to our system is not so promising since about 10% of CH₄ is lost in this process, and it is not clear whether these molecular sieves would also retain H₂ in addition to the retained CH₄. Furthermore, this extraction process is bulky and energy intensive particularly with respect to the regeneration of the

molecular sieves. Membrane technology is a more interesting option in this regard. Membranes are already used in biogas treatment to separate CO₂ from CH₄. However, such membranes allow the permeation of CO₂ rather than CH₄ and therefore can't be used to extract CH₄ from our reaction system.

A process for the separation of methane from a H₂ and CO gas stream was invented by Raman et al.⁵³ It is based on the separation of CH₄ by converting it into CH₄ hydrate. The separation is possible because CO don't form hydrates with H₂ unlike CO₂ which form hydrates easily. This is why such process can't be used for this reaction system. To sum up, to our knowledge, no already applied or simple technology for the extraction of CH₄ from a H₂/CO₂ mixture exists.

On the other hand, several methods are available for the extraction of H₂O whether continuously or in discrete manner like the adsorption and absorption columns (e.g. Molecular sieves, Glycol), hydrophilic membranes, and condensers. Compared to the adsorption and absorption units, applying condensers or membranes within the reaction step requires lower operating and investment costs.

3.1.2.2 Most promising integration concept: Active cooling and H₂O removal

Based on the above, the most promising and technically feasible integration concept is the removal of H₂O coupled with cooling (Case 5). The optimal profile of j_{H_2O} and the component mole fraction versus the reaction time for Case 5 are shown in Figure 3.3. As can be seen, H₂O needs to be continuously removed to keep its content minimal over the entire reaction time. The maximum amount of H₂O is removed at the beginning of the reaction when the reaction rate is the highest. Initially, j_{H_2O} is at approximately 27 mol/s and then it gradually decreases, along the reaction time, close to zero with the decrease in the reaction rate.

3.2 Level 2

At this level, only the most promising reaction concept of Level 1 (Case 5: $q_{ex}(t), j_{H_2O}(t)$) is further investigated with respect to the 'mechanisms' with which the optimal flux

profiles of Level 1 can be realized. Accordingly, these fluxes are not *unlimited* anymore. They are now governed by constitutive equations based on which suitable control variables are selected to attain the desired $q_{ex}(t)$ and $j_{H_2O}(t)$.

With regard to the removal of H₂O, two options are considered. The first one is water condensation where the amount of water removed is controlled by the condenser temperature. The second option is the in-situ and continuous removal of water by means of a hydrophilic membrane. In this case, the membrane permeance is used to optimize the amount of water being extracted over the entire reaction time.

As for the heat flux, it is realized by an external coolant and is controlled, along the reaction coordinate, by the coolant temperature. In terms of reactor configuration, this results in: (1) a cascade of polytropic multitubular reactor with intermediate condensation steps and (2) a polytropic membrane reactor.

3.2.1 Reactor cascade with interstage condensation

Condensation is one of the most common and simplest H₂O separation techniques. The high volatility of H₂, CH₄, CO₂, and CO enables the separation to be highly selective without any significant losses in other components of the reaction mixture.

The integration of the chemical reaction and condensation in one unit will allow the continuous extraction of H₂O as desired and depicted in Figure 3.3. However, the relatively high temperatures at which methanation is usually operated (570-600 K) makes water condensation possible only at very high pressures (>100 atm). On one hand, this can be extremely expensive. On the other hand, the formation of water films on the catalytic surface will lead to significant mass transfer resistances. Hence, interstage condensation steps in a cascade of polytropic reactors is instead considered in this work.

3.2.1.1 Model formulation for the reactors

Since the objective is to maximize the STY, a catalyst configuration that allows maximum catalyst density inside the reactor is considered i.e. randomly packed spherical catalytic particles.

The inlet mole fraction and total molar flow rate for the first reactor in the cascade are decision variables. Other variables for every reactor in the cascade include: the catalyst particle diameter, reactor tube diameter, the inlet temperature, inlet pressure, and coolant temperature. The upper and lower bound of these variables are given below:

$$1 \leq D_p \leq 30 \text{ mm}$$

$$1 \leq D_t \leq 30 \text{ cm}$$

$$573 \leq T_{in} \leq 673 \text{ K}$$

$$1 \leq p_{in} \leq 10 \text{ atm}$$

The reactors are described using a 1D pseudo homogeneous plug flow model. According to Schlereth and Hinrichsen,⁴¹ a 1D pseudo-homogeneous model is able to describe the qualitative trends of the reactor and can be used for evaluating the process conditions.

It is assumed that the reactors are operating under steady state, the axial diffusion is negligible compared to axial convection, and that there is no radial gradient in concentration, temperature, and velocity.

The STY is defined as:

$$STY = \frac{\dot{n}_{CH_4, prod}}{\frac{\pi}{4} D_t^2 \int_0^\tau v_{int} dt} \quad (3.12)$$

The composition of the different compounds is calculated using the component mass balance equation:

$$\frac{d(\rho_i v_{int})}{dt} = \sum_j \mathcal{G}_{ij} r_j \rho_c \frac{(1-\varepsilon)}{\varepsilon} M_i v_{int} \quad (3.13)$$

As for the interstitial velocity profile, it is calculated using the conservation of the total mass flow rate:

$$v_{\text{int}} = \frac{\rho_{g,\text{in}} v_{\text{int},\text{in}}}{\rho_g} \quad (3.14)$$

The superficial velocity is calculated from the interstitial one using:

$$v_s = \varepsilon v_{\text{int},\text{in}} \quad (3.15)$$

The same assumptions made for the energy balance in Level 1 are applied in this level as well.

$$\rho_g C_p \frac{dT}{dt} = - \left(\frac{4}{\varepsilon D_t} q_{\text{ex}} + \sum_j \Delta H_{\text{rxn},j} r_j \rho_c \frac{1-\varepsilon}{\varepsilon} \right) \quad (3.16)$$

As mentioned earlier, the heat exchange between the reaction segment and the coolant section is now limited and is governed by the following transport kinetic equation:

$$q_{\text{ex}} = \alpha (T - T_c) \quad (3.17)$$

The overall heat transfer coefficient is calculated by accounting for the heat transport resistance adjacent to the tube wall and through the packed bed as suggested by de Wasch and Froment.⁵⁴

$$\frac{1}{\alpha} = \frac{1}{\alpha_w} + \frac{D_t}{8\lambda} \quad (3.18)$$

The correlation used for computing the heat conduction through the packed bed or the wall heat transfer coefficient is based on a stagnant and a dynamic contribution.

The heat conduction through the bed is calculated, using the equations provided by Tsotsas,⁵⁵ as follows:

$$\lambda = \lambda_b + \frac{Pe\lambda_g}{8} \quad (3.19)$$

$$Pe = \frac{v_{\text{int}} \rho_g C_{p,g} D_p}{\lambda_g} \quad (3.20)$$

The specific heat capacity of the gas mixture is calculated using:

$$C_p = \sum_{i=1}^s y_i \frac{\hat{C}_{pi}}{M_i} \quad (3.21)$$

The stagnant contribution, λ_b , is calculating using Eq. (3.22-3.24).

$$\lambda_b = (1 - \sqrt{1-\varepsilon} + \sqrt{1-\varepsilon} k_c) \lambda_g \quad (3.22)$$

$$k_c = \frac{2}{N} \left(\frac{B}{N^2} \frac{k_p - 1}{k_p} \ln \frac{k_p}{B} - \frac{B+1}{2} - \frac{B-1}{N} \right) \quad (3.23)$$

$$N = 1 - \left(\frac{B}{k_p} \right), \quad k_p = \frac{\lambda_p}{\lambda_g}, \quad B = 1.25 \left(\frac{1-\varepsilon}{\varepsilon} \right)^{\frac{10}{9}} \quad (3.24)$$

The wall heat transfer coefficient is calculated using the correlations of Martin and Nilles according to:⁵⁶

$$\alpha_w = \left[\left(1.3 + \frac{5D_p}{D_t} \right) \frac{\lambda_b}{\lambda_g} + 0.19 \text{Re}^{0.75} \text{Pr}^{0.33} \right] \frac{\lambda_g}{D_p} \quad (3.25)$$

The pressure drop inside the reactor is calculated using Ergun equation:

$$\frac{dp}{dt} = - \left[150 \mu_g \frac{(1-\varepsilon)^2}{D_p^2 \varepsilon^3} + 1.75 \frac{v_s \rho_g (1-\varepsilon)}{D_p \varepsilon^3} \right] \frac{v_s^2}{\varepsilon} 10^{-5} \quad (3.26)$$

The equation reported by Jeschar et al.⁵⁷ is used to calculate the bed porosity:

$$\varepsilon = 0.375 + 0.34 \frac{D_p}{D_t} \quad (3.27)$$

The temperature difference between the reaction mixture and coolant was restricted to ≤ 30 .

In order to ensure a plug flow, the following constraint is enforced:

$$\frac{D_t}{D_p} \geq 10 \quad (3.28)$$

A general criterion for the absence of significant intraparticle and interphase temperature and concentration gradient developed by Dogu et al.⁵⁸ (Eq. (3.29)) was enforced as a constraint over the entire reaction time. This ensured that the reactors are very well described by the pseudo-homogeneous model with an effectiveness factor, η_c , between 1 and 1.05. The advantage of this criterion is its applicability to all forms of kinetic expressions and not just to power models.

$$\left| -\frac{D_p^2}{4} (F_{MTL} + F_{HTL}) \right| < 0.75 \quad (3.29)$$

$$F_{MTL} = \sum_{i=1}^5 \frac{(\partial r_j / \partial C_i)_{C_{i,bulk} T_{bulk}}}{r_{j,bulk} D_{im}} \left(\sum_{j=1}^3 r_j \mathcal{G}_{ij} \right) (1 + 5Bi_{mass,i}^{-1}) \quad (3.30)$$

$$F_{HTL} = \frac{(\partial r_j / \partial (1/T))_{C_{i,bulk} T_{bulk}} \left(\sum_{j=1}^3 r_j \Delta H_{rxn,j} \right) (1 + 5 Bi_{heat}^{-1} \beta)}{r_{j,bulk} \lambda_p T_{bulk}^2} \quad (3.31)$$

$$\beta = \left(1 - \frac{D_p}{6 \alpha_p T_{bulk}} \right) \left(\sum_{j=1}^3 r_j \Delta H_{rxn,j} \right) \quad (3.32)$$

$$Bi_{mass,i} = \frac{D_p k_{c,p}}{2 D_{i,m}} \quad (3.33)$$

$$Bi_{heat} = \frac{D_p \alpha_p}{2 \lambda} \quad (3.34)$$

where α_p is the heat transfer coefficient between the particle and the fluid. It is calculated using the correlation provided for spherical particles by Wakao et al..⁵⁹ The thermal conductivity of the catalyst particle, λ_p , is assumed to be equal to 5 [W/(m K)].

The diffusion coefficient of component i diffusing in a mixture of gases forming a stagnant film, D_{im} , is calculated using the equation proposed by Wilke:⁶⁰

$$D_{i,m} = \frac{1 - x_i}{\sum_{j=1, j \neq i}^5 \frac{x_j}{D_{ij}}} \quad (3.35)$$

The binary diffusion coefficient is calculated using the empirical correlation of Fuller et al..⁶¹

The fluid to particle mass transfer coefficient, $k_{c,p}$, is calculated using the Sherwood correlation of Wakao et al..⁵⁹

$$Sh = 2 + 1.1 Sc^{0.33} Re^{0.6} \quad (3.36)$$

3.2.1.2 Model formulation for the condensers

The phase separation in the condenser is calculated using an equilibrium flash model as reported by Biegler.⁶² Since the sizing of the condenser is beyond the scope of this study, the energy balance of the condenser is not considered here.

The overhead split factor of water, defined as $\xi_{H_2O} = \frac{\dot{n}_{H_2O,v}^{cond}}{\dot{n}_{H_2O,f}^{cond}}$ and the condenser temperature are decision variables ($0 \leq \xi_{H_2O} \leq 1$, $298 \leq T^{cond} \leq 400$ K). The pressure in the condenser is equal to the outlet pressure of the reactor preceding it. The split factor of the other components are calculated using Eq. (3.37-3.44).

$$\xi_i = \frac{\omega_{i,H_2O} \xi_{H_2O}}{1 + (\omega_{i,H_2O} - 1) \xi_{H_2O}} \quad (3.37)$$

$$\omega_{i,H_2O} = \frac{K_{i,cond}}{K_{H_2O,cond}} \text{ for } i \in \{H_2, CO, CO_2, CH_4\} \quad (3.38)$$

$$K_{H_2O,cond} = \frac{p_{H_2O}^{sat}}{p \times 760} \quad (3.39)$$

$$\log(p_{H_2O}^{sat}) = A + \frac{B}{T} + C \log(T) + DT + ET^2 \quad (3.40)$$

with $A=29.8605$, $B=-3.1522 \times 10^3$, $C=-7.3037$, $D=+2.4247 \times 10^{-9}$, and $E=1.8090 \times 10^{-6}$.

The phase distribution constants, defined as $K_i^{cond} = \frac{x_{i,v}^{cond}}{x_{i,l}^{cond}}$ are used to account for the solubility of the gaseous components in the liquid phase. These are calculated using temperature-dependent correlations developed by Fernandez-Prini et al. (see Eq.(3.41-3.44)).⁶³ The coefficients for calculating the phase distribution constants are presented in Table 6.

$$\ln(K_i^{cond}) = qF_i + \frac{E_i}{T^{cond}} f(\tau) + (F_i + G_i \tau^{2/3} + H_i \tau) \exp\left(\frac{273.13 - T^{cond}}{100}\right) \quad (3.41)$$

$$f(\tau) = \frac{\rho^*(l)}{\rho_c} - 1 \quad (3.42)$$

$$\frac{\rho^*(l)}{\rho_c} = 1 + b_1 \tau^{1/3} + b_2 \tau^{2/3} + b_3 \tau^{5/3} + b_4 \tau^{16/3} + b_5 \tau^{43/3} + b_6 \tau^{110/3} \quad (3.43)$$

$b_1=1.99274064$, $b_2=1.09965342$, $b_3=-0.510839303$, $b_4=-1.75493479$, $b_5=-45.5170352$, and $b_6=-6.74694450 \times 10^5$

$$\tau = 1 - \frac{T^{cond}}{T_c} \text{ with } T_c = 647.1 \quad (3.44)$$

Table 3.6 Coefficients for calculating the phase distribution constant

i	E	F	G	H
H ₂	2286.4159	11.3397	-70.7279	63.0631
CO ₂	1672.9376	28.1751	-112.4619	85.3807
CH ₄	2215.6977	-0.1089	-6.6240	4.6789
CO	2346.2291	-57.6317	204.5324	-152.6377

The reactors, condensation steps, and the drying step are all included in the optimization problem which has the following general form:

$$\begin{aligned} \max \quad & STY \\ & T_c(t), D_p, D_t, p_{in} \\ & T_{in}, \xi_i, T_{cond}, x_{i,in} \end{aligned}$$

s.t:

- Total mass balance
- Component mass balance
- Chemical reaction kinetics
- Energy balance
- Momentum balance
- Transport kinetics
- State equations
- Intrinsic bounds: e.g. temperature, tube diameters.
- Initial and outlet compositions
- Design criteria equations
- Dew point equation
- Mass balance for the dehydration process

3.2.1.3 Results and discussion

The optimal profile of j_{H_2O} obtained in Level 1 can be realized by assuming a sequence of infinite number of condensation steps. However, this is not practical. Therefore, reactor cascades of up to 6 condensation steps are considered here. Their respective STY values are shown in Figure 3.4.

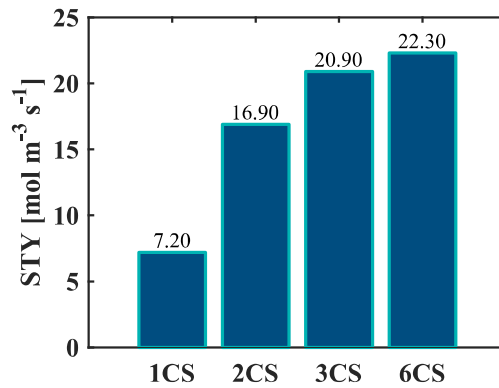


Figure 3.4 STY calculated for the different cascades

As anticipated, increasing the number of condensation steps per cascade, increases the STY. The magnitude of the incremental increase in STY, however, is shown to be diminishing. For a cascade of two reactors and one condensation step, the STY calculated is 7.2 mol/(m³ s). This value increases by more than 100% for a cascade of two condensation steps (2CS). On the other hand, despite doubling the number of condensation steps from three to six steps, the STY increases by less than 7% only, reaching a value of 22.3 mol/(m³ s). This is still lower than the STY calculated for case 5 in Level 1 (33 mol/(m³ s)). As a result of the additional constraints and the technical limitations introduced in Level 2, the optimal profiles of the mole fraction and temperature of Level 1 could not be completely realized leading to losses in the STY ($\approx 30\%$).

It can be deduced, based on the results shown in Figure 3.4, that a cascade of more than three condensation steps will not be economically attractive due to the minor increase in the STY in return of the expected additional operating and investment cost of the units. Consequently, the most promising configuration is the 3CS cascade and will therefore be further analyzed in more details.

As expected, the optimal temperature of all three condensers is at the lower bound ($T_{\text{cond}}=298\text{ K}$) with the split factor of H₂O being close to zero. This indicates that the H₂O is mostly in the liquid phase (see Table 3.7), thus resulting in the negligible H₂O mole fraction at the inlet of Reactors 2, 3, and 4 as shown in Figure 3.5.

Table 3.7 Optimal operating conditions and inlet/outlet gas composition of condensers 1, 2, and 3

Condenser	C1	C2	C3
T [K]	298	298	298
ξ [-]	[1, 1, 1, 0, 1]	[1, 1, 1, 0, 1]	[1, 1, 1, 0, 1]
{H ₂ ,CO ₂ ,CH ₄ ,H ₂ O,CO}			
$x_{i,in}$ [-]	[0.5, 0.13, 0.12, 0.25, 0]	[0.14, 0.05, 0.42, 0.4, 0]	[0.05, 0.03, 0.8, 0.1, 0]
{H ₂ ,CO ₂ ,CH ₄ ,H ₂ O,CO}			
$x_{i,out}$ [-]	[0.66, 0.17, 0.16, 0, 0]	[0.22, 0.074, 0.7, 0, 0]	[0.06, 0.04, 0.9, 0, 0]
{H ₂ ,CO ₂ ,CH ₄ ,H ₂ O,CO}			

The figure also shows that the mole fraction of H₂O is relatively high in Reactor 1 and Reactor 2 where most of the reactants are converted ($X_{R1}=0.5$, $X_{R2}=0.92$). On the other hand, the water content is very low in Reactors 3 and 4. As a result, the thermodynamic limitation is overcome and almost complete conversion is reached ($X_{R4}=0.995$). Notably, the CO mole fraction was always near zero throughout the reaction time.

The gas mixture leaving Reactor 4 has a mole fraction of: 0.02 for H₂, 0.028 for CO₂, 0.928 for CH₄ and 0.023 for H₂O. The composition of H₂ and CO₂ already meet the pipeline specifications. The mole fraction of CH₄ is near the desired value while that of H₂O is much larger than the allowed value. The NG quality specifications of the produced gas mixture are met, nevertheless, after it is processed in the downstream drying unit.

The inlet pressure in all the reactors is at the upper bound (10 bar). This is expected since high pressure is favored for thermodynamic and kinetic reasons. On the one hand, it shifts the equilibrium, according to Le Chatelier principle, towards the product side allowing higher level of H₂ conversion. On the other hand, it increases the rate of the reaction.

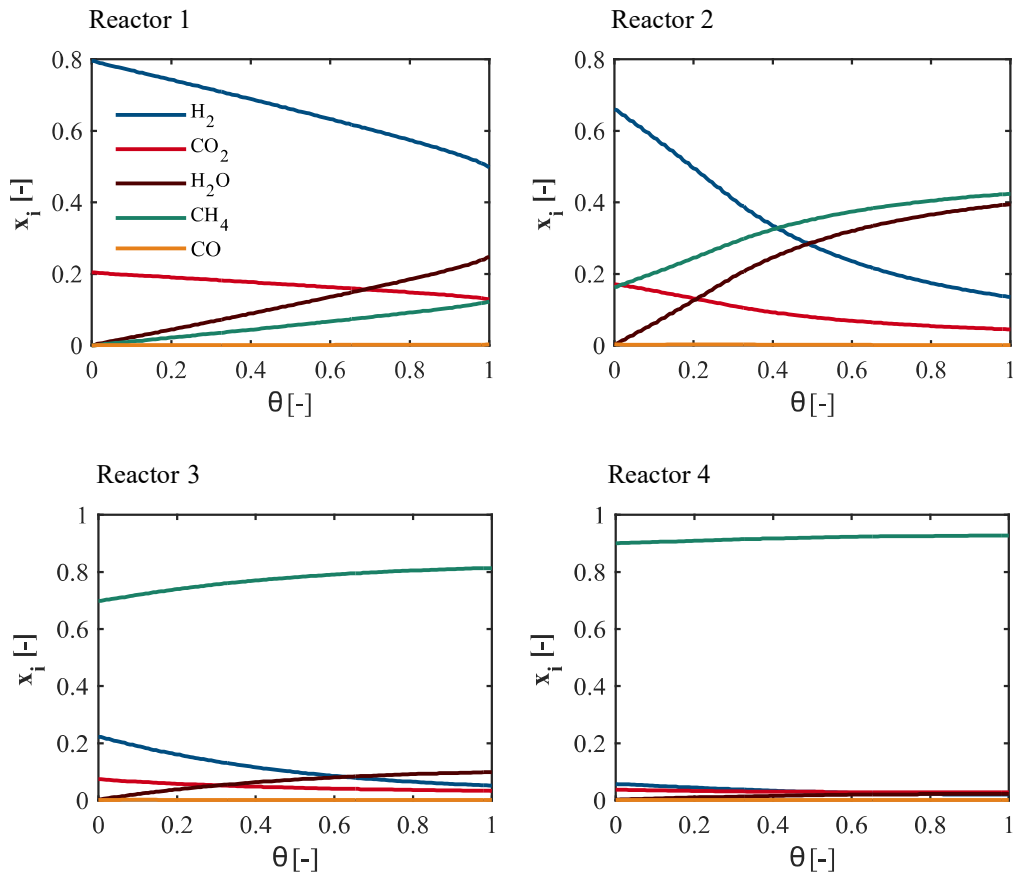


Figure 3.5 Results of 3CS cascade of Level 2, Component mole fraction profile in the four reactors.

Figure 3.6 shows the optimal profile of the coolant temperature and the resulting temperature of the gas mixture in the 4 reactors. The inlet temperature of the gas mixture is 619 K in Reactor 1. It increases gradually in parallel with the coolant temperature until it reaches the upper limit (673 K) at the outlet of the reactor. The temperature difference between the coolant and the mixture is kept at the maximum allowed value i.e. 30 K for most efficient heat transfer. This is expected since the reaction is highly exothermic and the reaction rate is maximum in Reactor 1 (highest concentration of reactants). The obtained temperature profile differs qualitatively and quantitatively from the optimal temperature profile of Level 1 where the temperature was kept constant at 673 K. This is due to the fact that in Level 1 it was assumed that the heat flux is unlimited i.e. any amount of heat released could be removed very rapidly. The heat flux of Level 2 is however limited by the heat transport kinetics (Eq. (3.17)) as mentioned earlier.

The lower inlet reactant concentration of Reactor 2 compared to that of Reactor 1 means a lower reaction rate and consequently less amount of heat released. Therefore, a comparatively higher inlet temperature of the gas mixture for Reactor 2 is possible ($T_{R2,in}=649$ K). The mixture temperature then increases moderately along with the coolant temperature. A temperature difference of 30 K is maintained over the first 30% of the reactor residence time. Afterwards, the temperature difference starts to diminish as the mixture temperature is kept constant at 673 K.

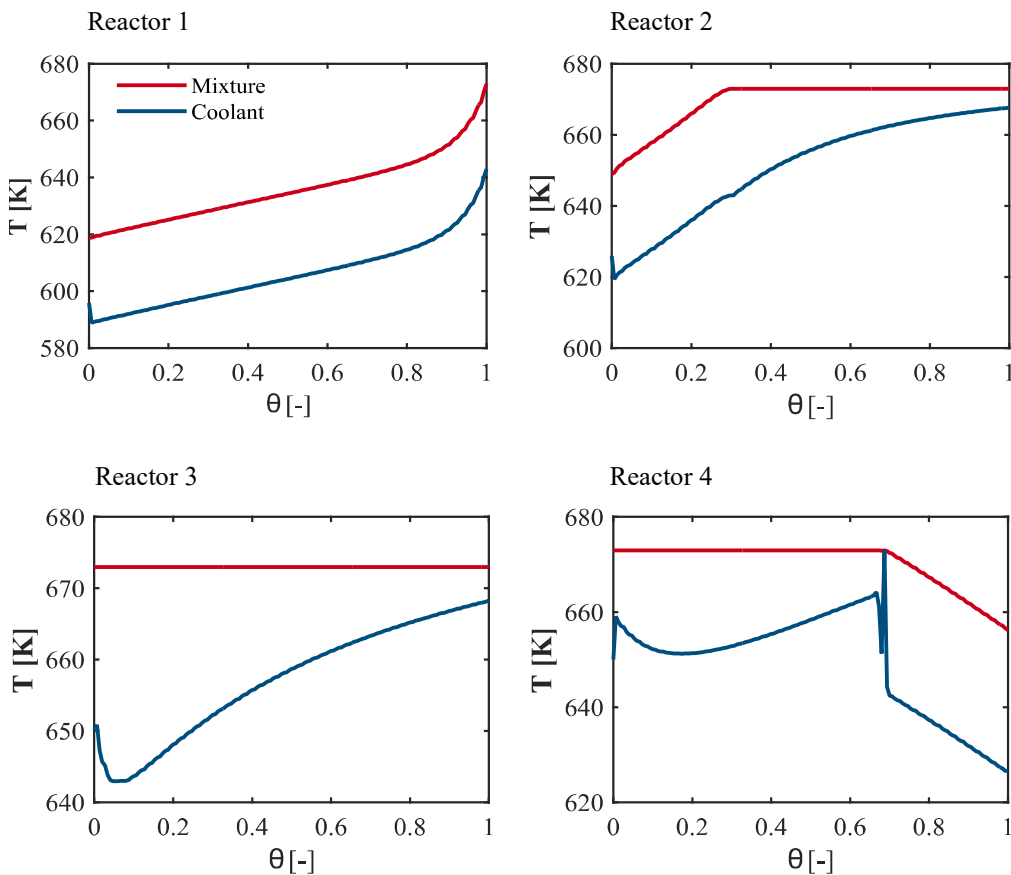


Figure 3.6 Results of 3CS cascade of Level 2, coolant and reaction mixture temperature profile in the four reactors

Since most of the H₂ conversion is achieved in Reactors 1 and 2 ($X_{R1}=0.5$, $X_{R2}=0.92$), the amount of heat released in Reactors 3 is comparatively insignificant. The temperature can thus be maintained, throughout the reactor, at the upper limit (673 K) by gradually increasing the coolant temperature.

A similar optimal temperature profile is obtained for the gas mixture in Reactor 4. The temperature stays constant at 673 K until the dimensionless time, θ , reaches 0.7. It then decreases steadily to 656 K in order to achieve the desired conversion ($X=0.995$). By examining the coolant temperature profiles in Reactor 1, 2, and 3, one can deduce that a co-current flow heat exchange should be employed to technically approximate the optimal temperature profiles. In contrast, Reactors 4 can be coupled with either isothermal or counter current cooling. The sharp increase in the coolant temperature which is observed at $\theta=0.7$ seems could be a result of a numerical error.

3.2.2 Membrane reactor

The membrane reactor is a process intensification concept that offers an inherent ability to combine reaction and water extraction in one single unit. As a result, it provides the advantage of compactness compared to the interstage condensation approach discussed earlier.

Several hydrophilic membranes are available for in-situ removal of water. However, for the membrane to be suitable for this application, it needs to have high permeance, high H₂O permselectivity, and very good thermal and mechanical stability. A hydroxy sodalite (H-SOD) membrane which was synthesized by Khajavi et al.⁶⁴ has such characteristics. For instance, this membrane only allows very small molecules such as helium, ammonia, and water (kinetic diameters 2.6, 2.55, and 2.65Å respectively) to permeate through. Owing to this unique window diameter, absolute separation of water from hydrogen streams can therefore be achieved. Moreover, it can operate at temperature as high as 723 K⁶⁵ and at a pressure up to 24 bar⁶⁶ which covers the operating range of methanation.

3.2.2.1 Model for Membrane packed bed Reactor

The membrane packed bed reactor is modeled in a similar way as the packed bed reactors of the aforementioned cascade configuration. But some equations are modified

to count for the specific geometrical and mechanistic characteristics of the membrane reactor.

The STY is defined based on the total volume of the membrane reactor as follows:

$$STY = \frac{\dot{n}_{CH_4,prod}}{\frac{\pi}{4} D_{to}^2 \int_0^\tau v_{int} dt} \quad (3.45)$$

The component mass balance now include a term for the mass transport through the membrane:

$$\frac{1}{v_{int}} \frac{d(\rho_i v_{int})}{dt} = \frac{4D_{ii}}{\varepsilon(D_{to}^2 - D_{ii}^2)} j_i M_i + g_i r_{rxn} \rho_c \frac{(1-\varepsilon)}{\varepsilon} M_i \quad (3.46)$$

The mass flux through the membrane is described by a phenomenological transport kinetic model. The water molar flux is proportional to the permeance and to the partial pressure difference across the membrane according to the equation:

$$j_{H_2O} = 1.013 \times 10^5 \times Perm(p_{H_2O} - p_{H_2O,s}) \quad (3.47)$$

The *Perm* is a decision variable with which the water flux is controlled. It is allowed to vary within realistic bounds: $10^{-8} \leq Perm \leq 10^{-6}$ mol/(m² Pa s). These bounds were chosen based on the permeance values of the state-of-the-art hydrophilic membranes reported in literature.⁶⁷ The flow rate of the sweep gas (e.g. air) is assumed to be very high that its water mole fraction is considered negligible. This means maximum driving force for H₂O permeation which results in the determination of the maximum potential of this proposed reactor concept.

The interstitial velocity profile is determined by solving the continuity equation:

$$\frac{1}{v_{int}} \frac{d(\rho_g v_{int})}{dt} = \frac{4D_{ii}}{\varepsilon(D_{to}^2 - D_{ii}^2)} \sum_{i=1}^5 j_i M_i \quad (3.48)$$

The energy balance for the reaction channel is defined as:

$$\rho_g C_p \frac{dT}{dt} = - \left(\frac{4D_{to}}{\varepsilon(D_{to}^2 - D_{ii}^2)} q_{ex} + \sum_{j=1}^3 \Delta H_{rxn,j} r_j \rho_c \frac{1-\varepsilon}{\varepsilon} \right) \quad (3.49)$$

One needs to note that, according to this three-level design concept, the detailed reactor design is considered only in Level 3. Therefore, the modeling of the permeate side will

not be considered in this level (Level 2) but in Level 3 if the STY is higher than that of the reactor-condenser cascade.

The void fraction of the reaction side is calculated using the equation reported by Dutoit et al.:⁶⁸

$$\varepsilon = 0.3517 + 0.387 \frac{D_p}{D_{to} - D_{ti}} \quad (3.50)$$

The general form of the optimization problem is given below:

$$\begin{aligned} \max \quad & STY \\ & T_c(t), D_p, D_{ti}, D_{to}, \\ & p_{in}, T_{in}, Perm(t), x_{i,in} \end{aligned}$$

s.t:

- Total mass balance
- Component mass balance
- Chemical reaction kinetics
- Energy balance
- Momentum balance
- Transport kinetics
- State equations
- Intrinsic bounds e.g. temperature, tube diameters
- Initial and outlet compositions
- Mass balance for the drying unit

3.2.2.2 Results and discussion

The optimal profile of the membrane permeance and the resulting H₂O flux profile are shown in Figure 3.7 (top). As expected, the permeance remains constant at its upper bound (10⁻⁶ mol/(m² Pa s)) over the entire reaction time for maximum water removal rate. The water flux increases with the increase in the H₂O mole fraction from zero at the beginning of the reaction to a maximum of 0.37 mol/m² around $\theta=0.2$. It then decreases gradually to almost zero towards the end of the reaction time in a close resemblance to the H₂O mole fraction.

As shown from Figure 3.7 (middle), most of the H₂ is converted in the dimensionless reaction time between 0 and 0.2. Consequently, a steady increase in the mixture temperature, starting from T=602 K, is observed. Over this time period, the temperature difference between the reaction gas mixture and the coolant is kept at 30 K. The mixture temperature remains at 673 K till $\theta=0.66$ before it decreases towards the end of the reaction similar to the temperature profiles observed in reactor 4 of the reactor-condenser cascade. It finally reaches 653 K.

Based on the coolant temperature profiles, the desired mixture temperature profiles can be technically realized by assuming two reaction segments. For the first segment, Co-current heat exchange should be applied for the first reaction segment whereas counter current for the second one (see Figure 3.7 (bottom)).

The membrane reactor achieved a STY of 7.31 mol/(m³ s) at a H₂ conversion of 0.995. The STY is almost four times lower than the value obtained in Case 5 of Level 1. The significant decrease in the STY is related to the transport limitations introduced in Level 2 on the heat and water fluxes (Eq. (3.17), Eq. (3.47)). Since heat removal is now limited, the ideal isothermal operation of the reactor at 673 K (Case 5 of Level 1), is not feasible anymore. Instead, the inlet mixture temperature has to be as low as 602 K before it increases gradually to 673 K. Moreover, because the H₂O flux is now limited by the permeance of the membrane, H₂O cannot be extracted as efficiently as in Level 1. One can see that the H₂O mole fraction is significantly above zero most of the reaction time.

As in the case of the reactor-condenser cascade, the gas mixture leaving the membrane reactor needs to undergo downstream drying process before it can be injected into the NG grid. Regarding the inlet pressure, it is also at its upper bound.

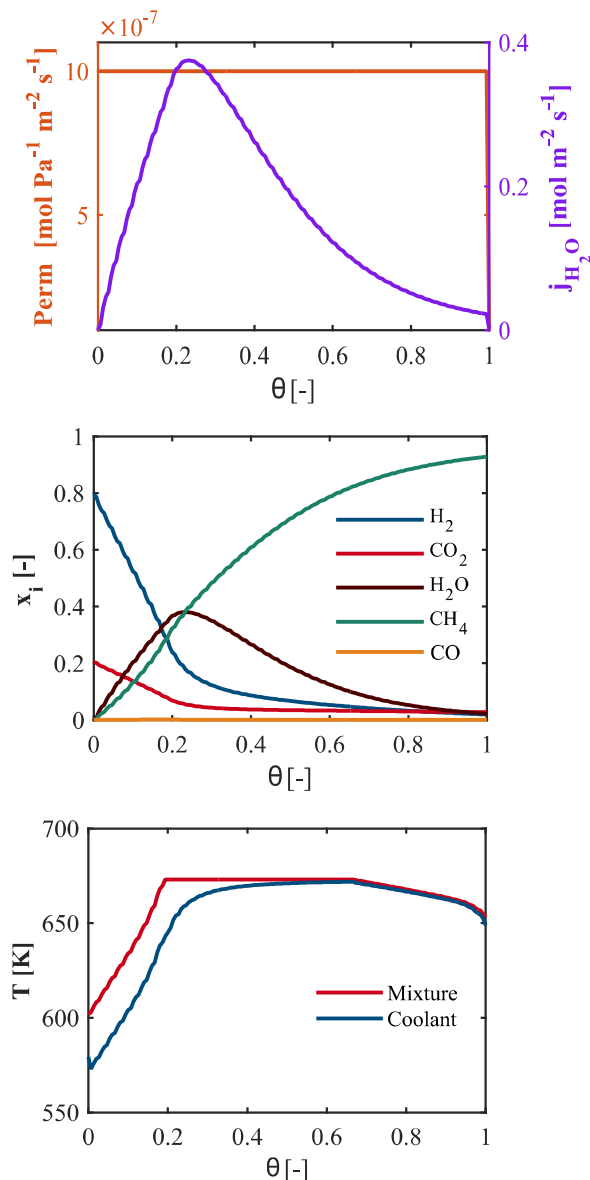


Figure 3.7 Results of Membrane reactor. From top to bottom: Permeance and water flux optimal profile, component mole fraction profile, optimal temperature profile of the coolant and the reaction mixture.

3.2.3 Comparison between reactor cascade and membrane reactor

Due to its limited permeance, the membrane reactor shows a slightly better performance than the reactor-condenser cascade which included only one condensation step (1CS cascade). The 3CS cascade (see Figure 3.8), on the other hand, achieves a STY that is more than 150% larger than that of the membrane reactor. It is therefore considered the most attractive reactor configuration for the methanation of CO_2 . In order for the

membrane reactor to show a better performance than the reactor-condenser cascade, the permeance of the membrane should be improved significantly.

3.3 Level 3

Based on the results of Level 2, the technical feasibility of the 3CS cascade is further investigated. In this level, the decision variable profiles (T_c) of the 4 reactors are technically approximated and realized. The change in coolant temperature is now defined by the energy balance of the cooling section. This additional constraint will reduce the degrees of freedom of the optimization problem. The heat flux can't be optimized anymore and only the inlet conditions (T_{in} , p_{in}) and other design variables (e.g. D_t , D_p) are optimized. As one would expect, this will result in a further decrease in the STY compared to Level 2. Moreover, at this level, a comparison is made between the derived optimal reactor design and operating conditions, and other reactor designs typically used for the methanation reaction: (1) a series of 6 adiabatic reactors with intercooling steps and (2) a single polytropic fixed bed reactor.

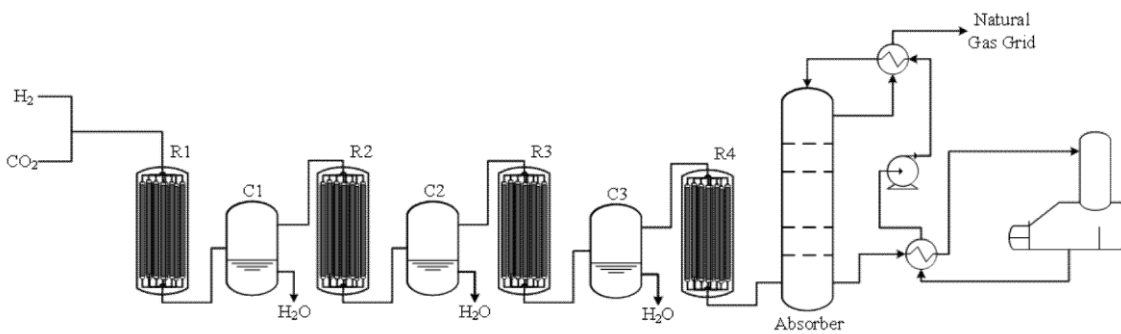


Figure 3.8 Schematic representation of the 3CS cascade integrated with the dehydration process

3.3.1 Model formulation for 3CS reactor cascade

The same equations and bounds of Level 2 are applied here as well. However, the balance equations are formulated in the Eulerian formulation:

$$\frac{d(\rho_i v_i)}{dz} = \left(\rho_c \frac{1-\varepsilon}{\varepsilon} M_i \right) \sum_j v_{ij} r_j \quad (3.51)$$

$$\rho_g C_p \frac{dT}{dz} = - \left(\frac{4}{d_t \varepsilon} q_{ex} + \sum_j \Delta H_j r_j \rho_c \frac{(1-\varepsilon)}{\varepsilon} \right) \frac{1}{v_i} \quad (3.52)$$

$$\frac{dp}{dz} = - \left(150 \mu_g \frac{(1-\varepsilon)^2}{d_p^2 \varepsilon^3} + 1.75 \frac{v_s \rho_g (1-\varepsilon)}{d_p \varepsilon^3} \right) v_s \quad (3.53)$$

The energy balance of the coolant is described using a simplified 1D equation. The coolant used is molten salt NaNO₂ (HITECH[®] from BRENNTAG) which is suitable for high temperature applications (149-538 °C). The mass flow rate of the coolant, \dot{m}_c , is a decision variable. The heat capacity of the coolant is $C_{p,c}=1.5616$ kJ/(kg K).

$$\dot{m}_c C_{p,c} \frac{dT_c}{dz} = \pi D_t q_{ex} \quad (3.54)$$

3.3.2 Results and discussion

Figure 3.9 shows the temperature profiles of the gas mixture and the coolant in the four reactors.

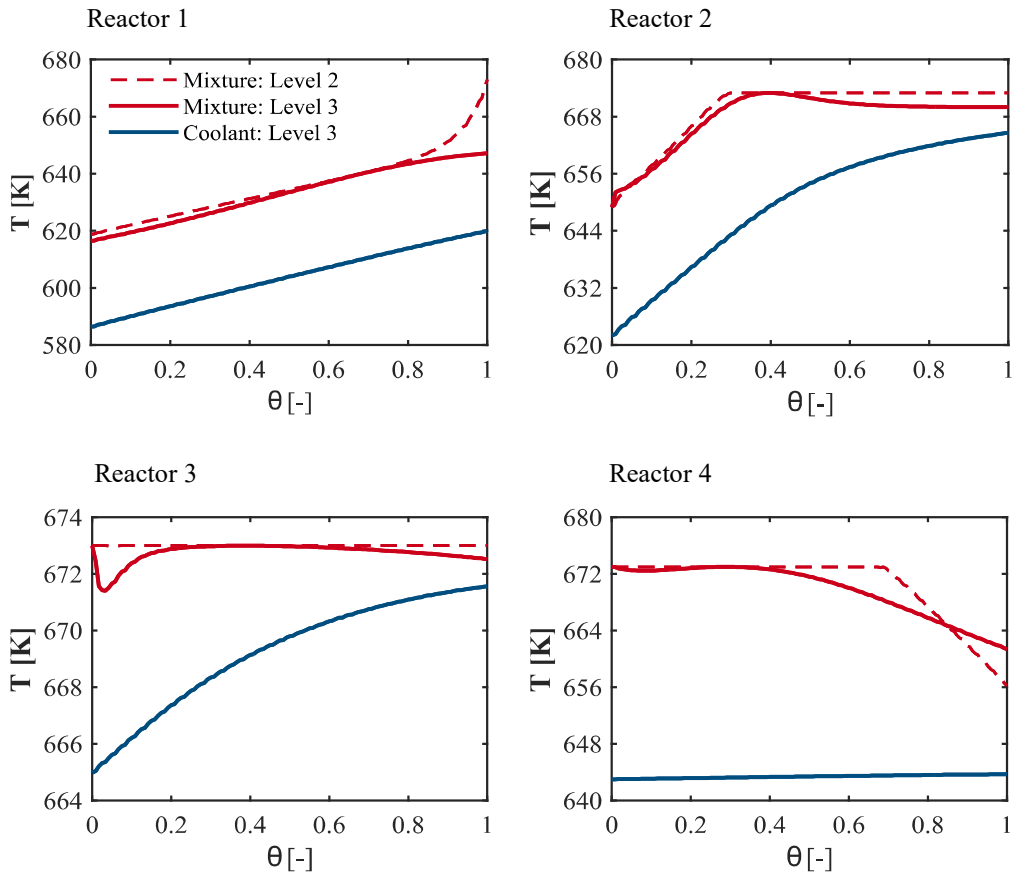


Figure 3.9 Results of 3CS cascade of level 3, coolant and reaction mixture temperature profile in the four reactors

The profiles look closely similar to the ones of Level 2, which implies that using co-current heat exchangers for reactors R1, R2, and R3 and isothermal cooling for R4 were reasonable technical approximations of the optimal coolant temperature profiles of Level 2. As a result of that, the STY obtained in Level 3 was only slightly lower, by 6 %, than the one obtained in Level 2 (see Figure 3.10).

The geometric dimensions and operating conditions of the four multitubular reactors are shown in Table 3.8. As can be seen, the length of the reactors is much larger than their respective diameter. This is especially true for the first and second reactors where most of the H₂ is converted and consequently most of the heat is released. This geometry provides large surface area to volume ratio thus enhancing the heat exchange and allowing better control of the reaction temperature.

Table 3.8 The geometric design and operating conditions of the different reactors in the 3CS cascade

Reactor	R1	R2	R3	R4
D_t [cm]	1.6	1.4	1.3	2.4
D_p [mm]	1.6	1.4	1	1
L [m]	0.95	1.6	1.85	0.29
p_{in} [atm]	10	10	10	10
T_{in} [K]	616	652	673	673
T_{out} [K]	647	670	672.5	661
$T_{c,in}$ [K]	552	622	665	643
$T_{c,out}$ [K]	620	665	672	644
$x_{i,in}$ [-]	[0.796,0.204,	[0.648,0.169,0.178,	[0.233,0.076,	[0.059,0.037,
{H ₂ ,CO ₂ ,CH ₄ ,H ₂ O,CO}	0,0,0]	0.003, 0]	0.69,0.003,0]	0.9,0.003,0]
$x_{i,out}$ [-]	[0.479,0.125,	[0.146,0.048,	[0.053,0.034,	[0.02,0.028,
{H ₂ ,CO ₂ ,CH ₄ ,H ₂ O,CO}	0.13,0.26,0]	0.430,0.375,0]	0.808,0.105,0]	0.928,0.023,0]
X_{out} [-]	0.52	0.92	0.98	0.995
$\dot{n}_{t,in}$ [mol/s]	0.08	0.047	0.021	0.017

The particle diameter is at or very close to the lower bound (1 mm) in all four reactors. The smaller the particle diameter, the lower is the heat and mass transfer resistance and the higher is the catalyst efficiency. Moreover, the smaller the particle diameter, the smaller is the bed porosity and the higher is the catalyst density.

The pressure drop inside each reactor was kept less than 1 atm. The inlet mole fraction of the 1st reactor was an optimization variable ($x_{in,H_2}=0.795$, $x_{in,CO_2}=0.205$).

Figure 3.10 shows the STY of the 3CS reactor configuration as well as the STY obtained using: (1) an optimized cascade of adiabatic reactors with intercooling steps (Adiab) but without water condensation and (2) an optimal single packed bed reactor with external cooling. It should be noted that to obtain a meaningful design of the two reference cases (Adiab and Poly), the temperature ranges were extended to higher values.

Still, the 3CS reactor configuration showed a much superior performance, especially in comparison with the adiabatic cascade. Moreover, the results show that the temperatures within the reactors of the 3CS cascade can be better controlled, without the formation of hotspot, in contrast to the polytropic reactor which registered a very steep increase in the temperature. Avoiding hotspots is crucial for lengthening the life of the catalyst.

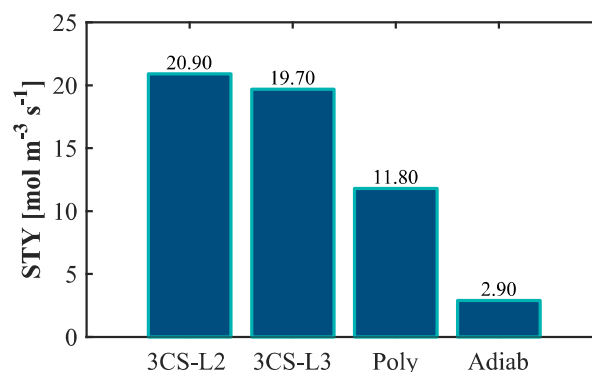


Figure 3.10 Space time yield obtained by our optimal reactor cascade with three condensation steps in Level 2 (3CS-L2) and Level 3 (3CS-L3) and by other reactor designs (adiabatic cascade and single polytropic reactor)

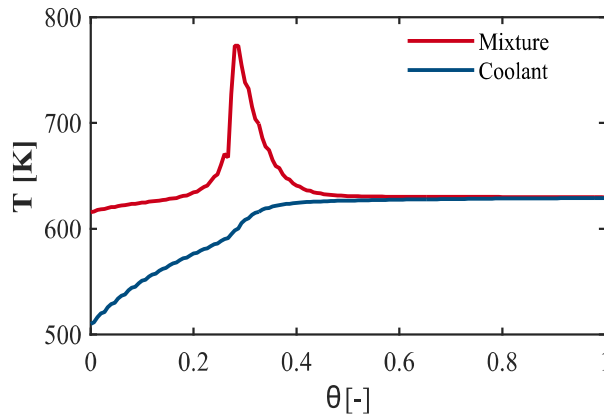


Figure 3.11 Temperature profile of a single polytropic reactor

3.4 Conclusion

A reaction configuration was optimized to produce renewable methane of natural gas grid quality while limiting the downstream processing of the produced gas to one drying step. Due to thermodynamic constraints, this was only possible when at least one of the products was extracted during the reaction. The impact of ideal cooling and dosing/removal of the different components on the STY was systematically investigated using a design procedure that is based on the EPF methodology. The results showed that extraction of both methane and water increases the STY significantly. Also, the removal of methane is more advantageous than the removal of water due to the fact that the adsorption equilibrium constant of methane, which contributes to the ‘resistance’ term in the rate equation, is larger than that of water by two orders of magnitude over the operating temperature range. Nevertheless, the extraction of methane is technically challenging. Therefore, two reaction configurations that apply water removal were investigated and compared: (1) a polytropic membrane reactor that allows continuous and in-situ water removal and (2) polytropic reactor cascade with intermediate condensation. The results showed that the cascade consisting of 3 condensation steps and 4 multitubular reactor was the most attractive configuration in terms of maximized STY. The cascade was optimized in terms of the temperature profile of the reaction mixture, inlet composition, operating pressure, reactor dimensions and the extent of condensation. The performance of 3CS configuration was then compared to the typical

reactor designs used for methanation, the cascade of adiabatic reactors with intercooling and the single polytropic reactor. It was demonstrated that our design achieved much higher STY and allowed better temperature control. Finally, it should be noted that while reactor-condenser cascade was superior to the membrane reactor, the membrane reactor can still be an attractive option for methanation due to its compactness. Increasing the permeance of the membrane reactor should be the focus of many researchers since it can significantly enhance its performance.

4 Total cost optimization of the Sabatier process

Since economics is the main driving force of chemical processes, and since optimal reactor design and operation based on stand-alone criteria like the STY doesn't necessarily lead to the economic optimum design, an optimization of the whole CO₂ methanation process, with main emphasis on the reaction section, is performed for minimum total cost (C_t). The same process layout proposed in the previous chapter is also considered here. The process is comprised of a reaction step and a drying step. The drying step is realized using a glycol unit. Based on the results of the previous chapter, the reactor configuration considered here is a cascade of multitubular reactor with intermediate condensation steps. A comparison is made between cascades incorporating one, two, and three condensation steps within the reaction section. The plant is assumed to operate for 20 years, 330 days a year, and a volumetric SNG rate of 891 m_N³/h. The reactors are rigorously modeled while the other process units are described using shortcut models. Models for estimating the costs of the different units are also implemented.

4.1 Modeling and sizing of equipment

4.1.1 Reactors

We consider a cascade of polytropic tube bundle reactors with interstage condensation. The reactors are assumed to be randomly packed with spherical pellets. Optimization variables for each reactor of the cascade are: inlet temperature ($573 \text{ K} \leq T_{in} \leq 673 \text{ K}$), inlet pressure ($1 \text{ atm} \leq p_{in} \leq 10 \text{ atm}$), tube diameter ($1 \text{ cm} \leq d_t \leq 5 \text{ cm}$), length of reactor

(0.3 m ≤ L ≤ 10 m), and inlet composition of the first reactor ($0.79 \leq x_{H_2,in} \leq 0.81$, $0.19 \leq x_{CO_2,in} \leq 0.21$). The particle diameter of the catalyst in the tubes is also a decision variable and can be varied such that $d_t/d_p \geq 10$. The number of tubes in each reactor, which is an integer number, is not an optimization variable here. This is because the solver used in the optimization is a Nonlinear Programming (NLP) solver and not a Mixed Integer Nonlinear Programming (MINLP) solver. Each reactor is therefore assumed to comprise of 500 tubes.

The tubular reactors are described using a 1D pseudo homogeneous plug flow model. The component mass balances, Eq. (4.1), and the energy balance, Eq.(4.2), are given by:

$$\frac{d(\rho_i v_i)}{dz} = \left(\rho_c \frac{1-\varepsilon}{\varepsilon} M_i \right) \sum_j v_{ij} r_j \quad (4.1)$$

$$\rho_g C_p \frac{dT}{dz} = - \left(\frac{4}{d_t \varepsilon} q_{ex} + \sum_j \Delta H_j r_j \rho_c \frac{(1-\varepsilon)}{\varepsilon} \right) \frac{1}{v_i} \quad (4.2)$$

The reaction rate expressions r_j for the main reaction (methanation) and the main side reaction (reverse water gas shift) are obtained from the work of Xu and Froment.⁵⁰

The heat transfer between the reactor and the coolant are described by

$$q = \alpha (T - T_c) \quad (4.3)$$

where T_c , bounded between 550 and 673 K, is used to control the heat flux q_{ex} . The heat transfer coefficient across the wall of the reactor is calculated using the correlation given in Chapter 3.

Ergun's equation is used to estimate the pressure drop:

$$\frac{dp}{dz} = - \left(150 \mu_g \frac{(1-\varepsilon)^2}{d_p^2 \varepsilon^3} + 1.75 \frac{v_s \rho_g (1-\varepsilon)}{d_p \varepsilon^3} \right) v_s \quad (4.4)$$

4.1.2 Heat exchangers

The heat exchangers considered are counter-current tube-shell exchangers. The heat exchange area is calculated in terms of the heat duty, the mean logarithmic temperature difference, and the heat transfer coefficient.

$$A = \frac{Q}{U \Delta T_{lm}} \quad (4.5)$$

$$\Delta T_{lm} = \frac{(T_{in} - T_{e,out}) - (T_{out} - T_{e,in})}{\ln\left(\frac{T_{in} - T_{e,out}}{T_{out} - T_{e,in}}\right)} \quad (4.6)$$

If no phase change takes place, then the heat duty is calculated using:

$$Q = \sum_i n_i \int_{T_{in}}^{T_{out}} \hat{C}_{p,i}(T) dT \quad (4.7)$$

In case of phase change, then the latent heat is taken into account as will be shown in later in the modeling of the condensers for example.

The overall heat transfer coefficients are dependent on the heat transfer media. Typical values⁶⁹ are used and shown in Table 4.1.

Table 4.1 Typical values of the heat transfer coefficients for various fluids

In Shell	In Tube	Heat transfer coefficient [W/(m ² K)]
Water	Water vapor condensing	1929
Steam	Gases	283
Organic solvent	Organic solvent	340
glycol	glycol	68
Glycol	Gas	255

4.1.3 Compressors

The outlet pressure of the compressor is a decision variable. The outlet temperature and theoretical power of the compressor are calculated by assuming theoretical isentropic compression and ideal gas behavior.

$$T_{CMP,out} = T_{CMP,in} \left(\frac{P_{CMP,out}}{P_{CMP,in}} \right)^{\frac{\gamma-1}{\gamma}} \quad (4.8)$$

$$P_{CMP,th} = \dot{n}_{CMP,in} \left(\frac{1.4}{1.4-1} \right) RT_{CMP,in} \left[\left(\frac{P_{CMP,out}}{P_{CMP,in}} \right)^{\frac{1.4-1}{1.4}} - 1 \right] \quad (4.9)$$

The resulting brake power is estimated with the help of compressor efficiency (assumed to be 0.9) and the motor efficiency (assumed to be 0.8).⁶²

$$P_{CMP,b} = \frac{P_{CMP,th}}{\eta_c \eta_m} \quad (4.10)$$

4.1.4 Condensers

While the pressure in the condenser is equal to the outlet pressure of the reactor preceding it, the outlet temperature of the condenser and overhead split factor of water are decision variables.

Every condenser can be modeled as three heat exchangers in series. The heat duty of the condenser is calculated by summing up the heat duties of the three heat exchangers:

$$Q^{cond} = Q_1 + Q_2 + Q_3 \quad (4.11)$$

The first heat exchanger decreases the temperature of the gas mixture, using steam as a cooling media, to the dew point at which Eq. (4.12) is satisfied.

$$\sum_i x_{i,l}^{cond} = 1 \quad (4.12)$$

Since only water vapor is condensed (the other gases are at temperatures above the critical temperature), the equation becomes:

$$x_{H_2O,l}^{cond} = 1 \quad (4.13)$$

By applying Raoult's and Dalton's laws, it follows:

$$x_{H_2O,l}^{cond} = \frac{P^{cond} x_{H_2O,v}^{cond}}{P_{H_2O}^{sat}} \quad (4.14)$$

Using Eq. (4.13) and Eq. (4.14), we end up with:

$$\frac{P^{cond} x_{H_2O,v}^{cond}}{P_{H_2O}^{sat}} = 1 \quad (4.15)$$

The saturated partial pressure of water is temperature dependent:

$$\log(p_{H_2O}^{sat}) = A + \frac{B}{T_{Dp}} + C \log(T_{Dp}) + DT_{Dp} + ET_{Dp}^2 \quad (4.16)$$

Thus, the dew point temperature can be obtained when Eq. (4.15) is satisfied.

The amount of sensible heat, Q_1 , that needs to be removed in order to decrease the temperature of the gas mixture to the dew point is calculated as follows:

$$Q_1 = \dot{n}_{mix,in}^{cond} \sum_i \int_{T_{in}^{cond}}^{T_{Dp}^{cond}} x_{i,in}^{cond} \hat{C}p_i dT \quad (4.17)$$

The phase transition from vapor to liquid and the sub-cooling to the desired temperature (T^{cond}) occurs in the second and third heat exchanger respectively, both of which utilizes cooling water.

The latent heat, Q_2 , is the amount of heat released due to the change in the water phase from vapor to liquid and is calculated as follows:

$$Q_2 = -\dot{n}_{H_2O,d} \hat{h}_{H_2O}^{vap} \quad (4.18)$$

$$\hat{h}_{H_2O}^{vap} = 52053 \left(1 - \frac{T^{DP}}{647.13} \right)^{0.321} \quad (4.19)$$

The sensible heat removed during subcooling is calculated using:

$$Q_3 = \dot{n}_{mix,out}^{cond} \sum_i \int_{T_{DP}^{cond}}^{T_{out}^{cond}} x_{i,out}^{cond} \hat{C}p_i dT \quad (4.20)$$

The distribution of the different components in the two phases is calculated in the same way as in Chapter 3.

4.1.5 Glycol dehydration unit

Since the NG quality specifications demand extremely low water content, it is necessary for the produced gas to undergo downstream drying which can be accomplished using various available technologies. The most commonly used one is water absorption by means of triethylene glycol (TEG). The TEG dehydration unit (Figure 4.1) is favored over other techniques due to its inexpensive installation, ease of operation, and the relatively low energy requirement for TEG regeneration.

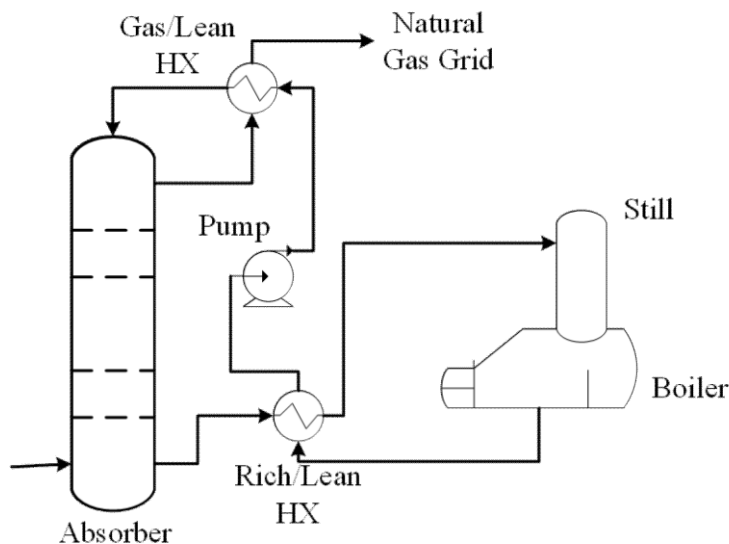


Figure 4.1 Glycol uni- an overview of the main components

The modeling and sizing of the main individual components of a typical glycol unit is presented below. The operating and design variables of the unit are optimized simultaneously with the reaction section.

4.1.5.1 Absorber

The produced SNG is first fed to the bottom of a bubble-cap tray absorber from the top of which enters lean TEG (glycol with little or no water). As the wet gas flows upward throughout the column, it is counter-currently contacted, on each tray, with the lean TEG. Having high affinity towards water, the TEG absorbs the water vapor and the gas is dehydrated to the required specification.

The pressure of the absorber column and the temperature at which the gas enters the column are decision variables. They are bounded as follows:

$$39 \leq p^{abs} \leq 83 \text{ atm}$$

$$294 \leq T_{in}^{abs} \leq 319 \text{ K}$$

The water removal efficiency of the absorption column is determined from a number of decision variables based on the empirical correlations developed by Bahadori and Vuthaluru.⁷⁰ These variables are the number of theoretical stages or trays in the column, the circulation rate, and the glycol purity.

The water removal efficiency is calculated using:

$$\ln(\eta^{abs}) = a^{abs} + \frac{b^{abs}}{\psi} + \frac{c^{abs}}{\psi^2} + \frac{d^{abs}}{\psi^3} \quad (4.21)$$

The circulation rate, defined as $\psi = \frac{\dot{V}_{TEG}}{\dot{m}_{H_2O,rem}}$, is a decision variable that varies between

0.01 and 0.06.

The coefficients a^{abs} , b^{abs} , c^{abs} , and d^{abs} are dependent on the TEG mass fraction (y_{TEG}) and also on the number of theoretical trays in the absorber via the set of values of the coefficients A^{abs} , B^{abs} , C^{abs} , and D^{abs} (see Table 4.2).

$$a^{abs} = A_1^{abs} + \frac{B_1^{abs}}{y_{TEG}} + \frac{C_1^{abs}}{y_{TEG}^2} + \frac{D_1^{abs}}{y_{TEG}^3} \quad (4.22)$$

$$b^{abs} = A_2^{abs} + \frac{B_2^{abs}}{y_{TEG}} + \frac{C_2^{abs}}{y_{TEG}^2} + \frac{D_2^{abs}}{y_{TEG}^3} \quad (4.23)$$

$$c^{abs} = A_3^{abs} + \frac{B_3^{abs}}{y_{TEG}} + \frac{C_3^{abs}}{y_{TEG}^2} + \frac{D_3^{abs}}{y_{TEG}^3} \quad (4.24)$$

$$d^{abs} = A_4^{abs} + \frac{B_4^{abs}}{y_{TEG}} + \frac{C_4^{abs}}{y_{TEG}^2} + \frac{D_4^{abs}}{y_{TEG}^3} \quad (4.25)$$

An empirical correlation is introduced by Bahadori et al. to calculate the purity of the lean TEG (y_{TEG}).⁷¹ It is a function of the boiler pressure and boiling temperature (Eq. (4.26)).

$$\ln(y_{TEG}) = a^{reb} + \frac{b^{reb}}{T} + \frac{c^{reb}}{T^2} + \frac{d^{reb}}{T^3} \quad \text{where} \quad (4.26)$$

$$a^{reb} = A_1^{reb} + B_1^{reb} p + C_1^{reb} p^2 + D_1^{reb} p^3$$

$$b^{reb} = A_2^{reb} + B_2^{reb} p + C_2^{reb} p^2 + D_2^{reb} p^3$$

$$c^{reb} = A_3^{reb} + B_3^{reb} p + C_3^{reb} p^2 + D_3^{reb} p^3$$

$$d^{reb} = A_4^{reb} + B_4^{reb} p + C_4^{reb} p^2 + D_4^{reb} p^3$$

The coefficients needed to calculate the TEG purity are presented in Table 4.3.

Table 4.2 Coefficients of the Correlation used for calculating the TEG

Index	A ^{abs}	B ^{abs}	C ^{abs}	D ^{abs}
1	-1.27×10 ⁵	3.78×10 ⁵	-3.78×10 ⁵	×1.2410 ⁵
2	1.16×10 ⁴	-3.46×10 ⁴	3.43×10 ⁴	-1.13×10 ⁴
3	-3.34×10 ²	9.94×10 ²	-9.86×10 ²	3.2×10 ²
4	2.85	-8.5	8.43	-2.79×10

Table 4.3 Coefficients of the correlation used in calculating the TEG purity

Index	A ^{reb}	B ^{reb}	C ^{reb}	D ^{reb}
1	-1.077391×10	6.846823×10 ⁻¹	-1.033838×10 ⁻²	4.777461×10 ⁻⁵
2	1.432249×10 ⁴	-9.191847×10 ²	1.385308×10	-6.426421×10 ⁻²
3	-6.323204×10 ⁶	4.107286×10 ⁵	-6.176238×10 ³	2.877455×10
4	9.271070×10 ⁸	-6.110140×10 ⁷	9.161653×10 ⁵	-4.288629×10 ³

The actual number of trays is calculated by assuming a tray efficiency of 25 % since equilibrium on a tray is usually a very poor assumption.⁶²

$$N_{real} = \frac{N_{th}}{\eta_{tray}} \quad (4.27)$$

In order to calculate the tray stack height, a typical tray spacing of 0.6 m is assumed (Eq. (4.28)).

$$H_{tray} = 0.6(N_{real} - 1) \quad (4.28)$$

The total height of the absorber column is equal to the height of the tray stack plus an additional eight feet to allow space for a vapor disengagement area above the top tray and an inlet gas area at the bottom of the column.

The diameter of the absorber column (Bubble Cap Column) is calculated with the help of the bubble cap column $C_b=176$ using Eq. (4.29-4.31) as reported by Bahadori and Vuthaluru.⁷⁰

$$D_b = \sqrt{\frac{4\dot{m}_{mix}}{j_{TEG}\pi}} \quad (4.29)$$

where \dot{m}_{mix} is the mass flow rate of the gas mixture and j_{TEG} is the mass flux [Kg/(hr m²)].

$$\dot{m}_{mix} = \sum_{i=1}^5 \dot{n}_i M_i \quad (4.30)$$

$$j_{TEG} = C_b \sqrt{\rho_{mix} (\rho_{TEG} - \rho_{mix})} \quad (4.31)$$

The density of the TEG is calculated using the temperature dependent correlation.⁷²

$$\rho_{TEG} = 1139.48 - 0.7104(T_{TEG,in} - 273.13) - 4.3663 \times 10^{-4} (T_{TEG,in} - 273.13)^2 \quad (4.32)$$

$$\rho_{mix} = \frac{pM_{mix}}{RT} \quad (4.33)$$

$$M_{mix} = \sum_{i=1}^5 x_i M_i \quad (4.34)$$

4.1.5.2 Reconcentrator

The water-rich glycol, exiting the absorber, enters a still column mounted on top of a reboiler where it is regenerated by simple distillation. As it flows downward through the still and into the reboiler, the rich glycol is heated to an optimal regeneration

temperature ($405 \leq T^{reb} \leq 477$ K) at an optimal pressure ($0.4 \leq p^{reb} \leq 1.4$ atm). Under these conditions, the water is vaporized and is driven out through the top of the still column. The lean glycol can then be circulated again through the absorber to repeat the process of continuously drying the SNG. The relatively easy separation of TEG and water is owed to the wide difference in their boiling points. The heat duty of the reboiler is assumed to comprise of only the sensible heat and the heat of water vaporization. It can be calculated using the formulas provided by the Glycol Dehydrator Design Manual of Sivalls,⁷³ the heat duty of the reboiler can be calculated as follows:

$$Q_t^{reb} = Q_{sens}^{reb} + Q_{vap,H_2O}^{reb} \quad (4.35)$$

$$Q_{sens}^{reb} = \dot{V}_{TEG} \rho_{TEG} C_{p,TEG} (T_{TEG,out}^{reb} - T_{TEG,in}^{reb}) \quad (4.36)$$

$$Q_{vap,H_2O}^{reb} = 970.3(\dot{m}_{H_2O,rem}^{abs}) \quad (4.37)$$

4.1.5.3 Rich Glycol/Lean Glycol Heat Exchanger

This heat exchanger is designed to increase the temperature of the rich glycol before it is fed into the still column, thus reducing significantly the heat duty of the reboiler. The temperature can be generally increased to around 150°C by recovering heat from the lean glycol exiting the reboiler. As a result, the lean glycol is also cooled down to the desired temperature (below 121 °C) before it is pumped back into the absorber.⁷⁴

4.1.5.4 Pump

Due to the pressure difference between the boiler and the absorber, a centrifugal pump is needed to circulate the low-pressure lean glycol back to the high-pressure absorber. pump efficiency of 0.5 and Motor efficiency of (0.9) are used.⁶²

$$P_{PMP,b} = \frac{\dot{V}_{TEGlean} (p_{out}^{PMP} - p_{in}^{PMP})}{\eta_p \eta_m} \quad (4.38)$$

$$\dot{V}_{TEGlean} = \frac{m_{t,TEGlean}}{\rho_{TEGlean}} \quad (4.39)$$

$$\rho_{TEGlean} = \rho_{H_2O,st} SG_{TEGlean} \quad (4.40)$$

The specific gravity $SG_{TEGlean}$ is calculated using (obtained from Dow Chemicals):

$$SG_{TEGlean} = 0.992 + 1.7518 \times 10^{-1} y_{TEGlean} - 5.4955 \times 10^{-2} y_{TEGlean}^2 \quad (4.41)$$

4.1.5.5 Gas/Glycol Heat Exchanger

The Gas/glycol heat exchanger is designed to adjust the temperature of the lean glycol prior to entering the absorber. After the dried synthetic natural gas exits the top of the absorber, it passes through the heat exchanger where it exchanges heat with the recirculated lean glycol. For a proper design, the lean glycol temperature needs to be 5-15 °F ($\approx 3-10^\circ\text{C}$) higher than the temperature at which the wet SNG enters the absorber.⁷⁵

4.2 Costing

The total cost of the CO₂ methanation process comprises of the capital cost, the utility costs (steam, water, electricity), and the costs of the raw materials (H₂, CO₂).

$$C_t = C_{raw} + C_{utility} + C_{inv} \quad (4.42)$$

4.2.1 Capital cost

The capital cost is the fixed investment needed to purchase and install the various major units of the CO₂ methanation process (e.g. reactors, heat exchangers, pump, compressors, glycol absorber, reboiler).

After sizing the different major units of the CO₂ methanation process, their costs are estimated using power law correlations developed by Guthrie. The proposed method is comprised of factors that are used to account for the numerous direct and indirect costs associated with the cost of the equipment.⁶²

$$BMC = UF(MPF + MF - 1)BC \quad (4.43)$$

The Base Cost (BC) is the ‘free on board’ equipment cost. It increases nonlinearly with the capacity of the unit (S) according to equation:

$$BC = BC_0 \left(\frac{S_1}{S_{1,0}} \right)^\chi \left(\frac{S_2}{S_{2,0}} \right)^\phi \quad (4.44)$$

The standard Base Costs (BC₀) of various units with their respective capacities (S₀) and exponents (χ and ϕ) are presented in Table 4.4. As can be seen from this table, each unit has its own characteristic variable that defines its capacity. For instance, the capacity of a shell-and-tube heat exchanger is associated with the heat exchange area while that of the reactor is defined by the reactor length (S₁) and diameter (S₂).

The module factor (MF) accounts for the installation of the equipment (piping and labor) as well as for the shipping, taxes, and supervision. It is dependent on the Base Costs as shown in Table 4.4. The material and pressure correction factor MPF is used when the process unit is made of special materials or is operated at high pressure.

Table 4.4 Cost parameters of the different units

Unit	BC ₀	S ₁	χ	S ₂	ϕ	MPF	MF	CE	UF
CMP	23×10 ³	74.6×10 ³	0.77	1	0	2.8	1	115	5.0835
HEX	3×10 ²	0.510967	0.024	1	0	0.85	1.83	115	5.0835
Abs	1×10 ³	1.2192	0.81	0.9144	1.05	1.6	4.23	115	5.0835
Abs Stack	180	3.048	0.97	0.6096	1.45	2.8	1	115	5.0835
Still	1×10 ³	1.2192	0.81	0.9144	1.05	1	4.23	115	5.0835
Reb	1×10 ³	0.510967	0.024	1	0	0.85	1.83	115	5.0835
RCTR	6.9×10 ²	1.2192	0.78	0.9144	0.98	1.15	3.18	115	5.0835
PMP	3.9×10 ²	0.43499	0.17	1	0	2.895	3.38	402	1.4542

Since the cost data for the various types of equipment are given in terms of mid 1968 prices, an updated factor to account for inflation is introduced:

$$UF = \frac{\text{present cost index}}{\text{base cost index}} \quad (4.45)$$

In our work, the Chemical Engineering Plant Index of the year 2012 published by the Chemical Engineering magazine (CI=584.6) is used for cost updating. The base cost index is of year 1969 (IC=115) except for the circulation pump.

The capital investment cost is the summation of the costs of all units in addition to the cost of the catalyst used:

$$C_{cap} = \sum_u BMC_u + \Psi_{catal} \rho_{catal} V_{rctr} (1 - \varepsilon) N_{rctr} \quad (4.46)$$

4.2.2 Raw materials and utility cost

The utilities of the CO₂ methanation process include steam and water for heating/cooling in addition to electricity for compression/pumping. The utility demands are determined from the material and energy balances. The cost of the utilities are presented in Table 4.5.

$$C_{raw} = \sum_i \Psi_i \dot{n}_{i,in} \quad i \in \{H_2, CO_2\} \quad (4.47)$$

$$C_{el} = \sum_s \Psi_{el} P_s \quad s \in PMP \vee CMP \quad (4.48)$$

$$C_{st} = \Psi_{st} Q_{st} \quad (4.49)$$

$$C_{CW} = \Psi_{CW} Q_{CW} \quad (4.50)$$

The specific prices are summarized in Table 4.5.

Table 4.5 Prices of raw materials and utilities

Utility/Raw Materials	Price	Unit
Steam	1.4×10^{-8}	\$/J
Cooling water	2.54×10^{-9}	\$/J
Electricity	5.33×10^{-8}	\$/J
Hydrogen	1.2×10^{-2}	\$/mol
Carbon dioxide	1.1×10^{-3}	\$/mol
Catalyst	500	\$/kg

The resulting optimization problem was solved using CONOPT 3.14 G in AMPL. It can be stated as follows:

$$\min_{DoF} Cost$$

s.t:

- Component balance equations
- Energy balance equation
- Pressure drop equation
- Chemical reaction kinetics
- Heat transport kinetics
- Ideal gas law
- Inequality constraints
- Shortcut models for other process units (e.g. condensers, compressors, absorber)

4.3 Results and discussion

Eventhough increasing the number of condensation steps enhances the performance of the reactor cascade as was demonstrated in the previous chapter, it may not always have a positive effect on the economics of the process. The results in Figure 4.2 shows that having two intermediate condensation steps instead of three steps reduces the relative production cost of the SNG by 1.36%. For the given plant capacity, this means a cost reduction of 1.8 million USD over a period of 20 years. However, a further decrease in

the number of condensation steps to only one, leads to an increase in the cost by around one million USD. Thus, the best reactor configuration is a cascade of three multitubular reactors with two intermediate condensation steps (Figure 4.3).

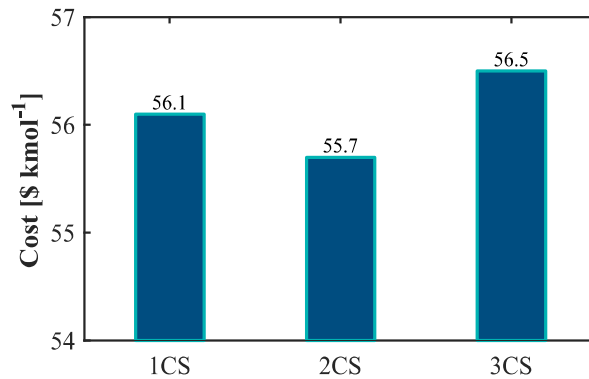


Figure 4.2 Relative production cost for the three cascades

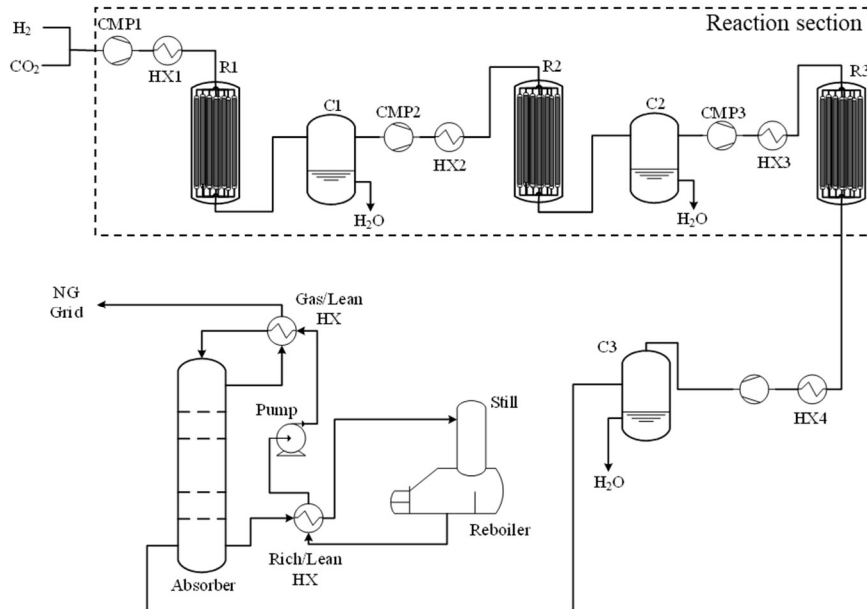


Figure 4.3 Process layout of the cost optimal process

The optimal temperature profiles of the coolant and reaction mixture in the three reactors are presented in Figure 4.4 (left). Initially, the mixture temperature of Reactor 1 is at the lower bound (573 K) and then starts to increase gradually until $\theta=0.87$. Afterwards, the temperature remains constant at the upper bound (673 K) since high temperatures enhance the reaction. On the other hand, the temperature difference between the gas mixture and the coolant is zero at the beginning indicating that no active cooling is needed. This reduces the cost of cooling. The temperature difference instantly becomes 30 K at $\theta=0.08$ to allow maximum heat transfer and then remains constant till $\theta=0.9$. After that, this difference keeps getting smaller towards the reactor

outlet in order to maintain the mixture temperature at 673 K. A higher inlet temperature is observed for Reactor 2.

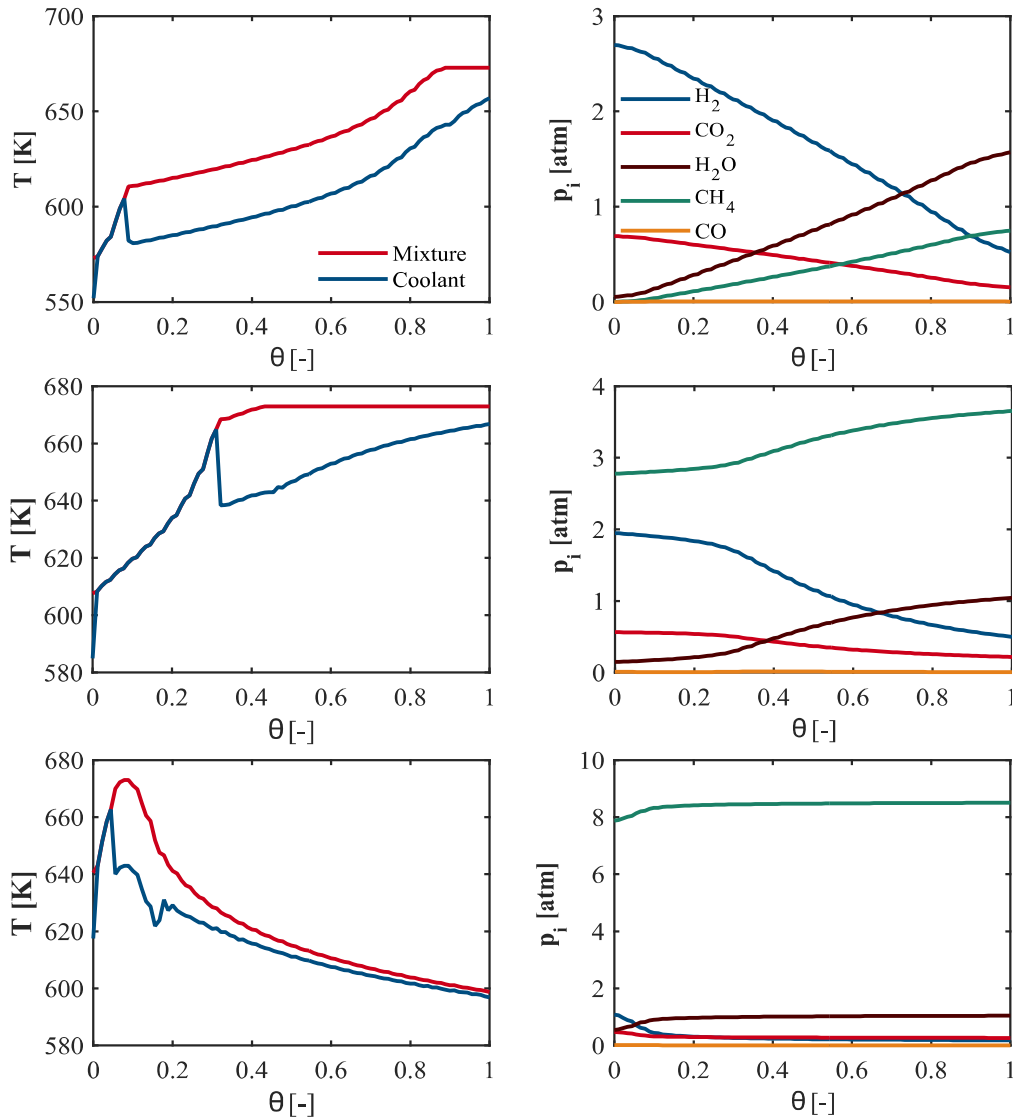


Figure 4.4: Optimal temperature profiles (left column), partial pressures (right column) in the tubes of the three reactors (from top to bottom: Reactors 1, 2, and 3).

The mixture temperature increases from 608 K at $\theta=0$ to 668 K without the need for external cooling. After $\theta=0.31$, cooling is applied and the mixture temperature continues to increase and then gets fixed at 673 K while the coolant temperature increased from 638 K to 667 K. As for the mixture temperature in Reactor 3, it increases from 643 K at the reactor inlet to 673 K at $\theta=0.08$ before it starts to gradually decrease, with the decrease in the coolant temperature, reaching 599 K at the reactor outlet. Based on the above, the optimal temperature profiles can be approximated using a combination of adiabatic operation as well as active cooling using co-current (Reactor 1 and 2) and counter current (Reactor 3) heat exchange.

Figure 4.3 (right) also shows the partial pressure of the different components along the three reactors. Notably, the optimal total inlet pressure of Reactor 1 and Reactor 2 are 3.44 and 5.45 atm respectively. Generally, a higher pressure is favorable from the kinetic and the thermodynamic perspective. However, a relatively low pressure is preferred in the first two reactors since it leads to less amount of heat released by the reaction and thus allows a better temperature control especially when operating the reactor adiabatically. More importantly, a step-wise increase in the inlet pressure starting from 3.44 to 5.45 and then 10 atm reduces the operating cost of the compressors since the molar rate of the gas mixture to be compressed decreases as we go from Reactor 1 to Reactor 3 due to both the reaction and the condensation. Furthermore, having the inlet pressure of the last reactor (Reactor 3) at the upper bound (10 atm) shifts the chemical equilibrium further towards the product side, thereby achieving the desired high level of H₂ conversion ($X > 99\%$), and also increases the reaction rate. Furthermore, a high pressure in the last reactor reduces the power needed for compressing the gas to 39 atm, which is the optimal pressure level in the absorber column of the glycol unit. The geometric dimensions of the reactors are shown in Table 4.6.

Table 4.6 The geometric design and operating conditions of the different reactors, each consisting of 500 tubes, in the cost optimal 2CS cascade

Reactor	R1	R2	R3
D_t [cm]	1.9	1.8	5
D_p [mm]	1.9	1.8	1
L [m]	1.39	0.59	0.49
T_{in} [K]	573	608	640
T_{out} [K]	673	673	599
$x_{i,in}$ [-]	[0.78,0.20,0, 0.02,0]	[0.36,0.1,0.51,0.03,0]	[0.11,0.05,0.79,0.055,0]
{H ₂ ,CO ₂ ,CH ₄ ,H ₂ O,CO}			
$x_{i,out}$ [-]	[0.18,0.05,0.25,0.52,0]	[0.09,0.04,0.67,0.19,0]	[0.018,0.027,0.85,0.10,0]
{H ₂ ,CO ₂ ,CH ₄ ,H ₂ O,CO}			
X_{out} [-]	0.85	0.966	0.995
$\dot{n}_{t,in}$ [mol/s]	0.04	0.013	0.01

The results also show that the mole fraction of the reactants increase following each intermediate condensation which contributes to the sudden increase of reaction rates in the next reactor.

The mole fraction of CH₄ at the outlet of Reactor 3 is 85.1%. This increases further after drying the produced gas in the glycol unit such that the SNG quality requirements are met ($x_{i,out} = [0.02, 0.03, 0.95, 0, 0]$).

The produced gas enters the absorber at 313 while the lean TEG is fed from the top at 317 K at a circulation rate of $\psi = 0.52 \text{ m}^3$ of TEG / kg of water. Only two theoretical stages, which are equivalent to eight real stages, are needed to dry the produced SNG to the desired level. The diameter of the absorber is 1.43 m. The boiler is operated at 0.4 atm and 477 K leading to a TEG purity of 0.998. Other relevant operating conditions of the different process units are presented in Tables 4.7, 4.8, and 4.9.

Table 4.7 Optimal operating conditions of the compressors

Unit	Inlet	Outlet	Inlet	Outlet
	pressure [atm]	pressure [atm]	Temperature [K]	Temperature [K]
CMP1	1	3.44	333	474
CMP2	3	5.45	315	374
CMP3	5.42	10	342	408
CMP4	9.97	39	373	550

Table 4.8 Optimal operating conditions of the heat exchangers

Unit	Inlet Temperature [K]	Outlet Temperature [K]
HX1	474	573
HX2	374	608
HX3	408	640
HX4	599	373

Table 4.9 Optimal operating conditions of the condensers

Unit	Inlet	Outlet	ζ [-]
	Temperature [K]	Temperature [K]	{H ₂ ,CO ₂ ,H ₂ O,CH ₄ ,CO}
CND1	673	315	[1,1,0.025,1,1]
CND2	673	342	[1,1,0.24,1,1]
CND3	550	312	[1,1,0.015,1,1]

4.4 Conclusion

In this work, we designed a process for the production of SNG from H₂ and CO₂ and optimized it for minimized production cost. The proposed process is comprised of a reaction section and a drying section. The reaction section is a cascade of multitubular fixed bed reactors and intermediate condensation steps for water removal, and the drying section is a glycol unit. Rigorous models are used to describe the performance of the reactors while the other process units are modeled using shortcut models. The investment costs of the different units are computed using Guthrie's power law correlations. Different reaction cascades comprising of one, two, and three condensation steps are investigated. The simultaneous optimization of the reactors and other major units of the process (e.g. absorber, heat exchangers, compressors, condensers) in each cascade reveals that the most cost-efficient configuration is a cascade of three reactors and two intermediate condensers. The respective production cost of SNG is 55.7 \$/kmol can only be achieved by the optimal design and sizing of the reactors and sizing of the auxiliary units as well as operating the various process units at their optimal conditions. Within the reactor tubes for instance, optimal temperature profiles should be realized by applying a combination of active cooling (co-current and countercurrent) and adiabatic operation. The results also clearly demonstrate the importance of considering the coupling between the reaction section and the other process units when determining the optimal process operating conditions. It is shown, for example, that the optimal pressure of the first and second reactor is highly influenced by the compression cost. Instead of operating at the highest possible pressure, which is favourable from a kinetic and thermodynamic perspective, a low pressure is preferred (3.44 atm and 5.45 atm respectively). The results also show that taking the economics of the process into consideration when selecting the optimal reactor design and the operating conditions is

of paramount importance. High productivity does not necessarily mean more profit. While a cascade of three condensation steps within the reactor is the optimal configuration for maximum STY, a cascade of two condensation steps is the cost optimal setup. Furthermore, the production cost of the SNG can be significantly reduced by implementing efficient heat integration through the design of a smart heat exchanger network.

5 On the kinetics of the Sabatier reaction

5.1 Introduction

The design, optimization, and simulation of industrial processes demand a priori knowledge of the intrinsic rate and the selectivity of the reaction in question. Over the past few decades, a considerable amount of literature has been published on the kinetics of CO₂ methanation reaction.^{26,50,76–92} Nevertheless, most of these studies were carried out either under operating conditions not suitable for the industrial production of SNG (low pressure/low Temperature)^{26,77,79,81–86} or using catalysts that are very expensive (Ru, Rh) to be adopted in the industry.^{87–91} Moreover, only a limited number of the industrially relevant studies resulted in rate expressions that are thermodynamically consistent.^{50,92} The most frequently used kinetic model in the simulation and optimization of CO₂ methanation was proposed by Xu and Froment in 1989.⁵⁰ The model comprised of rate equations for methane steam reforming, CO₂ methanation, and reverse water gas shift on a standard methane steam reforming catalyst (Ni/MgAl₂O₄). The experiments related to CO₂ methanation and reverse water gas shift were conducted over technically relevant temperature and pressure ranges (573–673 K, 3–10 atm). However, the authors primarily focused in their study on methane steam reforming as reflected by the choice of the catalyst used.

As recent as the year 2016, several studies were published on the kinetics of CO₂ methanation. Since this reaction is a linear combination of RWGS and CO methanation, Ronsch et al.⁹³ adapted CO methanation and WGS rate equations proposed by Zhang et al.⁹⁴ to simulate the dynamic behavior of CO₂ methanation reactor. In his study, Zhang performed experiments over commercial nickel catalyst in a temperature range from 275 to 360 °C and with a total pressure range of 1–5 bar.

Hubble et al. and Lim et al. studied the kinetics of CO₂ methanation over Ni/Al₂O₃ using a batch reactor operated at 20 bar but at relatively low temperature (below 500 K).^{80,85} Koschany et al. carried out a kinetic study dedicated to CO₂ methanation under technically relevant conditions.⁹² The NiAl(O)_x catalyst employed in this study was highly selective to methane that only traces of CO were detected. Therefore, the r-WGS reaction was neglected and the derived kinetic model accounted only for the rate formation of methane.

In this work, we present a new comprehensive mechanistic kinetic study for CO₂ methanation performed on a commercial nickel based catalyst (Ni/CaO-Al₂O₃) over a wide range of process relevant conditions (temperature, pressure, and feed content). In contrast to the work of Koschany et al., the proposed model takes the r-WGS reaction into account. It is suggested that CO₂ methanation proceeds first via r-WGS reaction producing CO_{ad} which is further reduced to CH₄ in CO methanation reaction. The model is comprised of r-WGS and CO methanation rate expressions derived in accordance with mechanistic experimental and theoretical studies reported in literature^{15,92,95,96}.

5.2 Experimental

5.2.1 Experimental setup

The kinetic measurements were performed in an experimental setup operated under steady state. An overview of the experimental rig used in this work is shown in Figure 5.1.

Gas boosters purchased from MAXIMATOR[®] were employed in order to feed the reactor with gases (H₂ (purity:5.0), N₂ (purity:3.0), and CO₂ (purity:3.0)) at technically relevant operating pressures. The total pressure could be varied between 1 and 30 atm and was regulated by means of a back pressure control valve installed downstream the reactor. The flow rates of the gas streams were controlled using mass flow controllers (MFCs) manufactured and calibrated by BRONKHORST[®].

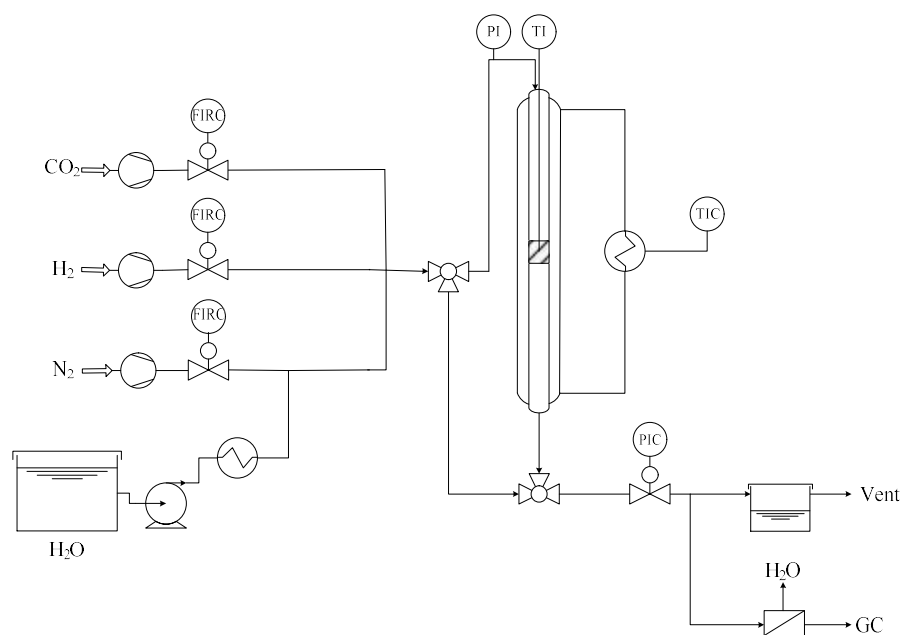


Figure 5.1 A schematic representation of the experimental setup used in the kinetic study

Steam was generated by pumping deionized water into the boiler using HPLC pump.

The feed lines were heated to prevent steam condensation upstream of the reactor.

The reactor was made of steel, had an I.D = 8 mm and was heated using an electric oven. A 0.5 mm thermocouple was inserted in the middle of the reactor in order to

measure the temperature of the catalyst bed. The catalyst used was a Ni/CaO.Al₂O₃ (20-25% NiO and 5-10% CaO) purchased from C&CS[®] in the form of spherical pellets. The pellets were crushed to a smaller size range at which mass and heat transfer limitations became negligible ($106 \leq D_p \leq 150 \mu\text{m}$). The ratio of the reactor inner diameter to the catalyst particle diameter is between 53 and 75.5 ($53 \leq \text{I.D./}D_p \leq 75.5$). This large ratio makes the assumption of plug flow adequate. The catalyst bed was diluted using inert particles (SiC) of the same size as the catalyst particles. This aimed at enhancing isothermality as well as obtaining sufficient bed length that decreased the deviation from plug flow performance.

The produced gas mixture was split into two streams. The majority of the gas was sent to the ventilation after passing through a water trap. A small portion was fed, after being dried using a membrane filter, to the Gas Chromatography (GC) for analysis. The GC used Helium as the carrier gas and Thermal Conductivity Detector (TCD) to determine the product composition (excluding water).

5.2.2 Preliminary and kinetic measurements

Initially, blank experiments without catalyst were conducted at relevant operating conditions. It was confirmed that neither the reactor nor SiC had any catalytic activity. And prior to the formal kinetic experiments, the catalyst stability and selectivity were also investigated under different pressures, temperatures and inlet composition. The catalyst showed good stability and high selectivity towards methane. Apart from the reactants, only CH₄, H₂O, and CO were detected at the reactor outlet.

For the kinetic experiments, the reactor was loaded with 76 mg of Ni/CaO-Al₂O₃ catalyst ($106 \leq D_p \leq 150 \mu\text{m}$). The catalyst was reduced by heating it up to 644 K at 2 K/min in a H₂/N₂ mixture (50:50) for 10 hours. After reduction, the catalyst underwent aging process for 24 hrs at 3 atm and 608.13 K. Following this, a series of experiments were performed using the aged catalyst during which the operating conditions (p, T, space velocity, and $x_{i,\text{in}}$) were systematically varied. To detect any possible deactivation

of the catalyst, a reference point measurement was conducted before and after every set of kinetic measurements. In case of deactivation, the aged catalyst is replaced by a fresh one which underwent the same reduction and aging procedure mentioned earlier. In this way, it was made certain that the kinetic data was collected at the same catalytic activity. Throughout the measurements, the reactor was operated in differential mode ($X \leq 0.1$) to ensure almost constant temperature and concentration along the catalyst bed.

Since the reactor was operated in the differential mode, the reaction rates were calculated using the following equations:

$$\hat{r}_{r-WGS} = \frac{X_{r-WGS} \dot{n}_{CO_2,0}}{m_c} \quad (5.1)$$

$$\hat{r}_{COMeth} = \frac{X_{COMeth} \dot{n}_{CO_2,0}}{m_c} \quad (5.2)$$

Knowing that

$$X_{r-WGS} = \frac{x_{CH_4,GC} + x_{CO,GC}}{x_{CH_4,GC} + x_{CO_2,GC} + x_{CO,GC}} \quad (5.3)$$

$$X_{COMeth} = \frac{x_{CH_4,GC}}{x_{CH_4,GC} + x_{CO_2,GC} + x_{CO,GC}} \quad (5.4)$$

It is worth noting that the insignificance of transport limitations was verified by performing different experimental tests. The mass of the catalyst (m_c) and CO₂ flow rate \dot{n}_{CO_2} were varied while keeping the space time (m_c/\dot{n}_{CO_2}) constant to test for external mass transfer (between the fluid and the external surface of the particle) limitation. In addition to varying particle size while keeping the same operating conditions to test for diffusion limitations.

5.3 Theoretical

Generally, two main reaction pathways are proposed for CO₂ methanation: ‘direct’ and ‘consecutive’. In the direct reaction route, CO₂ is hydrogenated into a CO_yH_x complex which is then reduced to CH₄ without the formation of CO. In contrast, the consecutive

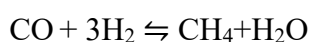
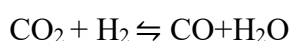
pathway proceeds first through the formation of intermediate CO in a reverse water gas shift reaction (r-WGS). The CO is then reduced to CH₄ via CO methanation route.

5.3.1 Consecutive route versus Direct route

In view of all that has been reported in literature on CO₂ methanation, it seems that the occurrence of either mechanisms (Direct or Consecutive) is highly dependent on the catalyst used. As was mentioned in the first chapter regarding the mechanisms, the ‘direct’ reaction pathway for CO₂ methanation was suggested in only few experimental studies^{17–20} where zirconia and/or ceria oxides were used as catalyst support. The formation of CH₄ independent of CO intermediate was attributed to the activation of CO₂ by the weak basic sites of the zirconia-ceria support (Aldana). On the other hand, a larger number of studies (experimental and theoretical) considered CO an indispensable intermediate in the CO₂ methanation reaction.^{24,25} For example, in a more recent study, Garbarino et al. studied CO₂ methanation over various Ni/alumina catalysts. It was concluded that fast methanation occurs at the expense of CO intermediate on the corners of nanoparticles interacting with alumina likely with a ‘via oxygenate’ mechanism.

It should also be mentioned that the concentrations of CO and CH₄ observed during the preliminary experiments that were carried out in our study were of the same order of magnitude. Furthermore, as will be shown in the Results section, the CH₄ selectivity was highly dependent on SV indicating that a series reaction is taking place.

Based on all the above, it is assumed in this work that CH₄ formation proceeds via r-WGS reaction followed by CO methanation according to the equations below:



Moreover, the side reactions such as the boudouard reaction, which may take place in parallel with the aforementioned reactions, were not considered in this work.

5.3.2 Mechanistic derivation of plausible kinetic models

Three main mechanisms were proposed in literature for the formation of CO during r-WGS reaction^{15,16}. One mechanism, the Redox mechanism, involves the dissociation of CO₂, upon adsorbing on the active sites of the catalyst, into CO_{ad} and O_{ad} as shown in Table 5.1. The other two mechanisms are ‘Hydrogen Assisted’ mechanisms during which adsorbed hydrogen reacts with adsorbed CO₂ to form an oxygenate intermediate (HCOO or COOH) that is converted, in a second step, into CO. According to Bothra et al., however, the formate intermediate (HCOO) is highly stable on the surface of nickel and is considered a spectator compound.¹⁶ Therefore, HCOO-mediated mechanism was discarded. Only the redox mechanism and the COOH mediated mechanism are considered to be plausible mechanisms for the reverse water gas shift reaction.

Table 5.1 Mechanisms for the activation of CO₂ over Nickel

Redox mechanism	Hydrogen-assisted mechanism (COOH-mediated)	Hydrogen-assisted mechanism (HCOO-mediated)
$H_2 + 2S \rightleftharpoons 2 H-S$	$H_2 + 2S \rightleftharpoons 2 H-S$	$H_2 + 2S \rightleftharpoons 2H-S$
$CO_2 + 2S \rightleftharpoons CO_2-2S$	$CO_2 + H-S \rightleftharpoons COOH-S + S$	$CO_2 + 2S \rightleftharpoons CO_2-2S$
$CO_2-2S \rightleftharpoons CO-S + O-S$	$COOH-S + S \rightleftharpoons CO-S + HO-S$	$CO_2-2S + H-S \rightleftharpoons HCOO-2S + S$
$CO-S \rightleftharpoons CO + S$	$CO-S \rightleftharpoons CO + S$	$HCOO-2S \rightleftharpoons OH-S + CO-S$
$O-S + H-S \rightleftharpoons OH-S + S$	$O-S + H-S \rightleftharpoons OH-S + S$	$CO-S \rightleftharpoons CO + S$
$OH-S + H-S \rightleftharpoons H_2O-S$	$OH-S + H-S \rightleftharpoons H_2O-S$	$OH-S + H-S \rightleftharpoons H_2O-S$
$H_2O-S \rightleftharpoons H_2O + S$	$H_2O-S \rightleftharpoons H_2O + S$	$H_2O-S \rightleftharpoons H_2O + S$

As for CO methanation, two mechanisms are considered.²⁷ The first is the CO dissociation mechanism where CO_{ad} dissociates into C_{ad} and O_{ad}. The second is the hydrogen assisted (HCO-mediated) mechanism where adsorbed hydrogen reacts with CO_{ad} to form HCO_{ad} (see Table 5.2).

The whole reaction system can then be described by combining any of the r-WGS mechanism with one of the CO methanation mechanisms (four different overall

mechanisms). Accordingly, several Langmuir-Hinshelwood-Hougen-Watson kinetic models for r-WGS and CO methanation were derived after assuming certain steps to be rate determining, others in quasi-equilibrium, and some surface species as Most Abundant Surface Intermediates (MASI). For an adequate and a more comprehensive derivation of the models, the assumptions made with respect to the rate determining steps were mostly based on the experimental and theoretical studies reported in literature.

Table 5.2 Two reaction mechanisms for CO methanation

CO dissociation mechanism	Hydrogen-assisted mechanism (HCO-mediated)
$\text{CO-S} + \text{S} \rightleftharpoons \text{C-S} + \text{O-S}$	$\text{CO-S} + \text{H-S} \rightleftharpoons \text{HCO-S} + \text{S}$
$\text{C-S} + \text{H-S} \rightleftharpoons \text{CH-S} + \text{S}$	$\text{HCO-S} + \text{S} \rightleftharpoons \text{CH-S} + \text{O-S}$
$\text{CH-S} + \text{H-S} \rightleftharpoons \text{CH}_2\text{-S} + \text{S}$	$\text{CH-S} + \text{H-S} \rightleftharpoons \text{CH}_2\text{-S} + \text{S}$
$\text{CH}_2\text{-S} + 2\text{H-S} \rightleftharpoons \text{CH}_4\text{-S} + 2\text{S}$	$\text{CH}_2\text{-S} + 2\text{H-S} \rightleftharpoons \text{CH}_4\text{-S} + 2\text{S}$
$\text{CH}_4\text{-S} \rightleftharpoons \text{CH}_4 + \text{S}$	$\text{CH}_4\text{-S} \rightleftharpoons \text{CH}_4 + \text{S}$
$\text{O-S} + \text{H-S} \rightleftharpoons \text{OH-S} + \text{S}$	$\text{O-S} + \text{H-S} \rightleftharpoons \text{OH-S} + \text{S}$
$\text{OH-S} + \text{H-S} \rightleftharpoons \text{H}_2\text{O-S}$	$\text{OH-S} + \text{H-S} \rightleftharpoons \text{H}_2\text{O-S}$
$\text{H}_2\text{O-S} \rightleftharpoons \text{H}_2\text{O} + \text{S}$	$\text{H}_2\text{O-S} \rightleftharpoons \text{H}_2\text{O} + \text{S}$

The two most distinctive among the derived models are: Model A and Model B (see Table 5.5). The detailed derivation of these models with the assumptions made are presented below.

Derivation of Model A

Model A is derived by assuming the redox mechanism for the formation of CO_{ad} and the CO dissociation mechanism for the formation of CH₄. Based on this mechanism, one of the earliest mechanistic kinetic model for CO₂ methanation was derived²⁷ (ref Weatherbee and Bartholomew) (Table 5.3).

Table 5.3 Mechanism assumed in the derivation of Model A
Elementary Steps

1	$H_2 + 2S \rightleftharpoons 2 H-S$
2	$CO_2 + 2S \rightleftharpoons CO-S+O-S$
3	$CO-S \rightleftharpoons CO + S$
4	$O-S + H-S \rightleftharpoons OH-S + S$
5	$OH-S + H-S \rightleftharpoons H_2O-S$
6	$H_2O-S \rightleftharpoons H_2O + S$
7	$CO-S + S \rightleftharpoons C-S + O-S$
8	$C-S + H-S \rightleftharpoons CH-S + S$
9	$CH-S + H-S \rightleftharpoons CH_2-S + S$
10	$CH_2-S + 2 H-S \rightleftharpoons CH_4-S + 2S$
11	$CH_4-S \rightleftharpoons CH_4 + S$

It was reported that the dissociative adsorption of H₂ on nickel is faster and has a lower energy barrier than that of CO₂.^{32,79} Therefore, it was assumed that step 2 is the rate determining step for the r-WGS reaction. On the other hand, step 7 i.e. the dissociation of CO into C and O, was considered to be rate limiting in the formation of CH₄. The assumption is in accordance with the work Choe et al. who used Atomic Superposition and Electron Delocalization-Molecular Orbital theory (ASED-MO) to investigate carbon formation and hydrogenation for CO₂ methanation on Ni (111) surface⁹⁷. They calculated the activation energy for the different elementary steps and concluded that the activation energy of CO dissociation (2.97 eV) is higher than the formation of methylidyne (0.72 eV), methylene (0.52 eV), and methane (0.5 eV). Apart from these

two rate determining steps, all other elementary steps are assumed to be fast and in quasi equilibrium. It follows:

$$K_1 = \frac{\theta_H^2}{p_{H_2} \theta^2}$$

$$r_2 = k_2 \left(p_{CO_2} \theta^2 - \frac{\theta_{CO} \theta_O}{K_2} \right)$$

$$K_3 = \frac{p_{CO} \theta}{\theta_{CO}}$$

$$K_4 = \frac{\theta_{OH} \theta}{\theta_O \theta_H}$$

$$K_5 = \frac{\theta_{H_2O} \theta}{\theta_O \theta_{OH}}$$

$$K_6 = \frac{p_{H_2O} \theta}{\theta_{H_2O}}$$

$$r_7 = k_7 \left(\theta_{CO} \theta - \frac{\theta_C \theta_O}{K_7} \right)$$

$$K_8 = \frac{\theta_{CH} \theta}{\theta_C \theta_H}$$

$$K_9 = \frac{\theta_{CH_2} \theta}{\theta_{CH} \theta_H}$$

$$K_{10} = \frac{\theta_{CH_4} \theta^2}{\theta_{CH_2} \theta_H^2}$$

$$K_{11} = \frac{p_{CH_4} \theta}{\theta_{CH_4}}$$

Nine different surface reactive intermediates are involved: H-S, CO-S, O-S, C-S, CH-S, CH₂-S, CH₄-S, OH-S, H₂O-S. Their coverage can be calculated as follows:

$$\theta_H = K_1^{1/2} p_{H_2}^{1/2} \theta$$

$$\theta_{H_2O} = \frac{p_{H_2O} \theta}{K_6}$$

$$\theta_{CO} = \frac{p_{CO} \theta}{K_3}$$

$$\theta_{CH_4} = \frac{p_{CH_4} \theta}{K_{11}}$$

To calculate θ_O in terms of the components of gaseous phase:

$$\frac{\theta_{OH} \theta}{\theta_O \theta_H} \frac{\theta_{H_2O} \theta}{\theta_O \theta_{OH}} \frac{p_{H_2O} \theta}{\theta_{H_2O}} = K_4 K_5 K_6$$

$$\frac{\theta^3 p_{H_2O}}{\theta_O \theta_H^2} = K_4 K_5 K_6$$

$$\frac{\theta^3 p_{H_2O}}{\theta_O K_1 p_{H_2} \theta^2} = K_4 K_5 K_6$$

$$\theta_O = \frac{p_{H_2O} \theta}{K_1 K_4 K_5 K_6 p_{H_2}}$$

To calculate θ_{OH} in terms of the components of gaseous phase:

$$\frac{\theta_{OH} \theta}{\theta_O \theta_H} = K_4$$

$$\theta_{OH} = \frac{K_4 \theta_O \theta_H}{\theta} = \frac{K_4}{\theta} \frac{p_{H_2O} \theta}{K_1 K_4 K_5 K_6 p_{H_2}} K_1^{1/2} p_{H_2}^{1/2} \theta = \frac{p_{H_2O} \theta}{K_1^{1/2} K_5 K_6 p_{H_2}^{1/2}}$$

Similarly,

$$\theta_C = \frac{p_{CH_4} \theta}{K_8 K_9 K_{10} K_{11} K_1^2 p_{H_2}^2}$$

$$\theta_{CH} = \frac{p_{CH_4} \theta}{K_9 K_{10} K_{11} K_1^{3/2} p_{H_2}^{3/2}}$$

$$\theta_{CH_2} = \frac{p_{CH_4} \theta}{K_{10} K_{11} K_1 p_{H_2}}$$

The net reaction rate for CO formation:

$$r_2 = k_2 \left(p_{CO_2} \theta^2 - \frac{p_{CO} p_{H_2O} \theta^2}{K_1 K_2 K_3 K_4 K_5 K_6 p_{H_2}} \right) = k_2 \left(p_{CO_2} - \frac{p_{CO} p_{H_2O}}{K_1 K_2 K_3 K_4 K_5 K_6 p_{H_2}} \right) \theta^2$$

But,

$$K_1 K_2 K_3 K_4 K_5 K_6 = \frac{p_{H_2O} p_{CO}}{p_{H_2} p_{CO_2}} = K_{e_{r-WGS}}$$

$$r_2 = k_2 p_{CO_2} \left(1 - \frac{p_{CO} p_{H_2O}}{K_{e_{r-WGS}} p_{H_2} p_{CO_2}} \right) \theta^2$$

The net reaction rate for CH₄ formation:

$$r_7 = k_7 \left(p_{CO} \theta^2 - \frac{p_{CH_4} p_{H_2O} \theta^2}{K_1^3 K_3^{-1} K_4 K_5 K_6 K_7 K_8 K_9 K_{10} K_{11} p_{H_2}^3} \right)$$

$$= k_7 p_{CO} \left(1 - \frac{p_{CH_4} p_{H_2O}}{K_1^3 K_3^{-1} K_4 K_5 K_6 K_7 K_8 K_9 K_{10} K_{11} p_{CO} p_{H_2}^3} \right) \theta^2$$

But,

$$K_1^3 K_3^{-1} K_4 K_5 K_6 K_7 K_8 K_9 K_{10} K_{11} = \frac{p_{H_2O} p_{CH_4}}{p_{H_2}^3 p_{CO}} = Ke_{Meth}$$

$$r_7 = k_7 p_{CO} \left(1 - \frac{p_{CH_4} p_{H_2O}}{Ke_{Meth} p_{CO} p_{H_2}^3} \right) \theta^2$$

The normalized concentration of the free active sites θ can be calculated using:

$$1 = \theta + \theta_H + \theta_{OH} + \theta_O + \theta_{H_2O} + \theta_{CO} + \theta_C + \theta_{CH} + \theta_{CH_2} + \theta_{CH_4}$$

$$\theta^{-1} = 1 + K_1^{1/2} p_{H_2}^{1/2} + \frac{p_{H_2O}}{K_1^{1/2} K_5 K_6 p_{H_2}^{1/2}} + \frac{p_{H_2O}}{K_1 K_4 K_5 K_6 p_{H_2}} + \frac{p_{H_2O}}{K_6} + \frac{p_{CO}}{K_3} + \frac{p_{CH_4}}{K_8 K_9 K_{10} K_{11} K_1^2 p_{H_2}^2}$$

$$+ \frac{p_{CH_4}}{K_9 K_{10} K_{11} K_1^{3/2} p_{H_2}^{3/2}} + \frac{p_{CH_4}}{K_{10} K_{11} K_1 p_{H_2}} + \frac{p_{CH_4}}{K_{11}}$$

The rate expressions can be further simplified by assuming specific surface species as Most Abundant Surface Intermediates (MASI). The best result was obtained by considering H, H₂O, OH, CO and C to be MASI.

$$1 = \theta + \theta_H + \theta_{H_2O} + \theta_{HO} + \theta_{CO} + \theta_C$$

$$\theta^{-1} = 1 + K_{H_2}^{1/2} p_{H_2}^{1/2} + K_{H_2O} p_{H_2O} + \frac{K_{mix,OH} p_{H_2}^{1/2}}{p_{H_2O}} + \frac{K_{mix,C} p_{H_2}^2}{p_{CH_4}} + \frac{K_3}{p_{CO}}$$

Derivation of Model B

Model B was developed by assuming that both the formation of CO and CH₄ via hydrogen assisted mechanisms. The formation of COOH and HCO are considered to be the rate determining step for both r-WGS and CO methanation respectively. All other steps are assumed to be fast and are at quasi equilibrium except for the desorption of CO.

Table 5.4 Mechanism assumed in the derivation of Model B
Elementary Steps

1	$H_2 + 2S \rightleftharpoons 2 H-S$
2	$CO_2 + S \rightleftharpoons CO_2-S$
3	$CO_2-S + H-S \rightleftharpoons COOH-S + S$
4	$COOH-S + S \rightleftharpoons CO-S + HO-S$
5	$CO-S \rightleftharpoons CO + S$
6	$CO-S + H-S \rightleftharpoons HCO-S + S$
7	$HCO-S + S \rightleftharpoons CH-S + O-S$
8	$CH-S + H-S \rightleftharpoons CH_2-S + S$
9	$CH_2-S + 2 H-S \rightleftharpoons CH_4-S + 2S$
10	$CH_4-S \rightleftharpoons CH_4 + S$
11	$O-S + H-S \rightleftharpoons OH-S + S$
12	$OH-S + H-S \rightleftharpoons H_2O-S$
13	$H_2O-S \rightleftharpoons H_2O + S$

Step 3 is assumed to be the rate determining step for the r-WGS reaction:

$$r_{r-WGS} = r_3 = k_3 \theta_{CO_2} \theta_H$$

$$\theta_{CO_2} = K_{CO_2} p_{CO_2} \theta$$

$$\theta_H = K_{H_2}^{1/2} p_{H_2}^{1/2} \theta$$

$$r_{r-WGS} = r_3 = k_3 K_{CO_2} K_{H_2}^{1/2} p_{CO_2} p_{H_2}^{1/2} \theta^2$$

For thermodynamic consistency,

$$r_{r-WGS} = k_3 K_{CO_2} K_{H_2}^{1/2} p_{CO_2} p_{H_2}^{1/2} \left(1 - \frac{P_{CO} P_{H_2O}}{P_{H_2} P_{CO_2} K_{RWGS}}\right) \theta^2$$

Step 6 is assumed to be the rate determining step for the CO methanation reaction:

$$r_{COMeth} = k_6 \theta_{CO} \theta_H$$

To calculate θ_{CO} , we use the steady state approximation for CO_{ad} and $COOH_{ad}$:

$$\frac{d\theta_{CO}}{dt} = r_4 - r_5 - r_6 = 0$$

$$\frac{d\theta_{COOH}}{dt} = r_3 - r_4 = 0$$

It follows that,

$$r_3 = r_5 + r_6$$

The rate of CO desorption is assumed irreversible,

$$r_5 = k_5 \theta_{CO}$$

$$k_3 \theta_{CO_2} \theta_H = k_5 \theta_{CO} + k_6 \theta_{CO} \theta_H$$

$$\theta_{CO} = \frac{k_3 \theta_{CO_2} \theta_H}{k_5 + k_6 \theta_H}$$

$$\theta_{CO} = \frac{k_3 K_{CO_2} p_{CO_2} \theta K_{H_2}^{1/2} p_{H_2}^{1/2} \theta}{k_5 + k_6 K_{H_2}^{1/2} p_{H_2}^{1/2} \theta} = \frac{k_3 K_{CO_2} K_{H_2}^{1/2} p_{CO_2} p_{H_2}^{1/2} \theta}{\left(\frac{k_5}{\theta} + k_6 K_{H_2}^{1/2} p_{H_2}^{1/2}\right)}$$

$$r_{COMeth} = k_6 \frac{k_3 K_{CO_2} K_{H_2}^{1/2} p_{CO_2} p_{H_2}^{1/2} \theta}{\left(\frac{k_5}{\theta} + k_6 K_{H_2}^{1/2} p_{H_2}^{1/2}\right)} K_{H_2}^{1/2} p_{H_2}^{1/2} \theta = \frac{k_6 k_3 K_{CO_2} K_{H_2} p_{CO_2} p_{H_2} \theta^2}{\left(\frac{k_5}{\theta} + k_6 K_{H_2}^{1/2} p_{H_2}^{1/2}\right)}$$

For thermodynamic consistency,

$$r_{COMeth} = \frac{k_6 k_3 K_{CO_2} K_{H_2} p_{CO_2} p_{H_2} \left(1 - \frac{p_{CH_4} p_{H_2O}}{p_{H_2}^3 p_{CO} K_{COMeth}}\right) \theta^2}{\left(\frac{k_5}{\theta} + k_6 K_{H_2}^{1/2} p_{H_2}^{1/2}\right)}$$

$$\theta_{H_2O} = K_{H_2O} p_{H_2O} \theta$$

By assuming that H_2O , CO_2 and H are the most abundant surface intermediates, the normalized concentration of the free active sites θ can be calculated using:

$$1 = \theta + \theta_H + \theta_{H_2O} + \theta_{CO_2}$$

$$\theta^{-1} = 1 + K_{H_2}^{1/2} p_{H_2}^{1/2} + K_{H_2O} p_{H_2O} + K_{CO_2} p_{CO_2}$$

5.3.3 Parameter estimation and Model discrimination

The data collected from the kinetic experiments were fitted against the derived models and some other models reported in literature for both r-WGS and CO methanation reactions (Table 5.5). Since the system includes more than one dependent variable or response ($r_{r\text{-WGS}}$ and r_{COMeth}), the ‘determinant criterion’ approach, originally proposed by Box and Draper, was used for estimating the model parameters. This estimation criterion is obtained from the Bayesian argument and is based on minimizing the determinant of the matrix of the sum of squares and the cross-products of the residuals.⁹⁸ Therefore, unlike the classical weighted least square method which is used often in the parameter estimation of single response models and is seldom applied for multi response system, the ‘determinant criterion’ method takes into account the correlation between the different responses. The nonlinear optimization problem, which was solved in MATLAB[®] using the function *fmincon*, had the following structure:

$$\min |\mathbf{Z}^T \mathbf{Z}|$$

s.t:

$$\mathbf{h}(\mathbf{x}, \mathbf{p}) = 0$$

$$\text{LB} \leq \mathbf{p} \leq \text{UB}$$

where $\mathbf{Z} = [\mathbf{z}_{r\text{-WGS}}, \mathbf{z}_{\text{COMeth}}]_{n \times m}$, \mathbf{z}_j is the error vector and is equal to $(\check{r}_j - r_j(\mathbf{x}, \mathbf{p}))$, n is the number of data points, m is the number of dependent variables ($r_{r\text{-WGS}}$, r_{COMeth}), \check{r}_j is the experimentally measured rate of reaction j , \mathbf{x} is the vector of state variables (T, p_i), and \mathbf{p} represents the set of parameters. (Please note that, for convenience, through the rest of the chapter, bold text will not be used any further to distinguish vectors and matrices)

It follows that:

$$\mathbf{Z}^T \mathbf{Z} = \begin{bmatrix} (\check{r}_{r\text{-WGS}} - r_{r\text{-WGS}}(\mathbf{x}, \mathbf{p}))^T (\check{r}_{r\text{-WGS}} - r_{r\text{-WGS}}(\mathbf{x}, \mathbf{p})) & (\check{r}_{r\text{-WGS}} - r_{r\text{-WGS}}(\mathbf{x}, \mathbf{p}))^T (\check{r}_{\text{COMeth}} - r_{\text{COMeth}}(\mathbf{x}, \mathbf{p})) \\ (\check{r}_{\text{COMeth}} - r_{\text{COMeth}}(\mathbf{x}, \mathbf{p}))^T (\check{r}_{r\text{-WGS}} - r_{r\text{-WGS}}(\mathbf{x}, \mathbf{p})) & (\check{r}_{\text{COMeth}} - r_{\text{COMeth}}(\mathbf{x}, \mathbf{p}))^T (\check{r}_{\text{COMeth}} - r_{\text{COMeth}}(\mathbf{x}, \mathbf{p})) \end{bmatrix}$$

Since a consecutive route for the CO₂ methanation is assumed, the reverse water gas shift and CO methanation reaction rates are related to the formation rate of CO and CH₄ according to Eq. (5.1) and Eq. (5.2):

$$r_{r-WGS} = r_{CO} + r_{CH_4} \quad (5.1)$$

$$r_{COMeth} = r_{CH_4} \quad (5.2)$$

The reaction rate and the adsorption constants of the kinetic models were described using the Arrhenius and van't Hoff equations respectively (Eq. (5.3) and Eq. (5.4)).

$$k_j = k_{0,j} \exp\left(\frac{-E_{a,j}}{RT}\right) \quad j = \{r-WGS, COMeth\} \quad (5.3)$$

$$K_i = K_{0,i} \exp\left(\frac{-\Delta H_i}{RT}\right) \quad i = \{H_2, CO_2, CH_4, CO, H_2O\} \quad (5.4)$$

However, in order to decouple the pre-exponential factors from the activation energy and adsorption enthalpies, these equations were parameterized:

$$k_j = k_{r,j} \exp\left(\frac{-E_{a,j}}{R} \left(\frac{1}{T_r} - \frac{1}{T}\right)\right) \quad (5.5)$$

$$K_i = K_{r,i} \exp\left(\frac{-\Delta H_i}{R} \left(\frac{1}{T_r} - \frac{1}{T}\right)\right) \quad (5.6)$$

$k_{r,j}$ and $K_{r,i}$ were estimated first using data collected at the reference temperature $T_r = 623$ K.

The fitting of the models was demonstrated by means of parity plots (see below). The Root Mean Squared Error (RMSE) and the Average Absolute Deviation (AAD) were used to measure the goodness of fitting (see Eq. (5.7) and Eq. (5.8)) and served as the first criteria to discriminate between the different models:

$$RMSE_j = \sqrt{\frac{\sum_{i=1}^n (\tilde{r}_{ji} - r_{ji})^2}{n}} \quad (5.7)$$

$$AAD_j = \frac{\sum_{i=1}^n |\tilde{r}_{ji} - r_{ji}|}{n} \quad (5.8)$$

However, the discrimination between the more rivalry models was done via the Bayesian Information Criterion (BIC). It is calculated using the equation derived by Schwartz (see Eq. (5.9)).³⁴

$$BIC = n \ln\left(\frac{RSS}{n}\right) + n_p \ln(n) \quad (5.9)$$

where RSS is the sum of squared residuals and n_p are the number of parameters.

The 95% confidence interval of the parameter estimates is calculated from the t values and the diagonal elements of the covariance matrix of the parameter estimates ($C(\hat{p})$) according to Eq. (5.10).

$$p_q = \hat{p}_q \pm t_{n-n_p, \frac{0.05}{2}} \sqrt{C(\hat{p})_{qq}} \quad (5.10)$$

where qq is the diagonal element of the q^{th} parameter, and p is the true parameter.

The covariance matrix, which is the inverse of the Fisher information matrix, is computed for the collected data points and the parameter estimates. The covariance matrix based on the determinant criterion approach was derived by Kang and Bates as:⁹⁹

$$C(\hat{p}) = (n \Lambda_B)^{-1} \quad (5.11)$$

$$\Lambda_B = \sum_{u=1}^n X_u^T (\hat{Z}^T \hat{Z})^{-1} X_u \quad (5.12)$$

$$X_u = \frac{\partial r_j(x_u, p)}{\partial p_q} \quad (5.13)$$

5.3.4 Quantitative identifiability of the parameters

The development of mechanistic kinetic models based on elementary steps usually results in nonlinear *parameter combinations* in the rate expression, on which the goodness-of-fit of the model mainly depends. Therefore, any attempt to estimate all individual parameters simultaneously may result in nearly singular estimation problem, practical unidentifiability, and meaningless estimates⁴. In such cases, it is recommended to perform ‘partial’ parameter estimation i.e. to estimate only some of the parameters while keeping the others fixed at the best experimental or theoretical values available⁴. This is why it is important, following the selection of the most adequate model, to

investigate whether all model parameters can be quantitatively identified and to determine their significance.

The quantitative identifiability and the dependencies among the parameters were assessed, in this work, using a method that was proposed by Vajda et al. and is based on the Principal Component Analysis.³ First, the ($n_p \times n_p$) Fisher information matrix is calculated using normalized first derivatives/sensitivities. Then, it is decomposed into eigenvalues (λ) and eigenvectors. The magnitudes of the resulting eigenvalues provide an indication of whether all individual parameters can be simultaneously identified or not. The presence of small eigenvalues suggests that certain parameters have very large variances and are therefore practically unidentifiable. In this case, the coefficients of the normed eigenvector corresponding to the smallest eigenvalue can be used to determine: (1) which of the parameters is unidentifiable and (2) if the objective function is dependent on the product or the ratio of certain parameters rather than on each of them separately.

In their work, Vajda et al. comprehensively demonstrated this by considering a hypothetical case whereby the normed eigenvector corresponding to the smallest eigenvalue had the form: $u=[u_1, u_2, 0, 0, 0]^T$. According to Vajda et al, the objective function, in this case, would be dependent, not on p_1 and p_2 separately, but on a combination of the original parameters defined as:

$$\frac{p_1}{p_2^{C_2}} \text{ with } C_2 = \frac{u_1}{u_2}$$

In other words, these two parameters can not be identified individually. Under such scenario, and for a more sensible parameter estimation, only one of the two parameters should be left 'free' to be estimated while the other parameter is fixed at a nominal value.

Nevertheless, if one coefficient of the normed eigenvector, corresponding to the smallest eigenvalue is significantly larger than all other coefficients, then the original parameter associated with this coefficient is unidentifiable.⁴

Once an unidentifiable parameter is detected on the basis of this principal component analysis, it is eliminated. The Fisher information matrix is re-evaluated using the sensitivities of the remaining parameters and is eigen-decomposed. And, as in the first principal component analysis, if a new unidentifiable parameter is revealed, it is eliminated. Again, the fisher information matrix is recalculated and eigen-decomposed. These steps are repeated recursively until all computed eigenvalues are larger than a threshold value ($\lambda_{\min} > \lambda_{\text{thr}}$). This whole process results in a successive elimination of small eigenvalues and subsequently the unidentifiable parameters. The parameters corresponding to the remaining ‘large’ eigenvalues are quantitatively identifiable.

Once all unidentifiable parameters are determined, a new parameter estimation procedure is carried out whereby the identifiable parameters are re-estimated unlike the eliminated parameters are fixed at their nominal values.

This procedure is done separately for the two sets of estimated parameters, the set of rate constants obtained at the reference temperature and the other set containing the activation energies and adsorption enthalpies.

Table 5.5 Reported and derived kinetic models for the r-WGS and the CO methanation reaction

Model A
$r_{r-WGS} = k_2 p_{CO_2} \left(1 - \frac{p_{CO} p_{H_2O}}{K_{r-WGS} p_{H_2} p_{CO_2}} \right) \theta^2$
$\theta^{-1} = 1 + K_{H_2}^{1/2} p_{H_2}^{1/2} + K_{H_2O} p_{H_2O} + \frac{K_{mix,OH} p_{H_2}^{1/2}}{p_{H_2O}} + \frac{K_{mix,C} p_{H_2}^2}{p_{CH_4}} + \frac{K_3}{p_{CO}}$
$r_{COMeth} = k_7 p_{CO} \left(1 - \frac{p_{CH_4} p_{H_2O}}{K_{COMeth} p_{CO} p_{H_2}^3} \right) \theta^2$
Model B
$r_{r-WGS} = k_3 K_{CO_2} K_{H_2}^{1/2} p_{CO_2} p_{H_2}^{1/2} \left(1 - \frac{p_{CO} p_{H_2O}}{p_{H_2} p_{CO_2} K_{r-WGS}} \right) \theta^2$
$\theta^{-1} = 1 + K_{H_2}^{1/2} p_{H_2}^{1/2} + K_{H_2O} p_{H_2O} + K_{CO_2} p_{CO_2}$
$r_{COMeth} = \frac{k_6 k_3 K_{CO_2} K_{H_2} p_{CO_2} p_{H_2} \left(1 - \frac{p_{CH_4} p_{H_2O}}{p_{H_2}^3 p_{CO} K_{COMeth}} \right) \theta^2}{\left(\frac{k_5}{\theta} + k_6 K_{H_2}^{1/2} p_{H_2}^{1/2} \right)}$
Xu and Fromet Model ⁵⁰
$r_{r-WGS} = \frac{\frac{k_{WGS}}{p_{H_2}} \left(\frac{p_{H_2} p_{CO_2}}{K_{WGS}} - p_{CO} p_{H_2O} \right)}{\left(1 + K_{CO} p_{CO} + K_{H_2} p_{H_2} + K_{CH_4} p_{CH_4} + \frac{K_{H_2O} p_{H_2O}}{p_{H_2}} \right)^2}$
$r_{COMeth} = \frac{\frac{k_{COMeth}}{p_{H_2}^{2.5}} \left(p_{H_2}^3 p_{CO} - \frac{p_{CH_4} p_{H_2O}}{K_{COMeth}} \right)}{\left(1 + K_{CO} p_{CO} + K_{H_2} p_{H_2} + K_{CH_4} p_{CH_4} + \frac{K_{H_2O} p_{H_2O}}{p_{H_2}} \right)^2}$
Ronsch Model ⁹³
$r_{r-WGS} = \frac{\frac{k_{WGS}}{p_{H_2}} \left(\frac{p_{H_2} p_{CO_2}}{K_{WGS}} - p_{CO} p_{H_2O} \right)}{\left(1 + K_{CO} p_{CO} + K_{H_2} p_{H_2} + K_{CH_4} p_{CH_4} + \frac{K_{H_2O} p_{H_2O}}{p_{H_2}} \right)^2}$
$r_{COMeth} = \frac{k_{COMeth} \left(K_C K_H^2 p_{CO}^{0.5} p_{H_2} - K_C K_H^2 p_{CH_4} p_{H_2O} p_{CO}^{-0.5} p_{H_2}^{-2} \left(\frac{1}{K_{COMeth}} \right) \right)}{\left(1 + K_C p_{CO}^{0.5} + K_H p_{H_2}^{0.5} \right)^3}$

5.4 Results and discussion

5.4.1 Preliminary results

Apriori to the kinetic measurements, preliminary experiments were performed in order to investigate the activity, stability and selectivity of the catalyst. During these experiments, only CH₄, H₂O, and CO were detected as products at the reactor outlet.

It is well known that nickel based catalysts, during methanation reactions, are subjected to deactivation caused by Ni sintering and carbon deposition especially at high temperatures. Therefore, the stability of the catalyst was first investigated by feeding the reactor with a gas mixture containing H₂, CO₂, and N₂ (H₂:CO₂:N₂=13.33:3.33:83.33) at T=673 K, p=10 atm and a space velocity (SV) of 3.6 mol_{CO₂}/(hr g_c). Figure 5.2 shows the total conversion of CO₂ and the selectivity towards CH₄ ($S=r_{CH_4}/r_{CO_2}$) in the first 48 hours of time on stream.

A slight increase in the catalytic activity was observed over the first 5 hours of the reaction during which CO₂ conversion increased from 0.38 to 0.4. Afterwards, the conversion remained nearly constant towards the end of the reaction period demonstrating good catalytic stability. The CH₄ selectivity, on the other hand, was slightly above 0.8.

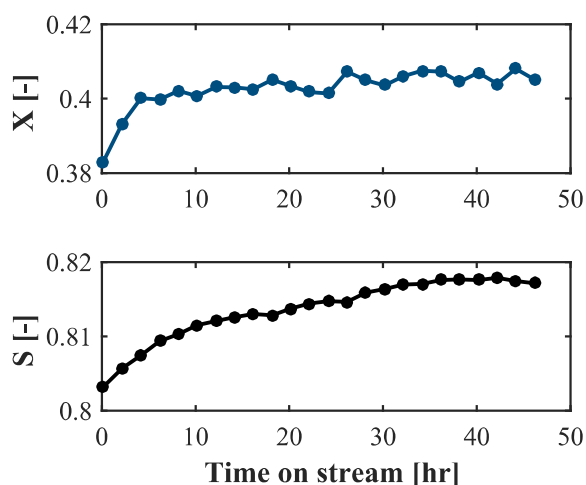


Figure 5.2 Stability test: Conversion and selectivity towards CH₄ versus time

Since the catalyst selectivity is usually dependent on the operating conditions, additional experiments were conducted over a range of temperature, pressure, feed composition and space velocity.

The influence of total pressure on the reaction system was first investigated. During these experiments, the reactor was fed with the gas mixture ($\text{H}_2:\text{CO}_2:\text{N}_2=16:4:80$) at $\text{SV}=0.16 \text{ mol}_{\text{CO}_2}/(\text{hr g}_c)$ and $T=570 \text{ K}$. As can be seen in Figure 5.3, CO_2 conversion increased from 0.28 to 0.41 (46%) by increasing the pressure from 6 to 30 atm. On one hand, increasing the total pressure under the same feed composition increases the partial pressure of the reactants and therefore the reaction rate. On the other hand, it decreases the average velocity of the mixture leading to a longer reactant-catalyst contact time (residence time) and thus higher conversion.

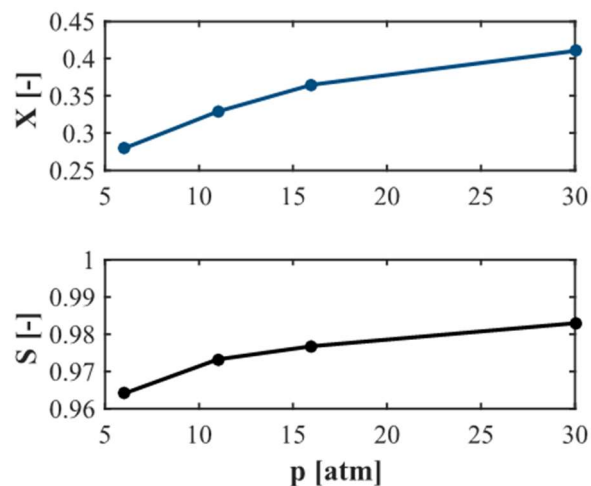


Figure 5.3 Influence of total pressure on CO_2 conversion and selectivity towards CH_4

Also, CH_4 selectivity increased with pressure from 0.96 at 6 atm to 0.98 at 30 atm. The selectivity was remarkably higher than the one observed in the long term stability experiment ($S=0.8$). This may be attributed to either the lower space velocity ($\text{SV}=0.16 \text{ mol}_{\text{CO}_2}/(\text{hr g}_c)$) or temperature ($T=570 \text{ K}$) under which these measurements were conducted compared to the stability experiment ($\text{SV}=3.66 \text{ mol}_{\text{CO}_2}/(\text{hr g}_c)$ $T=673 \text{ K}$). Therefore, the influence of these two variables (i.e. T and SV) on selectivity was further investigated.

Figure 5.4 shows the CO₂ conversion and the CH₄ selectivity as a function of space velocity (6.5-19.46 mol_{CO₂}/(hr g_c)) at two different temperatures (T=573 and 595 K). As expected, CO₂ conversion decreased with increasing space velocity (shorter residence time) as well as with decreasing temperature. The same trend was also observed for CH₄ selectivity. For example, at T= 595 K, selectivity decreased from 0.76 to 0.58 as the space velocity increased from 6.45 to 19.36 mol_{CO₂}/(hr g_c), and an increase in selectivity of 0.03 was observed by increasing the temperature from 573 to 595 K at SV=19.4 mol_{CO₂}/(hr g_c).

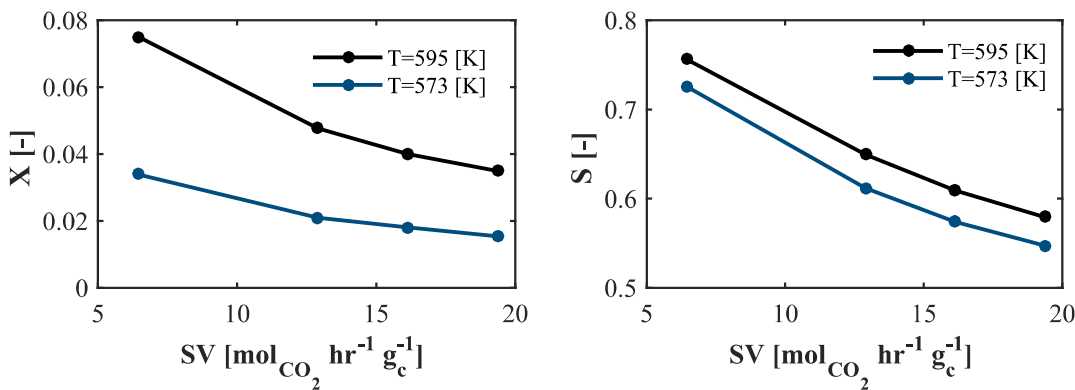


Figure 5.4 Influence of space velocity on CO₂ conversion and selectivity towards CH₄ at different temperature

This negative and significant correlation between selectivity and space velocity suggests that CH₄ formation follows the consecutive path: CO_{ad} is formed first via reverse water gas shift and is further reduced into CH₄ in CO methanation reaction. The higher the space velocity, the less is the contact time available for CO_{ad} to convert into methane and the higher is the amount of CO desorbing the catalytic bed. Since the CH₄ selectivity was always above 50 %, one can conclude that the formation of CH₄ is faster than the desorption of CO ($r_{CH_4} > r_{CO}$). Moreover, the increase in CH₄ selectivity with increasing temperature indicates that the activation energy of CO methanation is larger than the activation energy of r-WGS reaction.

5.4.2 Influence of Temperature

The influence of temperature on the reaction system was also investigated. Figure 5.5, for example, shows the rate of formation of CH₄ and CO measured over a temperature

range of 540-620 K. The plotted data was obtained by feeding a gas mixture of $H_2/CO_2/N_2$ into the reactor at $p=6.8$ atm and using three different inlet compositions (40:10:50, 60:10:30, 40:40:20). As expected, the rate of formation of CH_4 and CO increased with temperature. The collected data also confirmed the positive correlation between CH_4 selectivity and temperature which was observed earlier in Figure 5.4. One can also note from Figure 5.5 that the ratio of H_2 to CO_2 can significantly influence the rate of formation of CO and CH_4 . For $x_{H_2,in}/x_{CO_2,in} \geq 4$, the rate of CH_4 formation is greater than that of CO. In contrast, an equimolar feed of CO_2 and H_2 leads to a significant increase in CO formation and a comparably lower amount of CH_4 is produced. This can be explained by the absence of sufficient amount of H_2 needed to further reduce the produced CO into CH_4 . Figure 5.5 also shows that the effect of inlet composition on the rates of formation is more pronounced at higher temperatures. Therefore, the effect of H_2 and CO_2 on the reaction rates was systematically studied afterwards by varying the inlet composition of the reactants at relatively high temperature.

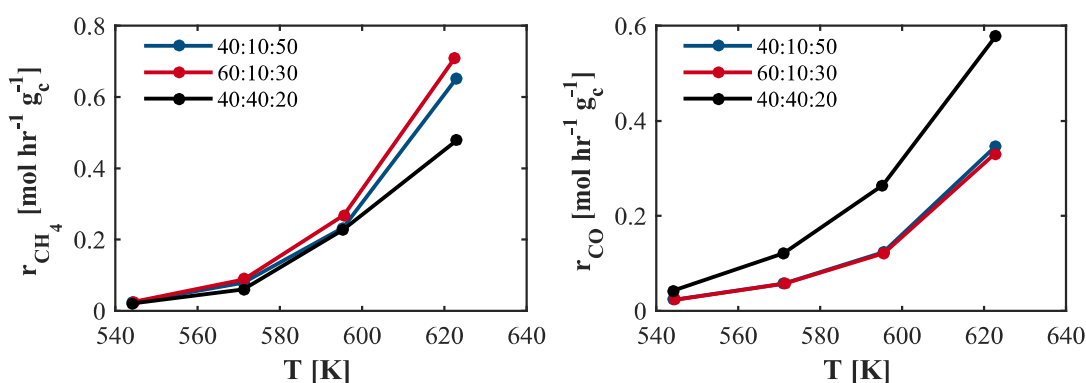


Figure 5.5 Influence of Temperature and inlet composition on the rate formation of CH_4 and CO ($p=6.86$ atm, $x_{H_2,in}/x_{CO_2,in}=4$, $SV=19.36$ mol $_{CO_2}/(hr$ g $_c)$)

5.4.3 Influence of H_2 and CO_2

For the first set of experiments (Figure 5.6), a gas mixture of $H_2/CO_2/N_2/H_2O$ was fed into the reactor at $T=623$ K and $p=6$ atm. Initially, the inlet composition of H_2 was varied between 0.38 and 0.56 while that of CO_2 was kept constant at 0.093. Afterwards, H_2 inlet composition was fixed at 0.56 whereas the inlet composition of CO_2 ranged

from 0.046 to 0.092. In this series of experiments, the inlet composition of H₂O was set at 0.1, and the total amount was balanced by N₂.

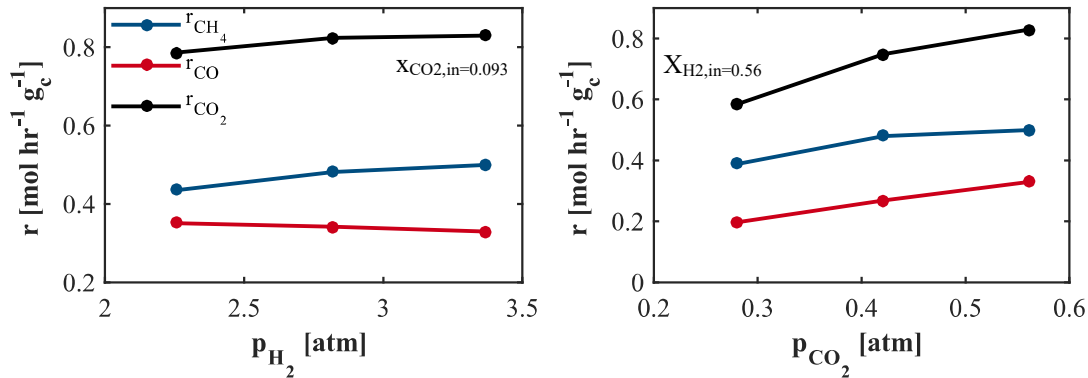


Figure 5.6 Influence of H₂ and CO₂ partial pressure on the rate of disappearance of CO₂ and the rate of formation of CO and CH₄ (T=623 K, p=6 atm, SV=12.9 mol_{CO₂/(hr g_c)}

As the partial pressure of H₂ increased from 2.26 to 3.37 atm, the rate of CO₂ disappearance and CH₄ formation increased from 0.79 to 0.83 and from 0.44 to 0.5 mol_{CO₂/(hr g_c) respectively. The magnitude of this increase In contrast, a slight decrease in the rate of CO formation from 0.35 to 0.33 mol_{CO₂/(hr g_c) was observed. On the other hand, increasing the partial pressure of CO₂ increases the rate of disappearance of CO₂ as well as the rates CO and CH₄ formation. Also, one can conclude that the impact of CO₂ on these rates is more significant compared to H₂. For example, increasing the partial pressure of CO₂ from 0.28 to 0.56 atm causes the rate of CO₂ disappearance to increase from 0.58 to 0.83 mol_{CO₂/(hr g_c).}}}

5.4.4 Influence of H₂O

The influence of H₂O on the formation of CO and CH₄ was also investigated. Figure 5.7 shows the rate of CO and CH₄ formation as a function of the partial pressure of H₂O at two different temperatures (T=623 and T=653 K). During this set of measurements, the reactor was fed, at p=3.2 atm, with a gas mixture of H₂/CO₂/H₂O/N₂ at H₂:CO₂ of 4. As can be seen from this figure, increasing the partial pressure of H₂O decreased both CO and CH₄ formation rates especially at high temperatures. The hindering effect of H₂O, however, was more pronounced on the rate of CH₄ formation. For instance, increasing the partial pressure of H₂O from 0.35 to 0.6 atm lead to a decrease in the rate of CH₄

formation from 0.43 to 0.35 mol_{CO₂}/(hr g_c) whereas CO formation rate decreased from 0.55 to 0.51 mol_{CO₂}/(hr g_c). This negative correlation between the reaction rates and the H₂O partial pressure can be explained. By increasing the partial pressure of H₂O, the rate of the backward reactions (Methane Steam Reforming and Water Gas Shift) increases thus decreasing the amount of CO and CH₄ produced. Furthermore, the number of H₂O molecules binding to the active sites of the catalyst also increases hence partially blocking H₂ and CO₂ from adsorbing. It should also be noted that during these measurements, CH₄ selectivity was below 0.5.

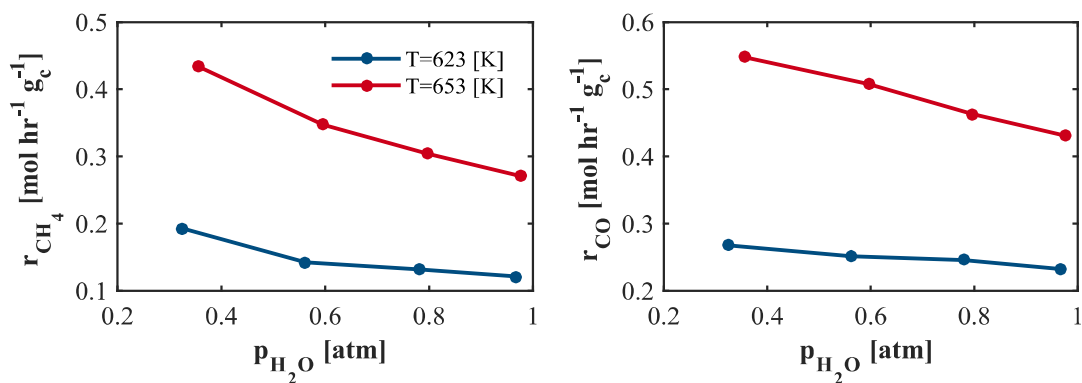


Figure 5.7 Influence of partial pressure of H₂O on the formation rate of CH₄ and CO (p=3.2 atm, X_{H₂,in}/X_{CO₂,in}=4, SV=9.68 mol_{CO₂}/(hr g_c))

5.4.5 Regression analysis: Comparison of results obtained for different kinetic models

As mentioned earlier, over 75 data points were collected over a wide range of temperature, pressure and inlet compositions. The data was then fitted against the derived models and some other models reported in literature. Consequently, proper sets of parameters for the various kinetic models were estimated by minimizing the determinant of the matrix of the sum of squares and the cross-products of the residuals.

Figure 5.8 compares the parity plots of four selected kinetic models each comprising of r-WGS and CO methanation rate expressions (Table 5.5).

As can be seen from this figure, the predictions of Model A showed the largest deviation from the experimental data especially with respect to the rate of CO methanation. The BIC calculated for this model was the highest among all other models

(BIC=-175), and the F values were notably low ($F_{\text{COMeth}}=87.9$ and $F_{\text{r-WGS}}=347$). One main reason for the discrepancy is the model inability to capture the positive effect of H₂ on CO₂ conversion and CH₄ formation that was observed during the experiments. Actually, the partial pressure of H₂ appears only in the denominator of the rate expressions thus giving H₂ rather an inhibiting role. The parity plots of the model developed by Froment and Xu, on the other hand, showed a more satisfactory correlation between the experimental and predicted values particularly for CO methanation (BIC=180.95). F values of 362 and 311 were calculated for r-WGS and CO methanation kinetic equations respectively. It is worth noting, however, that the mechanism proposed by Xu and Froment to derive the model was based on the Methane Steam Reforming reaction.

Ronsch et al. combined rate expressions for r-WGS and CO methanation reactions that were originally developed by Xu and Froment and Klose et al. respectively. The rate expression for the CO methanation showed very good fitting with an AAD of 0.051 while that computed for the r-WGS rate equation was inadequately higher at 0.095. It should be noted, however, that the two rate expressions don't share the same denominator. This is owed to the fact that while Xu and Froment assumed the catalytic surface to be aplenty covered with CO, H₂O, H₂, and CH₄, while Klose et al. considered adsorbed carbon and hydrogen atoms to be the most abundant surface intermediates.¹⁰⁰ Since the two reactions take place on the same active sites, claiming different species coverage for each reaction is unrealistic.

Model B, which was developed on the basis of mechanistic insights provided by published experimental and theoretical studies and our own collected data, had the lowest computed BIC (BIC=-198.8) and thus showed the best fitting with minimal deviation between experimental and predicted values. Examining both rate expressions of this model shows that they predict a positive influence of H₂ and CO₂ on both r-WGS and CO methanation reactions which is in agreement with the experimental results shown in Figure 5.6. Moreover, this model takes into account the inhibiting influence of

H₂O (see Figure 5.7) by including a H₂O adsorption term in the denominator of the rate expressions.

Based on the above results, Model B was selected as the most adequate kinetic model. Subsequently, the parameters of this model are checked for their quantitative identifiability using the method of Vajda as explained earlier. The result of the principal component analysis at the determinant criterion estimates of the rate and equilibrium constants ($k_{j,r}$ and $K_{i,r}$) is shown in Table 5.6. As can be seen, the problem is nearly singular since λ_{\min} , the smallest computed eigenvalue, is close to zero ($\lambda_5=2.2\times 10^{-13}$) and is significantly smaller than the threshold value ($\lambda_{th}=50$). A threshold value of 50 is assumed in this work since it leads to acceptable small variances in the parameter estimates. By examining the normed eigenvector corresponding to the smallest eigenvalue, λ_5 , one can conclude that the objective function is dependent on the ratio of $k_{5,r}$ and $k_{6,r}$ and not on their individual values. In other words, for a sensible parameter estimation problem, only one of these parameters can be identified while the other should be kept at a fixed nominal value. We decide to fix $k_{5,r}$ and is therefore eliminated for the next principal component analysis.

Table 5.7 lists the result of the second principal component analysis of the remaining parameters ($k_{3,r}$, $k_{6,r}$, $K_{H_2,r}$, $K_{H_2O,r}$, $K_{CO_2,r}$). The smallest eigenvalue, $\lambda_4=32$, is still smaller than the threshold value. The corresponding normed eigenvector reveals that the objective function is, again, dependent on a combination of parameters rather than on individual ones. Of particular interest are the ones with the highest coefficients and these are $K_{H_2,r}$, and $K_{H_2O,r}$. Again, one of the parameters needs to be fixed, $K_{H_2O,r}$, and is therefore eliminated for the next principal component analysis. The third principal component analysis (Table 5.8), shows that the smallest computed eigenvalue is now larger than the threshold value. As a result, all remaining parameters ($k_{3,r}$, $k_{6,r}$, $K_{H_2,r}$, $K_{CO_2,r}$) are identifiable.

Model-based optimization and experimental investigation of CO₂ methanation

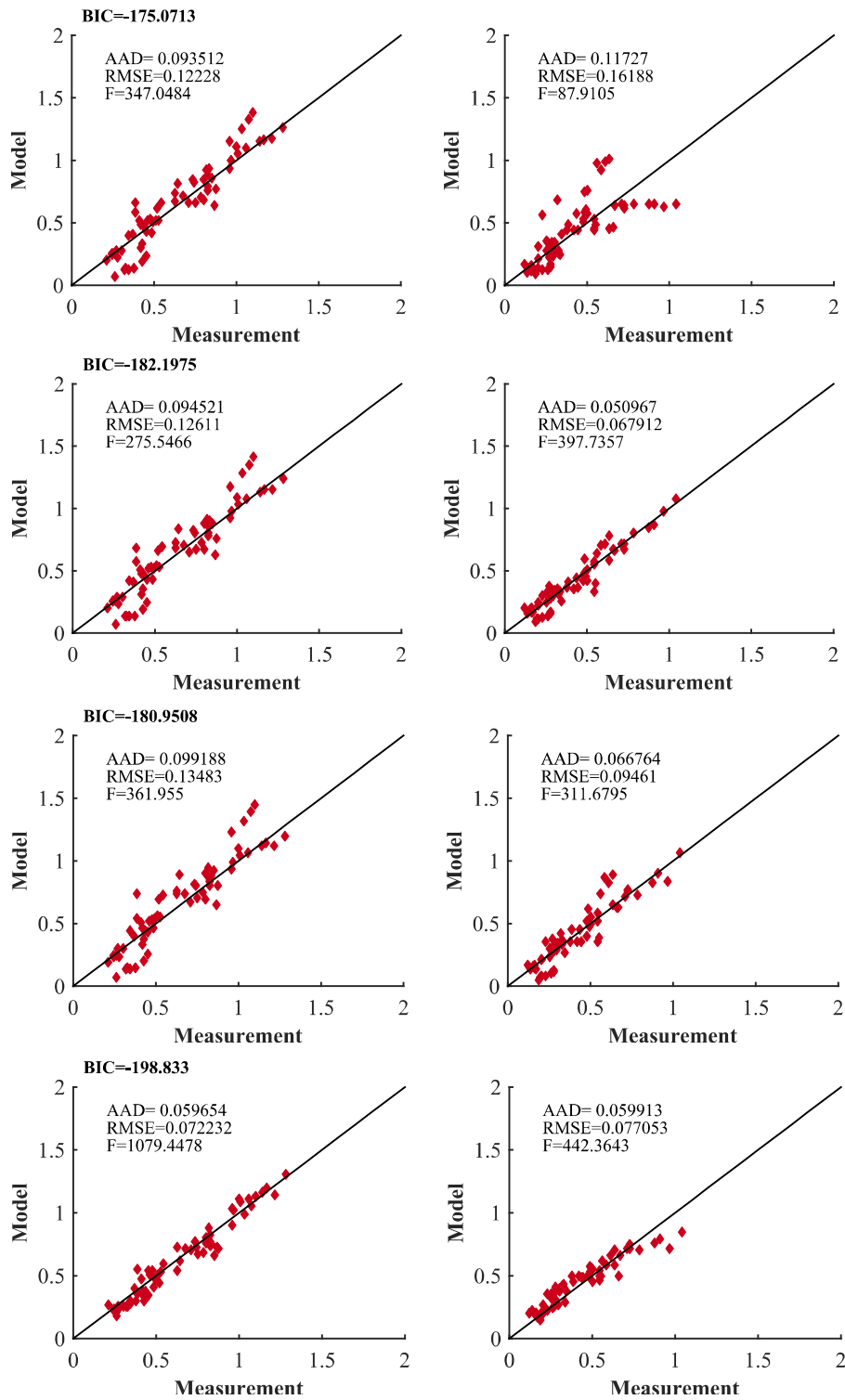


Figure 5.8 Parity plot of different models. From top to bottom: Model A, Ronsch Model, Xu Model, and Model B. Left column: rate of r-WGS. Right column: rate of CO Methanation

Table 5.6 First principal component analysis at the estimates of rate and adsorption constants ($\lambda_{th}=50$)

No.	λ	$k_{3,r}$	$k_{5,r}$	$k_{6,r}$	$K_{H_2,r}$	$K_{CO_2,r}$	$K_{H_2O,r}$
1	1.74×10^5	0.896	-0.193	0.193	0.241	0.248	-0.064
2	2.17×10^3	-0.145	0.3055	-0.306	-0.145	0.868	-0.133
3	1.11×10^3	0.3275	0.6047	-0.605	-0.1835	-0.3248	0.1491
4	106	0.0986	-0.168	0.1676	-0.5848	0.1516	0.7544
5	2.2×10^{-13}	0	0.7071	0.7071	0	0	0
6	32.72	-0.144	0.109	-0.109	0.7459	0.1202	0.6205

Table 5.7 Second principal component analysis ($\lambda_{th}=50$)

No.	λ	$k_{3,r}$	$k_{6,r}$	$K_{H_2,r}$	$K_{CO_2,r}$	$K_{H_2O,r}$
1	5.12×10^4	-0.921	-0.134	-0.223	-0.284	0.064
2	2×10^3	-0.238	-0.202	-0.123	0.9286	-0.158
3	664.75	0.2617	-0.881	-0.328	-0.1392	0.168
4	32	-0.142	-0.223	0.7451	0.1158	0.6011
5	100.22	0.082	0.3390	-0.5221	0.1560	0.7625

Table 5.8 Third principal component analysis ($\lambda_{th}=50$)

No.	λ	$k_{3,r}$	$k_{6,r}$	$K_{H_2,r}$	$K_{CO_2,r}$
1	5×10^4	0.9228	0.1337	0.2235	0.2840
2	2×10^3	0.2279	0.2127	0.1281	-0.9415
3	647	-0.263	0.8914	0.3215	0.1815
4	58	0.1656	0.3772	-0.9112	0.0013

Similarly, Table 5.9 lists the results of the principal component analysis at the determinant criterion estimates of the activation energies and adsorption enthalpies (E_{a3} , E_{a5} , E_{a6} , ΔH_{H_2} , ΔH_{CO_2} , ΔH_{H_2O}). As shown in Table 5.6, two eigenvalues, λ_5 and λ_6 , are smaller than the threshold eigenvalue. This indicates that some of the aforementioned parameters can't be uniquely estimated or that there are dependencies among certain parameters. The normed eigenvector corresponding to smallest eigenvalue λ_6 has one coefficient, associated with ΔH_{H_2} that is close to 1 while all other coefficients are significantly small. This indicates that there is no correlation between ΔH_{H_2} and the other parameters, and that its effect is insignificant.⁴ Therefore, it is eliminated for the next principal component analysis.

The results of the second principal component analysis (Table 5.7) reveal that the objective function depends on the ratio of E_{a5} and E_{a6} and not on these parameters separately. Therefore, we eliminated E_{a5} for the next principal component analysis (It will be fixed in the parameter estimation problem). All eigenvalues computed in the

third principal component analysis are larger than the threshold value. Thus, all remaining parameters (E_{a3} , E_{a6} , ΔH_{CO_2} , ΔH_{H_2O}) are identifiable.

Table 5.9 First principal component analysis at the estimates of activation energies and enthalpies ($\lambda_{th}=50$)

No.	λ	E_{a3}	E_{a5}	E_{a6}	ΔH_{H_2}	ΔH_{CO_2}	ΔH_{H_2O}
1	2.32×10^4	0.8068	-0.411	0.2166	-0.031	0.074	0.357
2	7.6×10^3	0.4468	0.767	-0.405	0.001	-0.158	0.151
3	2.21×10^3	-0.374	-0.01	0.0053	0.0094	-0.272	0.887
4	986.5	-0.096	0.157	-0.083	-0.013	0.9464	0.252
5	7.37	0	0.467	0.8845	0	0	0
6	0.1	-0.026	0.011	-0.006	-0.9994	-0.017	-0.006

Table 5.10 Second principal component analysis ($\lambda_{th}=50$)

No.	λ	E_{a3}	E_{a5}	E_{a6}	ΔH_{CO_2}	ΔH_{H_2O}
1	1.9×10^4	0.918	-0.262	0.136	0.069	0.258
2	5.1×10^3	0.274	0.837	-0.434	-0.185	0.039
3	1.47×10^3	-0.2	-0.092	0.0474	-0.62	0.753
4	932.7	0.172	-0.156	0.0809	-0.758	-0.604
5	4.35×10^{-13}	0	-0.46	-0.888	0	0

Table 5.11 Third principal component analysis ($\lambda_{th}=50$)

No.	λ	E_{a3}	E_{a6}	ΔH_{CO_2}	ΔH_{H_2O}
1	1.66×10^4	0.956	0.0857	0.0482	0.2754
2	691.2	0.042	0.7464	-0.6062	-0.2715
3	1.49×10^3	0.073	0.4165	0.7474	-0.5125
4	1.27×10^3	-0.28	0.5120	0.2676	0.7667

In conclusion, out of the 12 parameters that were initially estimated, eight can be uniquely identified.

A new parameter estimation procedure is carried out to re-estimate $k_{3,r}$, $k_{6,r}$, $K_{H_2,r}$, $K_{CO_2,r}$, E_{a3} , E_{a6} , ΔH_{CO_2} , ΔH_{H_2O} while $k_{5,r}$, $K_{H_2O,r}$, E_{a5} , ΔH_{H_2} are fixed at their nominal values. This slightly improved the fitting. The values of the estimated parameters are shown in Table 5.12. As reflected by their relatively small 95% confidence interval, the eight parameters were estimated with good certainty. The computed values of the activation energies for the rate determining steps are comparable to the values reported in literature.^{15,95}

For the sake of comparison, the parameters were also estimated by minimizing the sum of squared residual. They are also presented in Table 5.12. As can be seen, the least square estimates were, in general, close to the values obtained by minimizing the determinant criterion.

Table 5.12 Parameter estimates of Model B (see Table 5.5) based on the Determinant Criterion and the Least Square method

Parameter	Min of determinant	Min of RSS
$k_{3,r} [mol\ atm^{1.5}/(g\ hr)]$	7.9±0.65	8.447
$k_{5,r} [-]$	1.408	1.25
$k_{6,r} [atm^{0.5}]$	7.76±1.55	7.39
$K_{H_2,r} [atm^{-1}]$	0.423	0.317
$K_{CO_2,r} [atm^{-1}]$	1.86±0.15	1.686
$K_{H_2O,r} [atm^{-1}]$	0.396±0.189	0.365
$Ea_3 [kJ/mol]$	85.825±5.24	87.3503
$Ea_5 [kJ/mol]$	183.08	170.83
$Ea_6 [kJ/mol]$	96.5±15.8	93.73
$\Delta H_2 [kJ/mol]$	-6.26	-5.34
$\Delta CO_2 [kJ/mol]$	-70.35±10.4	-63.88
$\Delta H_2O [kJ/mol]$	-178.2±44.7	-133.83

The ability of Model B to predict the reaction performance was further validated using a new set of data points that was not employed in the parameter estimation. The data, which is represented in the parity diagram (Figure 5.9), was collected by conducting a series of experiments at different operating conditions. As can be seen, the points cluster

around the diagonal line indicating a very good fit especially with respect to the r-WGS rate equation. An AAD of 0.07 and 0.038 were calculated for the CO methanation and r-WGS rate equations respectively. The relatively low error values demonstrates the reliability and good predictive ability of the derived model.

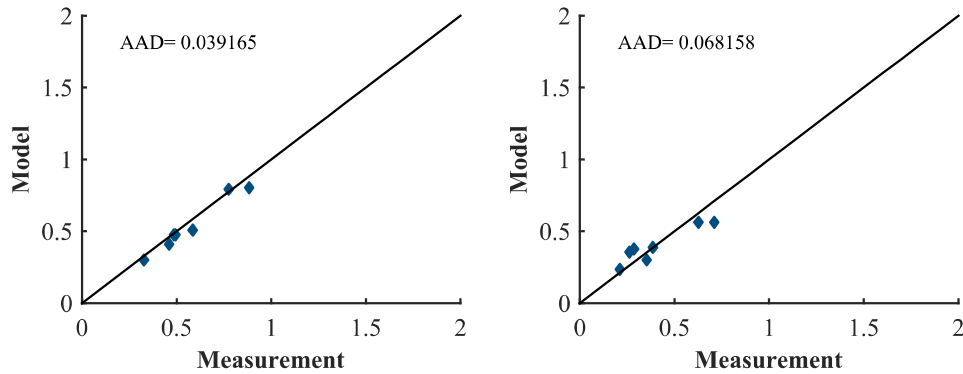


Figure 5.9 Parity plot: Predictive ability of the derived model

5.5 Comparison between reaction rates reported in Literature

To better understand how the kinetic model influences the reactor performance, a packed bed reactor with isothermal cooling is simulated, under the same operating conditions and with the same reactor dimension, using our model (Case 3 and Case 4) and the aforementioned kinetic models reported in literature (Models of Koschany et al. (Case 2), Xu and Froment (Case 1), and Ronsch et al. (Case 5)).

Figure 5.10 depicts the profiles of temperature and CH₄ production rate along the reactor. As expected, the profiles are dependent on the kinetic model employed. The reaction is initiated at the inlet of the reactor in Cases 2, 3, 4, and 5 with the reaction starting a little bit earlier in Case 2. Following the initiation of the reaction, an overshoot in the temperature is observed in the four cases leading to the formation of hot spots. The steepest temperature increase, the highest hotpot temperature, and thus the highest CH₄ production rate are observed in Case 2. This remarkably high activity that is demonstrated by the model of Koschany et al. is attributed to the fact that Koschany et al. employed in their study a much more active catalyst with a nickel loading of 50 % whereas the nickel loading of the catalyst used in this study was 20% (almost double the nickel loading of the catalyst used in this study). The lowest hotspot

temperature is observed in Case 3, when the reactor is simulated using our model which uses parameters estimated based on the determinant criterion. A slightly higher hotspot temperature is observed in Case 4. Nevertheless, the two cases (Case 3 and Case 4) show very similar temperature and CH₄ production rate profiles. In contrast, when the model of Xu and Froment is used in simulating the reactor performance, the initiation of the reaction is delayed and a shift in the location of the hot spot to the inside is observed. This results in a notably different CH₄ production rate profile. The reactor performance based on our kinetic model was mostly comparable to that of Ronsch et al. model, especially after hotspot formation, when the temperature starts to gradually decrease.

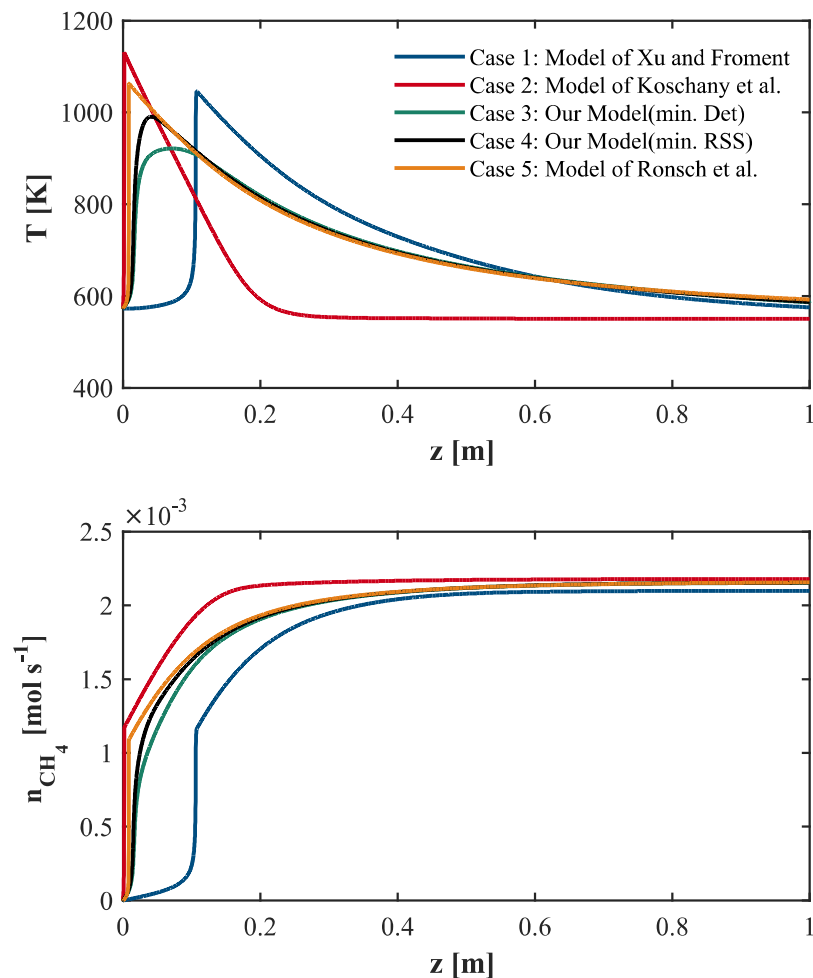


Figure 5.10 Performance of a packed bed reactor simulated using different kinetic models

5.6 Conclusion

A series of experiments were carried out at industrial relevant operating conditions to investigate the kinetics of CO₂ methanation over a commercial nickel-based catalyst. The data collected (see Appendix) were fitted against different models reported in literature and models derived in accordance with reported experimental studies and recently published theoretical calculations (e.g. Density Functional Theory). It was proposed that CO₂ methanation proceeds according to a consecutive pathway comprising of reverse water gas shift and CO methanation reactions. The most adequate rate expressions for r-WGS and CO methanation were developed on the basis of hydrogen assisted mechanisms. The hydrogenation of adsorbed CO₂ into COOH and of adsorbed CO into HCO were found to be the rate determining steps of r-WGS and CO methanation reaction respectively. The developed kinetic model had 12 parameters in total. The quantitative identifiability of the parameters was investigated using eigenvalue decomposition method. Due to the correlation of the parameters, eight of which were identifiable. By combining the kinetic study with other experiments designed for studying the adsorption of important intermediate surface species can help decreasing the number of unidentifiable parameters. Another important tool in this regard is the optimal design of experiments.

The performance of the derived model was then assessed using a “validation” dataset that was different from the dataset used in estimating the model parameters. The model demonstrated an ability to predict the reaction performance with good accuracy. Furthermore, a 1D model was used to simulate a packed bed reactor using our kinetic model and other models reported in literature. Interestingly, the reactor showed a quite different performance using our model compared to the one developed by Xu and Froment and Koshany et al. but a relatively similar performance to that of Ronsch et al. model.

6 Summary and outlook

In the first part of the thesis, CO₂ methanation process for the storage of renewable energy is designed with main emphasis on the reaction section. The process consists of a reaction section and a glycol unit for downstream drying. The optimal design of the reaction section is derived first, in Chapter 3, using a three level design procedure that was developed by Peschel et al. based on the conceptual framework of the Elementary Process Function methodology. The potential of several ‘ideal’ integration concepts for enhancing the reactor productivity was systematically investigated. It was shown that the simultaneous extraction of CH₄ and H₂O coupled with cooling can significantly increase the STY and that the removal of CH₄ is more advantageous than H₂O. Nevertheless, since the extraction of CH₄ from our reaction system can not be technically realized, two reactor configurations that apply water removal were further considered and analyzed: (1) A polytropic membrane reactor which allows in-situ and continuous removal of H₂O over the entire reaction time and (2) a polytropic reactor cascade with intermediate condensation. Design and operation variables such as the temperature profile within the reactors, inlet pressure, inlet composition, reactor dimensions, molar flowrate, number of condensation steps, and the level of condensation were optimized. It was shown that a cascade consisting of 4 multitubular

reactor with co-current heat exchangers and 3 condensation steps was the most attractive reactor configuration for maximizing the STY.

Building on the results obtained in Chapter 3, the economics of the Sabatier process was considered in Chapter 4. The design and operation of the reactors and other process units (e.g. heat exchangers, absorber, reboiler, compressors, pump) were simultaneously optimized for minimum SNG production cost. Reactor cascades consisting of one, two, and three condensation steps were compared. The cascade comprising of three fixed bed multitubular reactors and two condensation steps was found to be the cost optimal reactor configuration. It was shown that the optimal temperature profiles within the reactor is achieved using a combination of adiabatic operation and active cooling. Moreover, the study revealed the importance of considering the interaction between the different process units and the reactors for optimal operation of the process.

In the last part of the thesis, the experimental investigation of the CO₂ methanation and the derivation of comprehensive kinetic model was discussed. The derived model is comprised of reverse water gas shift and CO methanation rate equations. The hydrogenation of adsorbed CO₂ into COOH and of adsorbed CO into HCO were found to be the rate determining steps of r-WGS and CO methanation reaction respectively. Data collected at industrial relevant operating conditions and using a commercial nickel-based catalyst was employed in the discrimination between rival models and the estimation of the parameters. Due to the correlation between the model parameters of the model, only 8 out of 12 parameters could be uniquely identified. The predictive ability of the model was then assessed using a new set of data that was not used in the parameter estimation procedure. The model demonstrated an ability to predict the reaction performance with good accuracy. Afterwards, a packed bed reactor with isothermal cooling was simulated using our kinetic model and other models reported in literature. Interestingly, the reactor demonstrated a quite different performance using our model compared to the one developed by Xu and Froment and Koshany et al. but a relatively similar performance to that of Ronsch et al. model.

With regard to the modeling of the reactor, it may be necessary to implement more complex models (e.g. two dimensional heterogeneous model) for real world operation of the methanation reactor especially in the presence of highly active catalyst. Moreover, given the intermittent nature of the renewable sources, the operation of the reactor under dynamic conditions and how it responds to variations in the feed should be also investigated. Regarding the process design, the optimal design of heat exchanger network should be also considered since it can significantly reduce the investment and operating cost of the process. For the kinetic investigation, the implementation of optimal design of experiments and other advanced experimental techniques like steady state isotopic transient kinetic analysis can be powerful tools for getting insights into the reaction mechanism and increase the accuracy of the parameter estimation.

7 Appendix

Table 7.1 Collected data used in the estimation of the kinetic model parameters: Temperature, partial pressures of the different compounds, and production rates of CH₄ and CO

T [K]	p _{H₂} [atm]	p _{CO₂} [atm]	p _{CH₄} [atm]	p _{H₂O} [atm]	P _{CO} [atm]	r _{CH₄} [mol g ⁻¹ hr ⁻¹]	r _{CO} [mol g ⁻¹ hr ⁻¹]
589	3.363	0.55	0.0070	0.375	0.0062	0.16	0.14
609	7.58	1.87	0.1018	0.232	0.0282	0.66	0.18
588	0.9	0.11	0.0068	0.016	0.0027	0.19	0.08
622	7.4	1.82	0.1510	0.340	0.0383	0.97	0.25
596	5.94	0.72	0.0256	0.061	0.0099	0.33	0.13
617	2.31	0.57	0.0223	0.060	0.0150	0.48	0.32
624	2.81	0.38	0.0248	0.596	0.0102	0.38	0.16
588	0.9	0.22	0.0072	0.019	0.0044	0.20	0.12
615	2.3	0.56	0.0259	0.066	0.0147	0.55	0.31
595	3.94	0.98	0.0198	0.052	0.0121	0.25	0.15
622	8.0	1.28	0.0986	0.225	0.0280	0.91	0.26
573	5.98	0.99	0.0127	0.032	0.0067	0.16	0.09
608	5.35	1.32	0.0591	0.139	0.0213	0.54	0.20
615	2.32	0.57	0.0175	0.047	0.0117	0.38	0.25
615	1.34	0.33	0.0091	0.323	0.0081	0.26	0.23

Model-based optimization and experimental investigation of CO₂ methanation

574	5.99	0.74	0.0109	0.028	0.0057	0.14	0.07
624	1.32	0.32	0.0091	0.245	0.0074	0.34	0.28
638	1.49	0.36	0.0207	0.396	0.0141	0.50	0.34
608	2.77	0.54	0.0124	0.399	0.0101	0.28	0.23
624	3.29	0.53	0.0219	0.422	0.0144	0.50	0.33
614	2.31	0.57	0.0196	0.051	0.0117	0.42	0.25
613	2.3	0.56	0.0204	0.053	0.0126	0.44	0.27
589	1.82	0.33	0.0100	0.025	0.0054	0.28	0.15
615	1.23	0.30	0.0066	0.564	0.0073	0.20	0.22
574	3.97	0.99	0.0135	0.034	0.0070	0.17	0.09
623	4.83	0.94	0.0561	0.135	0.0232	0.71	0.29
624	2.3	0.56	0.0232	0.061	0.0150	0.50	0.32
589	1.82	0.45	0.0100	0.026	0.0062	0.28	0.17
588	1.35	0.22	0.0081	0.020	0.0042	0.23	0.12
624	3.3	0.39	0.0210	0.418	0.0118	0.48	0.27
623	5.84	0.94	0.0569	0.135	0.0215	0.72	0.27
589	7.8	1.94	0.0423	0.102	0.0177	0.27	0.11
588	7.77	1.43	0.0526	0.120	0.0146	0.34	0.09
609	8.1	1.31	0.0691	0.159	0.0204	0.64	0.19
590	0.9	0.22	0.0074	0.019	0.0045	0.21	0.13
594	2.9	0.71	0.0115	0.499	0.0080	0.20	0.14
644	2.73	0.52	0.0269	0.443	0.0208	0.61	0.47
633	1.23	0.30	0.0075	0.570	0.0096	0.23	0.29
588	5.46	1.01	0.0293	0.069	0.0109	0.27	0.10
644	3.30	0.39	0.0259	0.436	0.0167	0.58	0.38
623	6.6	1.28	0.0954	0.220	0.0288	0.88	0.27
574	4.98	0.99	0.0124	0.032	0.0068	0.16	0.09
636	1.36	0.33	0.0116	0.340	0.0119	0.32	0.32

596	5.93	0.97	0.0257	0.063	0.0118	0.33	0.15
608	3.32	0.54	0.0131	0.399	0.0100	0.30	0.23
589	1.8	0.22	0.0094	0.023	0.0041	0.26	0.11
608	6.7	1.32	0.0586	0.138	0.0208	0.54	0.19
589	3.36	0.41	0.0068	0.361	0.0052	0.15	0.12
632	2.44	0.60	0.0328	0.642	0.0209	0.49	0.31
608	3.3	0.26	0.0120	0.392	0.0064	0.28	0.15
590	2.8	0.55	0.0054	0.379	0.0065	0.12	0.15
595	4.93	0.97	0.0238	0.059	0.0119	0.30	0.15
623	2.2	0.53	0.0191	0.419	0.0154	0.44	0.35
622	3.82	0.94	0.0523	0.128	0.0236	0.67	0.30
624	11.38	1.81	0.1623	0.363	0.0381	1.04	0.24
623	5.8	0.69	0.0568	0.132	0.0182	0.72	0.23
644	2.16	0.53	0.0248	0.439	0.0211	0.56	0.48
624	2.74	0.53	0.0212	0.422	0.0151	0.48	0.34
624	1.6	0.40	0.0181	0.047	0.0110	0.55	0.33
588	5.45	1.35	0.0319	0.077	0.0130	0.29	0.12
622	5.24	1.29	0.0856	0.201	0.0298	0.79	0.27
644	3.01	0.58	0.0310	0.492	0.0227	0.63	0.46
624	3.3	0.27	0.0120	0.391	0.0049	0.27	0.11
608	2.21	0.55	0.0114	0.397	0.0103	0.26	0.23
583	2.35	0.58	0.0100	0.025	0.0051	0.22	0.11
608	3.32	0.40	0.0127	0.395	0.0084	0.29	0.19
589	11.75	1.93	0.0549	0.127	0.0170	0.35	0.11
623	3.31	0.26	0.0170	0.405	0.0086	0.39	0.20
609	7.6	1.38	0.0978	0.219	0.0230	0.63	0.15
608	11.5	1.87	0.1103	0.247	0.0266	0.71	0.17

8 Literature Cited

1. Peschel A, Freund H, Sundmacher K. Methodology for the design of optimal chemical reactors based on the concept of elementary process functions. *Industrial & Engineering Chemistry Research*. 2010;49(21):10535–10548.
2. Freund H, Sundmacher K. Towards a methodology for the systematic analysis and design of efficient chemical processes. *Chemical Engineering and Processing: Process Intensification*. 2008;47(12):2051–2060.
3. Vajda S, Valko P, Turányi T. Principal component analysis of kinetic models. *International Journal of Chemical Kinetics*. 1985;17(1):55–81.
4. Vajda S, Rabitz H, Walter E, Lecourtier Y. Qualitative and quantitative identifiability analysis of nonlinear chemical kinetic models. *Chemical Engineering Communications*. 1989;83(1):191–219.
5. Aziz MAA, Jalil AA, Triwahyono S, Ahmad A. CO₂ methanation over heterogeneous catalysts: recent progress and future prospects. *Green Chemistry*. 2015;17(5):2647–2663.
6. Wei W, Jinlong G. Methanation of carbon dioxide: An overview. *Frontiers of Chemical Science and Engineering*. 2011;5(1):2–10.
7. Gao J, Liu Q, Gu F, Liu B, Zhong Z, Su F. Recent advances in methanation catalysts for the production of synthetic natural gas. *RSC Advances*. 2015;5(29):22759–22776.

8. Müller K, Fleige M, Rachow F, Schmeißer D. Sabatier based CO₂-methanation of flue gas emitted by conventional power plants. *Energy Procedia*. 2013;40:240–248.
9. Ghaib K, Nitz K, Ben-Fares F-Z. Chemical methanation of CO₂. A review. *ChemBioEng Reviews*. 2016;3(6):266–275.
10. Abelló S, Berruenco C, Montané D. High-loaded nickel–alumina catalyst for direct CO₂ hydrogenation into synthetic natural gas (SNG). *Fuel*. 2013;113:598–609.
11. Rahmani S, Rezaei M, Meshkani F. Preparation of highly active nickel catalysts supported on mesoporous nanocrystalline γ -Al₂O₃ for CO₂ methanation. *Journal of Industrial and Engineering Chemistry*. 2014;20(4):1346–1352.
12. Aziz MAA, Jalil AA, Triwahyono S, Mukti RR, Taufiq-Yap YH, Sazegar MR. Highly active Ni-promoted mesostructured silica nanoparticles for CO₂ methanation. *Applied Catalysis B: Environmental*. 2014;147:359–368.
13. Tada S, Shimizu T, Kameyama H, Haneda T, Kikuchi R. Ni/CeO₂ catalysts with high CO₂ methanation activity and high CH₄ selectivity at low temperatures. *International Journal of Hydrogen Energy*. 2012;37(7):5527–5531.
14. Frontera P, Macario A, Ferraro M, Antonucci P. Supported catalysts for CO₂ methanation: A review. *Catalysts*. 2017;7(12):59.
15. Dietz L, Piccinin S, Maestri M. Mechanistic insights into CO₂ activation via reverse water–gas shift on metal surfaces. *The Journal of Physical Chemistry C*. 2015;119(9):4959–4966.
16. Bothra P, Periyasamy G, Pati SK. Methane formation from the hydrogenation of carbon dioxide on Ni(110) surface--a density functional theoretical study. *Physical chemistry chemical physics : PCCP*. 2013;15(15):5701–5706.
17. Aldana PU, Ocampo F, Kobl K, Louis B, Thibault-Starzyk F, Daturi M, Bazin P, Thomas S, Roger AC. Catalytic CO₂ valorization into CH₄ on Ni-based ceria-zirconia. Reaction mechanism by operando IR spectroscopy. *Catalysis Today*. 2013;215:201–207.
18. Schild C, Wokaun A, Koeppel RA, Baiker A. Carbon dioxide hydrogenation over nickel/zirconia catalysts from amorphous precursors: On the mechanism of methane formation. *The Journal of Physical Chemistry*. 1991;95(16):6341–6346.

19. Pan Q, Peng J, Wang S, Wang S. In situ FTIR spectroscopic study of the CO₂ methanation mechanism on Ni/Ce_{0.5}Zr_{0.5}O₂. *Catalysis & Science Technology*. 2014;4(2):502–509.
20. Solis-Garcia A, Louvier-Hernandez JF, Almendarez-Camarillo A, Fierro-Gonzalez JC. Participation of surface bicarbonate, formate and methoxy species in the carbon dioxide methanation catalyzed by ZrO₂ -supported Ni. *Applied Catalysis B: Environmental*. 2017;218:611–620.
21. Vesselli E, Rizzi M, Rogatis L de, Ding X, Baraldi A, Comelli G, Savio L, Vattuone L, Rocca M, Fornasiero P, Baldereschi A, Peressi M. Hydrogen-assisted transformation of CO₂ on nickel: The role of formate and carbon monoxide. *The Journal of Physical Chemistry Letters*. 2010;1(1):402–406.
22. Benitez JJ, Carrizosa I, Odriozola JA. HCOOH hydrogenation over lanthanide-oxide-promoted Rh/Al₂O₃ catalysts.
23. Pan Q, Peng J, Sun T, Wang S, Wang S. Insight into the reaction route of CO₂ methanation: Promotion effect of medium basic sites. *Catalysis Communications*. 2014;45:74–78.
24. Fujita S, Terunuma H, Nakamura M, Takezawa N. Mechanisms of methanation of carbon monoxide and carbon dioxide over nickel. *Industrial & Engineering Chemistry Research*. 1991;30(6):1146–1151.
25. Beuls A, Swalus C, Jacquemin M, Heyen G, Karelavic A, Ruiz P. Methanation of CO₂: Further insight into the mechanism over Rh/ γ -Al₂O₃ catalyst. *Applied Catalysis B: Environmental*. 2012;113-114:2–10.
26. Weatherbee GD, Bartholomew CH. Hydrogenation of CO₂ on group VIII metals II. Kinetics and mechanism of CO₂ hydrogenation on nickel. *Journal of Catalysis*. 1982;77(2):460–472.
27. Weatherbee GD, Bartholomew CH. Hydrogenation of CO₂ on group VIII metals I. Specific activity of Ni/SiO₂. *Journal of Catalysis*. 1981;68(1):67–76.
28. Peebles DE, Goodman DW, White JM. Methanation of carbon dioxide on nickel(100) and the effects of surface modifiers. *The Journal of Physical Chemistry*. 1983;87(22):4378–4387.

29. Zağlı E, Falconer JL. Carbon dioxide adsorption and methanation on ruthenium. *Journal of Catalysis*. 1981;69(1):1–8.
30. Lapidus AL, Gaidai NA, Nekrasov NV, Tishkova LA, Agafonov YA, Myshenkova TN. The mechanism of carbon dioxide hydrogenation on copper and nickel catalysts. *Petroleum Chemistry*. 2007;47(2):75–82.
31. Garbarino G, Riani P, Magistri L, Busca G. A study of the methanation of carbon dioxide on Ni/Al₂O₃ catalysts at atmospheric pressure. *International Journal of Hydrogen Energy*. 2014;39(22):11557–11565.
32. Ren J, Guo H, Yang J, Qin Z, Lin J, Li Z. Insights into the mechanisms of CO₂ methanation on Ni(111) surfaces by density functional theory. *Applied Surface Science*. 2015;351:504–516.
33. Appl M. Ammonia, 2. Production Processes. In: *Ullmann's encyclopedia of industrial chemistry* (6th edition). Weinheim: Wiley-Blackwell, 2003:-:68.
34. Kopyscinski J, Schildhauer TJ, Biollaz SMA. Production of synthetic natural gas (SNG) from coal and dry biomass – A technology review from 1950 to 2009. *Fuel*. 2010;89(8):1763–1783.
35. De Saint Jean M, Baurens P, Bouallou C, Couturier K. Economic assessment of a power-to-substitute-natural-gas process including high-temperature steam electrolysis. *International Journal of Hydrogen Energy*. 2015;40(20):6487–6500.
36. De Saint Jean M, Baurens P, Bouallou C. Parametric study of an efficient renewable power-to-substitute-natural-gas process including high-temperature steam electrolysis. *International Journal of Hydrogen Energy*. 2014;39(30):17024–17039.
37. Schaaf T, Grünig J, Schuster MR, Rothenfluh T, Orth A. Methanation of CO₂ - storage of renewable energy in a gas distribution system. *Energy, Sustainability and Society*. 2014;4(1):342.
38. Kiewidt L, Thöming J. Predicting optimal temperature profiles in single-stage fixed-bed reactors for CO₂-methanation. *Chemical Engineering Science*. 2015;132:59–71.
39. Schiebahn S, Grube T, Robinius M, Zhao L, Otto A, Kumar B, Weber M, Stolten D. Power to gas. In: Stolten D, Scherer V, editors. *Transition to renewable energy systems*. Weinheim, Germany: Wiley-VCH, Ü2013:813–848.

40. Jürgensen L, Ehimen EA, Born J, Holm-Nielsen JB. Dynamic biogas upgrading based on the Sabatier process: Thermodynamic and dynamic process simulation. *Bioresource Technology*. 2015;178:323–329.
41. Schlereth D, Hinrichsen O. A fixed-bed reactor modeling study on the methanation of CO₂. *Chemical Engineering Research and Design*. 2014;92(4):702–712.
42. Götz M, McDaniel Koch A, Graf F. State of the art and perspectives of CO₂ methanation process concepts for power-to-gas Applications. *International Gas Research Conference Proceedings*. 2014;1.
43. Lefebvre J, Götz M, Bajohr S, Reimert R, Kolb T. Improvement of three-phase methanation reactor performance for steady-state and transient operation. *Fuel Processing Technology*. 2015;132:83–90.
44. Götz M, Lefebvre J, Schollenberger D, Bajohr S, R. Reimert, Kolb T. Novel methanation concepts for the production of substitute natural gas. *International Gas Research Conference Proceedings*. 2014;3.
45. Brooks KP, Hu J, Zhu H, Kee RJ. Methanation of carbon dioxide by hydrogen reduction using the Sabatier process in microchannel reactors. *Chemical Engineering Science*. 2007;62(4):1161–1170.
46. Holladay JD, Brooks KP, Wegeng R, Hu J, Sanders J, Baird S. Microreactor development for Martian in situ propellant production. *Catalysis Today*. 2007;120(1):35–44.
47. Ohya H, Fun J, Kawamura H, Itoh K, Ohashi H, Aihara M, Tanisho S, Negishi Y. Methanation of carbon dioxide by using membrane reactor integrated with water vapor permselective membrane and its analysis. *Journal of Membrane Science*. 1997;131(1):237–247.
48. Skiff T, Szuts A, Szujo V, Toth A, editors. *Drizo unit competes with solid bed desiccant hydration*. PROCEEDINGS OF THE LAURANCE REID GAS CONDITIONING CONFERENCE., 2002.

49. Blachman M, McHugh T, editors. *Sour gas dehydration technology and alternatives*. PROCEEDINGS OF THE LAURANCE REID GAS CONDITIONING CONFERENCE., 2000.
50. Xu J, Froment GF. Methane steam reforming, methanation and water-gas shift: I. Intrinsic kinetics. *AIChE Journal*. 1989;35(1):88–96.
51. Yaws CL. *Chemical properties handbook: Physical, thermodynamic, environmental, transport, and health related properties for organic and inorganic chemicals*. McGraw-Hill handbooks. New York: McGraw-Hill, 1999.
52. Deublein D, Steinhauser A. *Biogas from Waste and Renewable Resources*. Weinheim, Germany: Wiley-VCH Verlag GmbH & Co. KGaA, 2008.
53. Raman PK, Lau FS, Robinson ET. *Process and apparatus for the separation of methane from a gas stream*. 8999020. 2015.
54. de Wasch AP, Froment GF. Heat transfer in packed beds. *Chemical Engineering Science*. 1972;27(3):567–576.
55. Tsotsas E. Wärmeleitfähigkeit von Schüttschichten. In: *VDI-Wärmeatlas* (10th edition). VDI Buch. Berlin, Heidelberg, New York: Springer, 2006:422–430.
56. Tsotsas E. Wärmeleitung und Dispersion in durchströmten Schüttungen. In: *VDI-Wärmeatlas* (10th edition). VDI Buch. Berlin, Heidelberg, New York: Springer, 2006:1213–1227.
57. Jeschar R. Druckverlust in Mehrkornschüttungen aus Kugeln. *Archiv für das Eisenhüttenwesen*. 1964;35(2):91–108.
58. Doğu T. A general criterion to test the relative importance of intraparticle and external heat and mass transfer resistances in porous catalysts. *The Canadian Journal of Chemical Engineering*. 1985;63(1):37–42.
59. Wakao N, Kagueli S, Funazkri T. Effect of fluid dispersion coefficients on particle-to-fluid heat transfer coefficients in packed beds: Correlation of nusselt numbers. *Chemical Engineering Science*. 1979;34(3):325–336.
60. Fairbanks DF, Wilke CR. Diffusion coefficients in multicomponent gas mixtures. *Industrial & Engineering Chemistry*. 1950;42(3):471–475.

61. Fuller EN, Schettler PD, Giddings JC. New method for prediction of binary gas-phase diffusion coefficients. *Industrial & Engineering Chemistry*. 1966;58(5):18–27.
62. Biegler LT, Grossmann IE, Westerberg AW. *Systematic methods of chemical process design*. Prentice-Hall international series in the physical and chemical engineering sciences. Upper Saddle River, NJ: Prentice-Hall, 1997.
63. Fernández-Prini R, Alvarez JL, Harvey AH. Henry's constants and vapor–liquid distribution constants for gaseous solutes in H₂O and D₂O at high temperatures. *Journal of Physical and Chemical Reference Data*. 2003;32(2):903–916.
64. Khajavi S, Kapteijn F, Jansen JC. Synthesis of thin defect-free hydroxy sodalite membranes: New candidate for activated water permeation. *Journal of Membrane Science*. 2007;299(1):63–72.
65. Khajavi S, Sartipi S, Gascon J, Jansen JC, Kapteijn F. Thermostability of hydroxy sodalite in view of membrane applications. *Microporous and Mesoporous Materials*. 2010;132(3):510–517.
66. Khajavi S, Jansen JC, Kapteijn F. Application of hydroxy sodalite films as novel water selective membranes. *Journal of Membrane Science*. 2009;326(1):153–160.
67. Rohde MP, Schaub G, Khajavi S, Jansen JC, Kapteijn F. Fischer–Tropsch synthesis with in situ H₂O removal – Directions of membrane development. *Microporous and Mesoporous Materials*. 2008;115(1):123–136.
68. Du Toit CG. Radial variation in porosity in annular packed beds. *Nuclear Engineering and Design*. 2008;238(11):3073–3079.
69. Coker AK, Ludwig EE. *Ludwig's applied process design for chemical and petrochemical plants: Volume 1* (4th edition). Amsterdam, Boston: Elsevier Gulf Professional, 2007.
70. Bahadori A, Vuthaluru HB. Simple methodology for sizing of absorbers for TEG (triethylene glycol) gas dehydration systems. *Energy*. 2009;34(11):1910–1916.

71. Bahadori A, Zahedi G, Zendejboudi S, Jamili A. A new method estimates TEG purity versus reconcentrator temperature at different levels of pressure in gas dehydration systems. *International Journal of Oil, Gas and Coal Technology*. 2014;7(1):85.
72. Yaws CL. *Thermophysical properties of chemicals and hydrocarbons* (2nd edition). Amsterdam: GPP Gulf Professional Publ./Elsevier, 2014.
73. Sivals R, editor. *Glycol dehydrator design manual.*, 1976.
74. Stewart M, Arnold K. *Gas dehydration field manual* (1st edition). s.l.: Elsevier professional, 2011.
75. Manning FS, Thompson RE. *Natural gas*. PennWell books. / Francis S. Manning; Richard E. Thompson ; 1. Tulsa, Okla.: PennWell Books, 1991.
76. Chiang JH, Hopper JR. Kinetics of the hydrogenation of carbon dioxide over supported nickel. *Industrial & Engineering Chemistry Product Research and Development*. 1983;22(2):225–228.
77. Cognion JM, Marguerin J. Kinetics of the methanation of carbon oxides. *Kinetics and Catalysis*. 1975;16(6):1346–1352.
78. Dew JN, White RR, Sliepcevich CM. Hydrogenation of carbon dioxide on nickel-kieselguhr catalyst. *Industrial & Engineering Chemistry*. 1955;47(1):140–146.
79. Herwijnen TV, Doesburg HV, Dejong WA. Kinetics of Methanation of CO and CO₂ on a nickel-catalyst. *Journal of Catalysis*. 1973;28(3):391–402.
80. Hubble RA, Lim JY, Dennis JS. Kinetic studies of CO₂ methanation over a Ni/γ-Al₂O₃ catalyst. *Faraday discussions*. 2016;192:529–544.
81. Inoue H, Funakoshi M. Kinetics of methanation of carbon monoxide and carbon dioxide. *Journal of Chemical Engineering of Japan*. 1984;17(6):602–610.
82. Pour V. Hydrogenation of carbon dioxide on nickel catalysts. I. Kinetics of hydrogenation on nickel-chromia catalysts. *Collection of Czechoslovak Chemical Communications*. 1969;34(1):45–56.
83. Shashidhara GM, Ravindram M. A kinetic study of the methanation of CO₂ over Ni–Al₂O₃ catalyst. *Reaction Kinetics & Catalysis Letters*. 1988;37(2):451–456.

84. Yadav R, Rinker RG. Steady-state methanation kinetics over a Ni/Al₂O₃ catalyst. *The Canadian Journal of Chemical Engineering*. 1993;71(2):202–208.
85. Yang Lim J, McGregor J, Sederman AJ, Dennis JS. Kinetic studies of CO₂ methanation over a Ni/γ-Al₂O₃ catalyst using a batch reactor. *Chemical Engineering Science*. 2016;141:28–45.
86. Binder GG, White RR. Synthesis of methane from carbon dioxide and hydrogen. *Chemical Engineering Progress*. 1950;46(11):563–574.
87. Kuśmierz M. Kinetic study on carbon dioxide hydrogenation over Ru/γ-Al₂O₃ catalysts. *Catalysis Today*. 2008;137(2-4):429–432.
88. Lunde P. Rates of methane formation from carbon dioxide and hydrogen over a ruthenium catalyst*1. *Journal of Catalysis*. 1973;30(3):423–429.
89. Shashidhara GM, Ravindram M. Methanation of CO₂ over Ru–SiO₂ catalyst. *Reaction Kinetics & Catalysis Letters*. 1992;46(2):365–372.
90. Traa Y, Weitkamp J. Kinetics of the methanation of carbon dioxide over ruthenium on titania. *Chemical Engineering & Technology*. 1999;22(4):291–293.
91. Wang X, Hong Y, Shi H, Szanyi J. Kinetic modeling and transient DRIFTS–MS studies of CO₂ methanation over Ru/Al₂O₃ catalysts. *Journal of Catalysis*. 2016;343:185–195.
92. Koschany F, Schlereth D, Hinrichsen O. On the kinetics of the methanation of carbon dioxide on coprecipitated NiAl(O)_x. *Applied Catalysis B: Environmental*. 2016;181:504–516.
93. Rönsch S, Köchermann J, Schneider J, Matthischke S. Global reaction kinetics of CO and CO₂ methanation for dynamic process modeling. *Chemical Engineering & Technology*. 2016;39(2):208–218.
94. Zhang J, Fatah N, Capela S, Kara Y, Guerrini O, Khodakov AY. Kinetic investigation of carbon monoxide hydrogenation under realistic conditions of methanation of biomass derived syngas. *Fuel*. 2013;111:845–854.
95. Zhou M, Liu B. DFT investigation on the competition of the water-gas shift reaction versus methanation on clean and potassium-modified nickel(1 1 1) surfaces. *ChemCatChem*. 2015;7(23):3928–3935.

96. Vesselli E, Schweicher J, Bundhoo A, Frennet A, Kruse N. Catalytic CO₂ hydrogenation on nickel: novel insight by chemical transient kinetics. *J. Phys. Chem. C*. 2011;115(4):1255–1260.
97. Choe S-J, Kang H-J, Kim S-J, Park S-B, Park D-H, Huh D-S. Adsorbed carbon formation and carbon hydrogenation for CO₂ methanation on the Ni(111) Surface: ASED-MO Study. *Bulletin of the Korean Chemical Society*. 2005;26(11):1682–1688.
98. Box GEP, Draper NR. The Bayesian estimation of common parameters from several responses. *Biometrika*. 1965;52(3-4):355–365.
99. Kang G, Bates DM. Approximate inferences in multiresponse regression analysis. *Biometrika*. 1990;77(2):321–331.
100. Klose J, Baerns M. Kinetics of the methanation of carbon monoxide on an alumina-supported nickel catalyst. *Journal of Catalysis*. 1984;85(1):105–116.

Publications and Statements of Authorship

Articles

A. El Sibai, L. Rihko-Struckmann, K. Sundmacher, Synthetic Methane from CO₂: Dynamic optimization of the Sabatier process for power to gas applications. *Computer Aided Chemical Engineering*, 37 (2015), 1157-1162

A. El Sibai formulated the methodology, carried out the optimization, and wrote the manuscript

A. El Sibai, L. Rihko-Struckmann, K. Sundmacher, Model based optimal Sabatier reactor design for Power-to-Gas applications. *Energy Technology*, 5 (2017), 911-921.

A. El Sibai formulated the methodology, carried out the optimization, and wrote the manuscript

Name: Ali El Sibai
Date of Birth: February 26th, 1987
Place of Birth: Beirut, Lebanon
Nationality: Lebanese
Marital Status: Single
Post-Address: Seyyad Street, Al Marwa bldg.,5th floor
Tahwitat El Ghadeer
Beirut, Lebanon
Phone number: +49/15257659499 / +961/81687353
Email: alielsibai@gmail.com

05/2011- **Candidate Dr. Eng.**
03/2018 PhD in Process Systems Engineering, **Otto-von-Guericke University (OvGU)**,
Magdeburg, Germany

04/2009- **M.Sc. Chemical and Process Engineering**
03/2011 Master studies in Chemical and Process Engineering, Faculty of Process
Engineering, OvGU, Magdeburg, Germany. **Grade: 1.1** (Marks: 1-Excellent, 5-
Failed)
Master thesis: *Measurement of S-NDR type oscillations in the*
N₂,H₂O,CO|N₂,H₂O system, Grade: 1.0

10/2005- **B.S Chemistry**
09/2008 Bachelor studies in Chemistry, Faculty of Sciences, Lebanese University, Beirut,
Lebanon.

08/2005 **High School Diploma**

